Factors influencing the catalytic activity of Fe-ZSM-5 during the catalytic conversion of N_2O

by

Franschua Johan van der Walt

BSc Chemistry and Applied Mathematics (Unisa)

Higher National Diploma Chemical Engineering (Vaal University of Technology)

National Diploma Chemical Engineering (Vaal University of Technology)

Master in Business Administration (University of Bedfordshire)

A thesis submitted to the University of Cape Town in fulfilment of the requirements for the degree of

Master of Science in Engineering

Centre for Catalysis Research

Department of Chemical Engineering

University of Cape Town

March 2015

Synopsis

Zeolites have found widespread applications as acid catalysts for decades. By introducing transition metal ions in the cation position, the zeolite is transformed into a redox catalyst. The nature of the trivalent heteroatom influences the properties of the zeolite. Contrary to Al-zeolites, Fe-containing zeolites show redox properties, since Fe can easily change its oxidation state (Fe^{2+}, Fe^{3+}, or Fe^{4+}). Catalytic function of isolated redox sites within zeolite cavities (or channels) may result in a material with specific redox properties (Kiwi-Minsker *et al.*, 2003). The properties of transition metal exchanged zeolites have been studied from the 1960's onwards and the conversion of N_2O over Fe-Y zeolites has been studied by Fu *et al.* (1981) in late 1970's.

In this study, the preparation of iron ZSM-5 zeolite catalysts by mechanochemical means and thermally induced solid-state ion exchange was studied. After grinding the NH_4-Zeolite and ferrous chloride, no x-ray reflections characteristic of ferrous chloride are detected. After heating the sample to 120 and 200 ºC reflections characteristic of ferrous chloride are visible but disappear upon further heating to 300 ºC. No porosity is observed after grinding and heating up to 200 °C as a result of pore mouth blocking. Moreover, upon heating up to 500 ºC porosity starts to develop with pore volumes and pore sizes slightly lower than those of the parent zeolite. From the thermogravimetric analysis it is evident that the ion exchange takes place during calcination from 150 and 420 ºC in agreement with the literature.

In the second part of the study commercial Fe-ZSM-5 catalyst samples with different N_2O conversion activities (in the presence of H_2O and NO at 425 °C), ranging between 70 and 90 % (high, mid and low activity) are studied and characterised. The effect of temperature during calcination of the plant produced and laboratory calcined extrudate catalyst material was investigated. Panov *et al.* (1996) reported in the literature that the Fe^{2+} is oxidised to Fe^{3+} in the presence of N_2O forming what they called the α-oxygen, a form of active surface oxygen, with the evolution of molecular nitrogen. During the conversion, two surface α-oxygen atoms migrate, combine and desorbs as molecular oxygen from the surface. The α-oxygen forms between 200 and 350 ºC and desorbs as molecular oxygen above 350 ºC (Taboada *et al.,* 2005). In this study, no correlation to N_2O conversion activity could be found

for the α-oxygen content and correspondingly the concentrations of the respective iron oxides and iron hydroxides in the Fe-ZSM-5 samples.

The high N_2O conversion test result, 91 % (in the presence of H_2O and NO at 425 °C), of the one specific plant produced and laboratory calcined extrudate sample, Fe-ZSM-5/500 compared to other commercial produced Fe-ZSM-5 samples ranging from 70 to 90 % (in the presence of H_2O and NO at 425 °C), the remarkable similarity of the characteristics with the Low Fe-ZSM-5 (activity of 71 %) sample, the high peak counts from the (1 0 4) and (1 1 0) planes at 33.1 ° and 35.6 ° 2Θ on the powder XRD, the high percentage of octahedral ferric species in small oligonuclear clusters characterized by strong absorptions between 300 and 400 nm, the low α-oxygen sites, the high percentage magnetic hyperfine field sextet on the Mössbauer spectra and the N_2O conversion Arrhenius plot indicate that there are possibly different active sites and different mechanisms involved in the catalytic reaction for this sample (Fe-ZSM-5/500) compares with the other ZSM-5 samples. The predominant active iron species in the Fe-ZSM-5/500 and Low Fe-ZSM-5 (N_2O conversion activity of 91 and 71 % respectively) samples are probably binuclear oxygen bridged iron sites ($Z^-[(OH)FeOFe(OH)]^{2+}$) and for the commercial produced High Fe-ZSM-5 and Mid Fe-ZSM-5 (N_2O conversion activity of 90 and 86 % respectively) samples mononuclear iron sites ($[Z^-[FeO]^+$) in extra framework positions. The Low Fe-ZSM-5 (activity of 71 %) sample contains a significant amount of Fe_2O_3 clusters on the external surface that reduces pore diffusion of the reaction gases to and from the active sites.

It was observed that the N_2O conversion activity (in the presence of H_2O and NO at 425 °C) of the plant produced and laboratory calcined extrudate catalyst samples decreases monotonically with an increase in the calcination temperature. The XRD and UV/visible spectra are identical for the samples calcined at the different temperatures. Nonetheless, the increase in calcination temperature from 500 to 650 °C strongly influences local electronic structure of Fe species, as observed by Mössbauer spectrometry at room temperature. The magnetic hyperfine field sextet identified in the 500 ºC sample is converted into two sextets after further heating to 650 ºC, each with approximately equal chemical shift off-sets either side of the original sextet. This is indicative of partial dehydration of the iron complex without a change in oxidation state and resulting from a loss of hydroxyl groups, which are converted into oxides.

Declaration

I know the meaning of plagiarism and declare that all of the work in the document, save for that which is properly acknowledged, is my own.

Acknowledgements

This thesis is a result of my work as a process engineer on the manufacturing facility of Clariant (previously Süd-Chemie) where the iron zeolites are manufactured.

First of all, I would like to thank my supervisor Professor Jack Fletcher for the support and guidance in execution of the research. To the management of Clariant, I am thankful for giving me the opportunity and financial support to work on this exciting project. A special thanks to Dr A Tissler for the numerous discussions on my work. I would like to thank Dr Thomas Moyo for the Mössbauer spectroscopy and the deconvolution of the spectra.

Finally, special appreciation to my wife from whom I always get support and lovely care.

Glossary

α-Oxygen	- reactive surface oxygen
α-sites	- the site where the α-oxygen forms
BET	- Brunauer-Emmet-Teller model for multilayer adsorption
Binuclear	- two bonded atoms/ions
BJH method	- Barrett, Joyner and Halenda method
Brønsted site	- Strong acid/base sites
Brønsted acid protons	- Strong acid
cation position	- the ion exchange position on the zeolite matrix
Crystalline	- highly ordered microscopic structure
CVD	- Chemical Vapour Deposition
DRIFTS	- Diffuse Reflectance Infrared Fourier Transform Spectroscopy
ESR	- Electron Spin Resonance
EXAFS	- X-ray absorption fine structure
Extra-framework position	- outside the zeolite framework
Framework position	- part of the zeolite matrix
FTIR	- Fourier Transform InfraRed
Isomer shift (IS)	- Mössbauer parameter indicative of the electron density
GHSV	- gas hourly space velocity
Isolated ions	- ion bonded to cation position of the zeolite
Magnetic hyperfine field	- Mössbauer parameter indicative unpaired spin
Micropore	- pores with pore sizes smaller than 20 Å
Mesopore	- pore sizes between 20 and 500 Å
Mononuclear	- single bonded atom/ion
Lewis acid sites	- weak acid site
Oligonuclear	- multiple bonded atoms/ions
Physisorbed	- physical adsorption
Quadrupole splitting (QS)	- Indication of the symmetry of the Mössbauer atom
Redox catalyst	- Catalyst with reduction and oxidation properties
SCD	- Selective catalytic decomposition
SSIE	- solid-state ion exchange
STP	- Standard Temperature and Pressure (100 kPa and 0 °C)
TAP	- Temporal Analysis of Products

TCD	- Thermal Conductivity Detector
TGA	- Thermogravimetric Analysis
TPD	- Temperature Programed Desorption
TPR	- Temperature Programed Reduction
Ultra-micropore	- Pore sizes below 7 Å
UV/visible	- Ultra violet and visible light
WIE	- Wet Ion Exchange
XRD	- X-ray Diffraction
ZSM-5	- Zeolite structure

Table of Contents

Synopsis ii

Declaration iv

Acknowledgements v

Glossary vi

Table of Contents viii

List of Figures xi

List of Tables xvi

1. Introduction 1

2. Background and literature review 3

2.1. Preparation methods 3

2.1.1. Isomorphous substitution 3

2.1.2. Wet ion exchange (WIE) 3

2.1.3. Chemical vapour deposition (CVD) 4

2.1.4. Solid-state ion exchange (SSIE) 4

2.2. Catalytic activity and the nature of the iron species 8

2.3. Catalytically active sites and the nature of the α-oxygen 14

2.4. The effect of temperature on the active sites. 16

2.5. Reaction mechanism 18

2.6. Reaction kinetics 22

3. Objectives of the study 26

4. Experimental 27

4.1. Preparation of the samples 27

4.1.1. Powder catalytic materials 27

4.1.2. Shaped catalyst (extrudates) 28

4.2. Physicochemical characterisation methods 30
4.2.1. Powder X-ray diffraction 30
4.2.2. Surface area and porosity 30
4.2.3. Differential thermogravimetric analysis (DTGA) 31
4.2.4. Ammonia temperature programmed desorption (TPD) 31
4.2.5. Temperature programmed N_2O conversion 31
4.2.6. Temperature programmed reduction (TPR) 33
4.2.7. Diffuse reflectance UV/visible spectroscopy 33
4.2.8. Mössbauer spectroscopy 34
4.2.9. Catalytic activity for N_2O conversion 34
5. Results 36
5.1. Structural/crystallographic characterisation 36
5.2. Porosity and surface area 41
5.3. Differential thermogravimetric analysis (DTGA) 46
5.4. Ammonia temperature programmed desorption (TPD) 47
5.5. Temperature programmed N_2O conversion and α-oxygen concentration 48
5.6. Temperature programmed reduction (TPR) 54
5.7. Diffuse reflectance UV/visible spectroscopy 54
5.8. Mössbauer spectroscopy 57
5.9. Catalyst activity 58
6. Discussion 60
6.1. Characterisation of the solid-state ion exchange 60
6.2. The nature of the iron species and effect on catalytic activity 62
6.3. The relationship between the α-oxygen content and the catalytic activity. 71
6.4. The effect of temperature during the final calcination of the extruded catalyst. 72
7. Conclusion 75

References 77

A. Appendix A: Analytical Methods – Extended Description 90

A-1. Physical adsorption 90

A-1.1 BET 90

A-1.2 Micro porosity analysis 91

A-1.3 t-plot method 91

A-1.4 MP method 92

A-1.5 Dubinin-Radushkevich models 93

A-1.6 Mesoporosity 94

A-2. Temperature programmed methods 95

A-2.1 Temperature programmed desorption (TPD) 95

A-2.2 Temperature programmed reduction (TPR) and temperature programmed oxidation (TPO) 95

A-2.3 Thermo gravimetric analysis (TGA) 96

A-3. Mössbauer spectroscopy 96

A-3.1 Isomer Shift (IS) 97

A-3.2 Quadrupole Splitting (QS_{Doub}) 98

A-3.3 Magnetic hyperfine splitting (H) 98

List of Figures

Figure 2.1 X-ray diffractograms of Fe-ZSM-5 (a) before milling and (b) after 12 min milling. Kharitonov *et al*. (2003) 8

Figure 2.2 Schematic representation of the different Fe species identified in Fe-ZSM-5 (Pérez-Ramírez *et al.*, 2002b). 9

Figure 2.3 Cationic positions within the ZSM-5 (Wichterlova *et al.*, 2003) 10

Figure 2.4 Temporal analysis of products (TAP) for N_2O conversion over mononuclear iron sites. Kondratenko and Pérez-Ramírez (2007) 15

Figure 2.5 Temperature dependency for response time (t_{max}) for maximum O_2 and N_2 release during N_2O conversion. Kondratenko and Pérez-Ramírez (2007) 15

Figure 2.6 The effect of calcination temperature on the temperature at 80 % N_2O conversion Zhang et al., 2014; Roy et al., 2008. 18

Figure 2.7 Reaction mechanism for the conversion of N_2O over mononuclear iron site (Heyden *et al.*, 2005) 20

Figure 2.8 Reaction mechanism for the conversion of N_2O over binuclear iron site (Hansen *et al.*, 2007) 22

Figure 2.9 N_2O conversion curves over mononuclear and binuclear oxygen bridged iron sites (Hansen *et al.,* 2007). 23

Figure 2.10 Arrhenius plots for N_2O conversion curves over mononuclear (Heyden *et al.*, 2005). 24

Figure 2.11 Arrhenius plots for N_2O conversion curves over binuclear oxygen (1 ppb H_2O) bridged iron sites (Hansen *et al.,* 2007). 24

Figure 2.12 Arrhenius plot for the binuclear iron site for reactions 18, 20, 21, 23 and the overall rate limiting curve modelled with DFT by Hansen *et al.* (2007). 25

Figure 4.1 TCD calibration curve for temperature programmed N_2O conversion over samples Fe-ZSM-5 (TCD signal for N_2+O_2 and N_2O concentration, N_2O 4.8 vol % in helium, 10 ºC/min). 32

Figure 5.1 Powder XRD patterns for M0, M120, M200, M300, $FeCl_2.4H_2O$ and NH_4Cl 37

Figure 5.2 Section of powder XRD patterns of M500, and Z500 37

Figure 5.3 Section of powder XRD patterns of M0, M120, M200, M400, and M500 38

Figure 5.4 Powder XRD patterns for $FeCl_2.4H_2O$ at ambient temperature, 120, 200 and 300 °C 38

Figure 5.5 Section of powder XRD patterns for M0, M120, M200, M300, and $FeCl_2.4H_2O$ 39
Figure 5.6 Powder XRD patterns for Fe-ZSM-5/500, Low Fe-ZSM-5, High Fe-ZSM-5 and Z500. α-Fe_2O_3 aggregates larger than 3-5 nm particle size peaks at 33.1° and 35.6° 2θ. 40
Figure 5.7 Powder XRD patterns for samples Fe-ZSM-5/500 and Fe-ZSM-5/900. α-Fe_2O_3 aggregates larger than 3-5 nm particle size peaks at 33.1° and 35.6° 2θ. 41
Figure 5.8 N_2 isotherms at recorded at liquid nitrogen temperature (-196 °C) of samples M0, M300, M400, M500 and Z500 43
Figure 5.9 MP method plots of the supermicropore sizes and pore volumes for samples M120, M300, M400, M500 and Z500 43
Figure 5.10 N_2 isotherms at recorded at liquid nitrogen temperature (-196 °C) of samples Fe-ZSM-5/500 and Fe-ZSM-5/650 45
Figure 5.11 MP method plots of the of the supermicropore sizes and pore volumes for samples Fe-ZSM-5/500 and Fe-ZSM-5/650 45
Figure 5.12 DTGA-MS of sample M0 (5 ºC/min in nitrogen) 46
Figure 5.13 Section of ammonia TPD of Z0 (saturated with ammonia in helium, heated at 10 ºC/min to 700 ºC in 20 cm3/min helium at STP) and NH_4Cl DTGA of M0 (5 ºC/min in nitrogen) 47
Figure 5.14 Ammonia TPD of samples Fe-ZSM-5/500, Fe-ZSM-5/650 and Z0 (saturated with ammonia in helium, heated at 10 ºC/min to 700 ºC in 20 cm^3/min helium at STP) 48
Figure 5.15 Temperature programmed N_2O conversion over samples Fe-ZSM-5/500 and Fe-ZSM-5/650 (TCD signal for N_2+O_2 concentration, N_2O 4.8 vol % in helium, 10 ºC/min, 0.3 g sample) 49
Figure 5.16 Temperature programmed N_2O conversion over samples High Fe-ZSM-5, Mid Fe-ZSM-5, Low Fe-ZSM-5, Fe-ZSM-5/500 and Z0 (TCD signal for N_2 below 350 °C and N_2+O_2 concentration above 350 °C, N_2O 4.8 vol % in helium, 10 ºC/min, 0.3 g sample) 50
Figure 5.17 Arrhenius plots for N_2O conversion over samples High Fe-ZSM-5, Mid Fe-ZSM-5, Low Fe-ZSM-5, Fe-ZSM-5/500 and Z0 (N_2O 4.8 vol % in helium, 10 ºC/min, 0.3 g sample) 51

Figure 5.18 Catalytic activity N_2O conversion performance test results (1 000 ppm N_2O, 100 ppm NO, 2.5 % O_2 and 3 100 ppm H_2O in nitrogen at 10 000 h-1) vs the temperature at 80 % conversion during temperature programmed N_2O conversion (N_2O 4.8 vol % in helium, 10 ºC/min, 0.3 g sample). 51
Figure 5.19 α-oxygen concentrations for Fe-ZSM-5/500 and Fe-ZSM-5/650 (TCD signal for N_2 concentration, N_2O 4.8 vol % in helium, 10 ºC/min, 0.3 g sample) 52
Figure 5.20 Ammonia TPR of samples Fe-ZSM-5/500 and Fe-ZSM-5/650 54
Figure 5.21 Diffuse Reflectance UV/visible spectra for samples Fe-ZSM-5/500 and Fe-ZSM-5/650 55
Figure 5.22 Diffuse Reflectance UV/visible spectra for samples Fe-ZSM-5/500, Low Fe-ZSM-5, Mid Fe-ZSM-5 and High Fe-ZSM-5. See section 4.2.7 for assignments. 56
Figure 5.23 Mössbauer spectra, recorded at room temperature in air of, High Fe-ZSM-5, Mid Fe-ZSM-5, Low Fe-ZSM-5, Fe-ZSM-5/500 and Fe-ZSM-5/650 with curves derived from deconvolution. 57
Figure 5.24 N_2O selective catalytic conversion at 425°C over catalyst Fe-ZSM5/500, Fe-ZSM5/550, Fe-ZSM5/600 and Fe-ZSM5/650, as a function of final catalyst calcination temperature. (1 000 ppm N_2O, 100 ppm NO, 2.5 % O_2 and 3 100 ppm H_2O in nitrogen at 10 000 h^{-1} at 425 °C) 59
Figure 6.1 Ion exchange mechanism 61
Figure 6.2 Conversion of N_2O (1 000 ppm N_2O, 100 ppm NO, 2.5 % O_2 and 3 100 ppm H_2O in nitrogen at 10 000 h^{-1} at 425 °C) over ion exchanged samples High Fe-ZSM-5, MiD Fe-ZSM-5 and Low Fe-ZSM-5 (full symbols) and Fe-ZSM-5/500, Fe-ZSM-5/550, Fe-ZSM-5/600 and Fe-ZSM-5/650 (open symbols) vs the respective XRD intensities of α-Fe_2O_3 at 33.1° and 35.6° (diamonds and squares, respectively). 63
Figure 6.3 Conversion of N_2O (1 000 ppm N_2O, 100 ppm NO, 2.5 % O_2 and 3 100 ppm H_2O in nitrogen at 10 000 h^{-1} at 450 °C) over ion exchanged samples High Fe-ZSM-5, MiD Fe-ZSM-5, Low Fe-ZSM-5 and Fe-ZSM-5/500 vs the percentage Fe^{3+} isolated species (wave lengths between 200 and 300 nm). 64
Figure 6.4 Conversion of N_2O (1 000 ppm N_2O, 100 ppm NO, 2.5 % O_2 and 3 100 ppm H_2O in nitrogen at 10 000 h^{-1} at 425 °C) over ion exchanged samples High Fe-ZSM-5, MiD Fe-ZSM-5, Low Fe-ZSM-5 and Fe-ZSM-5/500 vs the

percentage Oligomeric Fe_xO_y in zeolite channel (wave lengths between 300 and 400 nm). 64

Figure 6.5 Conversion of N_2O (1 000 ppm N_2O, 100 ppm NO, 2.5 % O_2 and 3 100 ppm H_2O in nitrogen at 10 000 h^{-1} at 425 °C) over ion exchanged samples High Fe-ZSM-5, MiD Fe-ZSM-5, Low Fe-ZSM-5 and Fe-ZSM-5/500 vs the percentage Fe_2O_3 cluster on external surface (wave lengths between 400 and 600 nm). 65

Figure 6.6 Conversion of N_2O (1 000 ppm N_2O, 100 ppm NO, 2.5 % O_2 and 3 100 ppm H_2O in nitrogen at 10 000 h^{-1} at 450 °C) over ion exchanged samples High Fe-ZSM-5, MiD Fe-ZSM-5, Low Fe-ZSM-5 and Fe-ZSM-5/500 vs the percentage Mössbauer isomer shift. 65

Figure 6.7 Conversion of N_2O (1 000 ppm N_2O, 100 ppm NO, 2.5 % O_2 and 3 100 ppm H_2O in nitrogen at 10 000 h^{-1} at 450 °C) over ion exchanged samples High Fe-ZSM-5, MiD Fe-ZSM-5, Low Fe-ZSM-5 and Fe-ZSM-5/500 vs the percentage Mössbauer sextet. 66

Figure 6.8 Conversion of N_2O (1 000 ppm N_2O, 100 ppm NO, 2.5 % O_2 and 3 100 ppm H_2O in nitrogen at 10 000 h^{-1} at 425 °C) over ion exchanged samples High Fe-ZSM-5, MiD Fe-ZSM-5, Low Fe-ZSM-5, Fe-ZSM-5/500 and Fe-ZSM-5/650 vs the α-oxygen/total Fe ratio. 67

Figure 6.9 Arrhenius plots of N_2O conversion over High Fe-ZSM-5, Mid Fe-ZSM-5 (N_2O 4.8 vol % in helium, 10 ºC/min, 0.3 g sample) and Mononuclear Fe site determined with DFT (Hansen *et al.*, 2007) 70

Figure 6.10 Arrhenius plots of N_2O conversion over Low Fe-ZSM-5, Fe-ZSM-5/500 (N_2O 4.8 vol % in helium, 10 ºC/min, 0.3 g sample) and 65 % binuclear Fe sites with 35 % Fe_2O_3 clusters as modelled with DFT (Hansen *et al.*, 2007) 70

Figure 6.11 α-oxygen content for samples High Fe-ZSM-5, MiD Fe-ZSM-5 and Low Fe-ZSM-5 and Fe-ZSM-5/500 vs the α-oxygen/total Fe ratio. 72

Figure A.1 Illustration of t-plot method for the determination of pore volume (Webb and Orr, 1997) 91

Figure A.2 Illustration of MP method for the determination of pore volume at different points along the nonlinear t-curve (Webb and Orr, 1997) 92

Figure A.3 Example of a typical N_2-isotherm with corresponding Dubinin-Radushkevich plot. (Lodewyckx and Verhoeven, 2002) 94

Figure A.4 The effects on the nuclear energy levels of ^{57}Fe of (a) the chemical isomer shift and (b) the quadrupole splitting (Berry, 1990) _____ 97
Figure A.5 The effect of magnetic splitting on the nuclear energy levels of ^{57}Fe (Berry, 1990).C _____ 99

List of Tables

Table 4.1 Powder sample identification – laboratory ground and calcined _____ 28
Table 4.2 Shaped samples, laboratory calcined at different temperatures for 5 hours _____ 29
Table 4.3 Shaped catalyst samples studied with different activity _____ 29
Table 5.1 Powder XRD intensities of α-Fe_2O_3 at 33.1 and 35.6 ° _____ 41
Table 5.2 Nitrogen adsorption and desorption data _____ 44
Table 5.3 α-Oxygen concentrations and N_2O conversion temperatures _____ 53
Table 5.4 Relative Diffused Reflectance UV/visible spectrum band intensities _____ 56
Table 5.5 Mössbauer spectra parameters _____ 58
Table A.1 Isomer shift ranges (in mm/s) in iron compounds (Dickson and Berry, 2012). __ 97

1. Introduction

The catalytic properties of transition metal exchanged zeolites have been observed from the 1960's. With the adoption of the Kyoto Protocol in 1997 transition metal exchanged zeolites, with specific reference to iron containing zeolites, have attracted renewed interest for its extraordinary catalytic properties in the abatement on nitrogen oxides into molecular nitrogen and oxygen (Battiston *et al.*, 2003a; Rauscher *et al*., 1999).

The properties of metal exchanged zeolites have been studied from the 1960's, Garten *et al.* (1970) found that Fe-Y zeolite can be oxidised with oxygen and reduced reversibly forming Fe^{2+} and Fe^{3+} compounds, furthermore, it was found in the 1970's that it can decompose N_2O with the first reaction mechanism proposed by Fu *et al*. (1981) in 1980. During 1988 a number of research groups found that benzene can be catalytically converted to phenol with N_2O as oxidising agent over ZSM-5 with selectivity in excess of 95 %. On investigation it was established that the ion present in commercial zeolites was the active component (Panov *et al*. 1993; Overweg *et al*., 2004).

While the catalytic properties of iron-exchanged ZSM-5 are well established, there remains still an open debate in the literature on the nature and the reactivity of the Fe-active phase. The discussion is complicated by the fact that different synthesis techniques are used, different iron loadings and zeolites with different characteristics are used resulting in different Fe-zeolite materials (Battiston *et al.*, 2003a; Marturano *et al.*, 2000).

The material of interest to this study is exclusively used in an environmental application for the selective catalytic decomposition (SCD) of nitrous oxide in the waste gas of nitric acid plants, where ammonia is converted to nitric oxide via catalytic oxidation over a platinum/rhodium catalyst in the Oswald process (Groves *et al.*, 2006). Nitrous oxides are formed in an undesirable side reaction during the oxidation of ammonia and downstream reactions of unreacted ammonia and nitric oxide. The amount varies depending on the operating conditions in the ammonia burner, with high pressure plants generally having a higher emission factor than lower and atmospheric pressure plants, with figures ranging from less than 2 to 19 kg N_2O per ton nitric acid produced (Groves *et al.*, 2006).

The motivation for this study finds itself in the variability in catalytic performance of plant produced catalyst samples during early commercialisation trails and, consequently, a desire to seek a correlation between process conditions and physicochemical characteristics which can be measured on such samples.

2. Background and literature review

2.1. Preparation methods

Various methods of preparing iron zeolites are reported in the literature which can be classified into four groups; isomorphous substitution followed by extraction (Bitter *et al*., 2003; Pérez-Ramírez *et al.*, 2003; Townsend and Coker, 2001 and Qi *et al.*, 2004) , wet ion exchange (Bitter *et al*., 2003; Chen *et al.*, 2011; Marturano *et al.*, 1999; Pieterse *et al.*, 2007 and Qi *et al.*, 2004), solid-state ion exchange (Bitter *et al*., 2003; Rauscher *et al.,* 1999; Lázár *et al.*, 1995; Abu-Zied *et al.*, 2008; Varga *et al.*, 1995; Qi *et al.*, 2004) and sublimation of volatile ferric chloride onto the zeolite matrix, also referred to as chemical vapour deposition (Bitter *et al*., 2003; Townsend and Coker, 2001; Abu-Zied *et al.*, 2008; Li *et al.*, 2007 and Qi *et al.*, 2004).

2.1.1. Isomorphous substitution

For Fe-Zeolites prepared by isomorphous substitution, the zeolite is synthesised hydrothermally with iron ions embodied in the zeolite framework. Thereafter, the iron is partially extracted from the framework to extra-framework position by means of a steaming or a calcination treatment at high temperature. The resulting catalysts show high activity towards the conversion of N_2O. The total iron and active sites concentration are low in these materials with Fe typically below 0.5 wt % (Bitter *et al*., 2003).

2.1.2. Wet ion exchange (WIE)

Wet ion exchange (WIE) catalyst is prepared by exchanging the zeolite acid site with Fe ions with a soluble iron salt in an aqueous solution followed by calcination at 500 °C (Zecchina *et al.*, 2007). The most frequently used salts are $FeCl_2$, $FeSO_4$, $(NH_4)_2Fe(SO_4)_2$, $FeCl_3$ and $Fe(NO_3)_3$ and the H-form zeolite (Zecchina *et al.*, 2007). The method is relatively easy compared to the other preparation methods as it involves fewer steps with a high degree of

reproducibility. The distribution of the iron species into the zeolite by this method is affected by the channel dimensions of the host zeolite, which channels should be wide enough for the hydrated iron ions to freely diffuse to the ion exchange sites located inside the channels (Li *et al.*, 2008). The size of the hydrated ferrous ion $[Fe(OH_2)_6]^{2+}$ is 7 Å at room temperature which make not suitable for ZSM-5 with the channel sizes of 5.1 x 5.5 Å on the (1 0 0) plane and 5.3 x 5.6 Å on the (0 1 0) plane resulting in a very low Brønsted site exchange and high iron oxides clusters on the external surface (Li *et al.*, 2008, Rauscher *et al.,* 1999; Pérez-Ramírez *et al.*, 2003; Zecchina *et al.*, 2007). The activity of catalysts produced with this method are generally lower compared to chemical vapour deposition (CVD) and Solid-state ion exchange (SSIE) due to channel blocking and large iron oxide clusters (Rauscher *et al.,* 1999; Pérez-Ramírez *et al.*, 2003 and Varga *et al.*, 1995).

2.1.3. Chemical vapour deposition (CVD)

For the chemical vapour deposition (CVD) method $FeCl_3$ is reacted with the Brønsted acid sites of H-ZSM-5 in the gas phase where after the catalyst is activated by hydrolysis and calcination (Battiston *et al.*, 2003b). This method is very effective with the complete exchange of the Brønsted protons for the iron ions (Fe/Al=1) in the extra-framework positions and low formation of large iron hydroxide and oxide clusters (Battiston *et al.*, 2003b; Marturano *et al.*, 2001).

2.1.4. Solid-state ion exchange (SSIE)

For solid-state ion exchange (SSIE), a zeolitic precursor (H- or NH_4-form) is ground together with iron salts typically iron sulphates or chlorides. Generally, with solid-state water-free ion exchange "the solid-state ion-exchange method has the following advantages: (i) it allows for control of the metal loading, (ii) it enables the exchange of multivalent cations into the zeolite exchange site (which is normally difficult using aqueous solutions because of the large size of the hydrated metal complex), (iii) it is reproducible even in the presence of air, (iv) it can create some active sites that are different from those obtained by aqueous exchange, and (v) it allows for the control of the metal oxide or crystallite size" (Abu-Zied *et al*., 2008), (vi) a high degree of exchange (up to 100%) can be obtained in a single process step (Karge, 1994).

Park *et al*. (2008) conducted N_2O conversion over a series of Fe-ZSM-5 catalysts prepared by wet ion exchange (WIE) and solid-state ion exchange (SSIE) methods. The SSIE catalysts generally reveal higher N_2O conversion activity than WIE catalysts if Fe/Al > 0.2. A broad XRD reflection for the WIE catalysts containing Fe/Al > 0.2 was observed at 33.8° 2θ indicating the presence of α-Fe_2O_3 on the catalyst surface, while for the SSIE catalysts no oxides patterns have been observed.

High impact mechanical actions on "solid surfaces are known to lead to physical and chemical changes in the near-surface regions where the solid atoms come into contact under mechanical forces. These mechanically initiated chemical and physicochemical effects in solids are generally termed mechanochemical effects" (Venkataraman and Narayanan, 1998) and were first observed in the 1880's by Carey Lea (BalÁž, 2000). Carey Lea investigated the halides of gold, silver, platinum and mercury and observed their conversion to halogens and metals as a result of fine grinding in a mortar. He concluded that the conversion cannot be attributed to temperature because these substances exhibit sufficient thermal stability and it was for the first time pointed out that not only heat, light and electric energy but also mechanical energy is able to initiate chemical reactions (BalÁž, 2000).

Ito *et al*. (1970) found that grinding for several days of stoichiometric mitures of cobalt ammonium phosphate monohydrate (a powder of reddish-violet colour) with potassium carbonate (a white powder), obtaining an intense blue colour which was identified as cobalt potassium phosphate by X-ray diffraction. Similarly, Lefelshtel *et al*. (1978) observed that prolonged grinding of stoichiometric mixtures of $ZnCO_3$ or ZnO and Fe_2O_3 in a ball mill leads to the formation of zinc ferrite ($ZnFe_2O_4$).

It is accepted that all reactions that can take place in solutions are possible in solid-state reactions provided that they come in close contact (Voskresenskii, 1965). "In synthetic inorganic chemistry, however, such solid-state reactions are possible only under three conditions: (1) the reactions should be thermodynamically feasible from the considerations of Gibbs free energy changes, (2) the two reacting species should be in intimate contact and (3) temperatures should be typically above about 40% of the melting points of the inorganic solids" (Venkataraman and Narayanan, 1998).

In the sixties, Thiessen proposed the first model in mechanochemistry- the magma-plasma model (Thiessen *et al*., 1967). According to this model a great quantity of energy is set free at the contact point between colliding particles. This energy is responsible for the formation of a special plasmatic state which is characterized by emission of fairly excited fragments, electrons and photons from the solid substance over a short time scale. The surface of the contacting particles is rather disordered and local temperatures can reach more than 10 000 ºC. Butjagin developed the theory of short-lived active centres (BalÁž, 2000). Upon mechanical impact a new surface arises which is unable to stabilize in the 10^{-9}-10^{-11} second time-frame of thermal excitation. During the 10^{-4}-10^{-7} seconds required for stabilization, chemical bonds are likely to rearrangement due to the relaxation of excess energy.

Solid-state reactions involving zeolites were first observed in the seventies (Karge, 1994). Proton-containing samples of zeolite-Y reacted with sodium chloride under evolution of hydrochloric acid. By means of IR spectroscopy, it was demonstrated that this reaction eliminated acidic OH groups and, thus, removed Brønsted centres from the zeolite structure (Karge, 1994). (Lázár *et al*., 1995) found upon grinding a mixture of iron(II)chloride and NH_4-Y (Fe/Al = 0.5) at ambient temperature that the intensity of the XRD reflections of iron(II)chloride decreased and reflections characteristic of crystalline ammonium chloride appeared indicating that partial contact-induced ion exchange occurred according to the following reaction:

$$FeCl_2 + NH_4\text{-}Y \rightarrow Fe\text{-}Y + NH_4Cl \quad (1)$$

However, Abu-Zied *et al*. (2008) found that, during the thermal treatment of the milled material up to 550 °C, the ion exchange between the NH_4^+ ions of the zeolite and the metal cations of the salt takes place. During the thermal treatment, the solid state interaction occurs which is accompanied by evolution of HCl or NH_4Cl gases.

Long and Yang (2001) studied the temperature programed desorption (TPD) of ammonia with FTIR from ZSM-5 surfaces. Ammonia desorbs over two broad ranges, centered at 160 and 390 °C. They showed that three ammonia species were generated on the ZSM-5 surface; physisorbed NH_3, coordinated NH_3 and NH_4^+ ions, where physisorbed and coordinated NH_3

disappeared below 300 °C coordinated "NH_4^+ ions with three hydrogen atoms bonded to three oxygen ions of the AlO_4 tetrahedra were still detected at 400 °C". When TPD experiments were performed on NH_4-ZSM-5, no NH_3 desorption peak was seen at 160 °C while a peak at 390 °C was observed (Long and Yang, 2001). The NH_3 desorption peak at 390 °C decreased significantly with increasing Fe content as a result of the Brønsted acid protons of ZSM-5 that were substituted by Fe^{2+} or Fe^{3+} (Brandenberger *et al*. (2009); Long and Yang 2001)

The micropore volume decreases as the degree of ion exchange between iron and the cation sites increases. Battison *et al.* (2003) reported that the micropore volume decreases by approximately 20 percent after iron loading by via chemical vapour deposition (CVD) of ferric chloride. Several other authors reported various extents in micropore volume reduction ranging between 5 and 20 percent (Sobolev *et al*., 1993; Panov *et al*., 1993; Marturano *et al.*, 1999; Abu-Zied *et al*., 2008). Also, Bitter *et al.* (2003) found that the micropore volume decreased by approximately 20 percent during mild calcination and only by 14 percent during severe calcination.

Kosanović *et al.* (1995) found that ball milling of zeolite ZSM-5 causes a considerable change in morphological, particulate, and structural properties of the zeolite due to breakages and damages to the original crystal into irregular small amorphous particles. The transformation of crystalline into amorphous phases takes place directly without the formation of intermediate solids different from the starting crystalline and the resulting amorphous phases (Kosanović *et al.*, 1995).

Kharitonov *et al*. (2003) showed that milling of the zeolite either increase its external surface area, or decrease its crystallinity. Abu-Zied *et al*. (2008) performed tests on the duration of milling time compared to activity on various metal exchanged ZSM-5 zeolites. The catalytic activity decreased considerably when the milling time increased from 30 minutes to 4 hours and the crystallinity decreased from initially 98% to 53 %. Kharitonov *et al*. (2003) reported that the micropore volume of Fe-ZSM-5 steadily decreases with the increase of the milling time from an initial 0.115 cm^3/g to 0.010 cm^3/g after 40 minutes milling. Kharitonov *et al*. (2003) found a significant decrease in crystallinity after 12 minutes milling of Fe-ZSM-5 with a centrifugal planetary mill as can be seen in Figure 2.1.

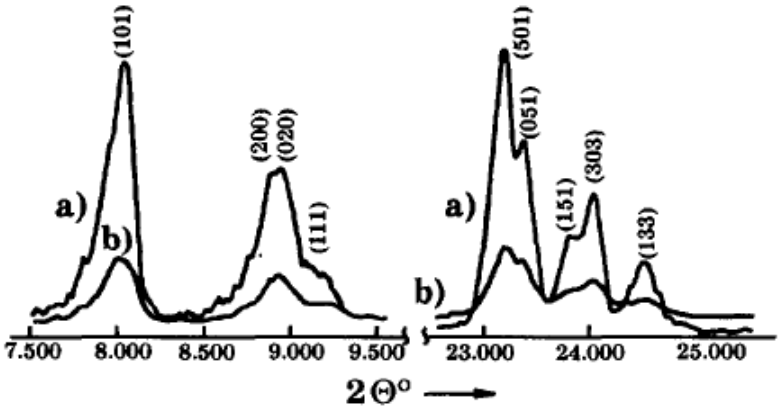

Figure 2.1 X-ray diffractograms of Fe-ZSM-5 (a) before milling and (b) after 12 min milling. Kharitonov *et al.* (2003)

2.2. Catalytic activity and the nature of the iron species

Zeolites have found widespread applications as an acid catalyst for decades (Panov *et al.* 1993). By introducing transition metal ions in the cation position, also referred to as the extra framework position, the zeolite is transformed into a redox catalyst (Kiwi-Minsker *et al.*, 2003). The properties and different valance states of the heteroatom like Fe which can easily change its oxidation state (Fe^{2+}, Fe^{3+}, or Fe^{4+}) (Kiwi-Minsker *et al.*, 2003) in the extra framework position influences the properties of the zeolite which has been suggested to proceed via Fe^{2+} oxidation to Fe^{3+} forming active oxygen species referred to as "α-oxygen" (Panov *et al.*, 1996). N_2O conversion on these active sites produces the oxygen species capable of oxidising a wide range of organic molecules, including methane, selectively producing hydroxyl-containing products (Dubkov *et al.* 2002, Sobolev *et al.*, 1993; Panov *et al.*, 1993 and Yoshizawa *et al.*, 2003). Furthermore, iron zeolites are active in the selective catalytic conversion of N_2O and the selective catalytic reduction of nitric oxide (NO) with hydrocarbons, carbon monoxide and ammonia to form molecular nitrogen (Rauscher *et al.*, 1999; Brandenberger *et al.* 2010a; Battiston *et al.*, 2003a; Chen *et al.*, 2011; Marturano *et al.*, 1999; Pérez-Ramírez *et al.*, 2003).

Different iron species (Figure 2.2) present in Fe-Zeolites have been identified in the literature which include "isolated ions (a) in framework positions (isomorphously substituted) or (b) in cationic positions in the zeolite channels, (c) binuclear and, in general, oligonuclear iron

complexes in extraframework positions, (d) iron oxide Fe_yO_x nanoparticles of size ≤ 2 nm, and (e) large iron oxide particles (Fe_2O_3) up to 25 nm in size located at the surface of the zeolite crystal" (Pérez-Ramírez *et al.*, 2002b).

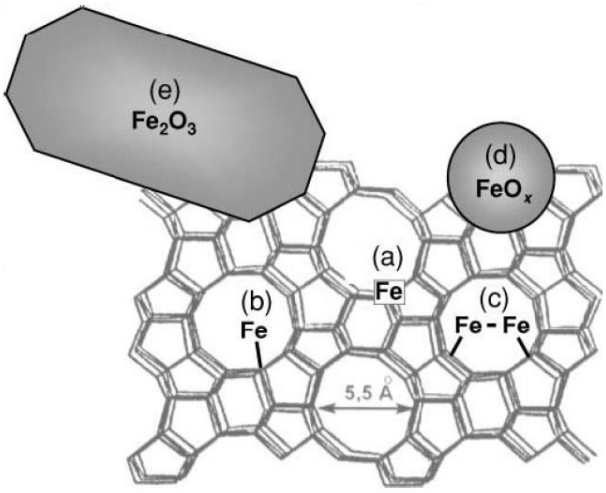

Figure 2.2 Schematic representation of the different Fe species identified in Fe-ZSM-5 (Pérez-Ramírez *et al.*, 2002b).

It is widely accepted that iron oxide (Fe_2O_3) are catalytically unreactive (Panov *et al.*, 1996; Battiston *et al*., 2003a), however, studies shown a remarkable catalytic activity of Fe in the ZSM-5 matrix. The structure of the α-sites has been much discussed in the literature. "They are Fe^{2+} sites, but they do not react with O_2. Only N_2O can oxidize them to Fe^{3+} upon formation of α-oxygen" (Pirngruber and Roy, 2005) and has been compared to the monooxygenases enzyme (Panov *et al.*, 1996). Other suggestions include mononuclear $[FeO]^{3+}$, binuclear oxygen bridged $[HO–Fe–O–Fe–OH]^{2+}$ oligonuclear iron clusters (El-Malki *et al*., 2000; Pirngruber and Roy, 2005; Battiston *et al*., 2003b; Pérez-Ramírez, 2004).

Battiston *et al.* (2003b), using EXAFS to show that the closest Fe–O shell in the complexes can be described with a $[HO–Fe–O–Fe–OH]^{2+}$ core, proposed that the majority of iron appears to be present as Fe-binuclear complexes. After sublimation, most Fe species are present as isolated chloride species in tetrahedral coordination, which upon subsequent hydrolysis and calcination in O_2 at 550 ºC are transformed into oxo-bridged binuclear $[HO\text{-}Fe\text{-}O\text{-}Fe\text{-}OH]^{2+}$ complexes compensating two negative charges of the lattice. These complexes, which can undergo reversible reduction in hydrogen at 500 ºC, account for about 85% of the total Fe content. The remainder of the iron is transformed into Fe_2O_3 upon

hydrolysis and calcination (Marturano *et al.*, 2000). These hydrolysis and calcination treatments, following the sublimation of $FeCl_3$, have been suggested to be the key steps in the formation of the active species in Fe-ZSM-5 zeolites (El-Malki *et al.* 2000). For low iron loadings (Fe=Al < 0.5), it has been reported that iron is present at ion exchange positions in the form of isolated $[FeCl_2]$ species, which upon hydrolysis and calcination are converted into $[Fe(OH)_2]^+$ or $[FeO]^+$ (Pirngruber and Roy, 2005; El-Malki *et al.* 2000).

ZSM-5 has three types of cationic sites, α, β, and γ sites (Figure 2.3). The α-cationic site is easily accessible as it is located in the wall of the straigth channel at the top of a pyramid with the base formed by four oxygen atoms. The β-cationic site in ZSM-5 is easily accessible as it is located in the channel crossing with the cation in an open coordination sphere. The γ-cationic site is located in the sinusoidal channel formed by two five-membered and two six-membered rings in ZSM-5 (El-Malki *et al*., 2000; Sklenak *et al.*, 2010; Wichterlova *et al.*, 2003).

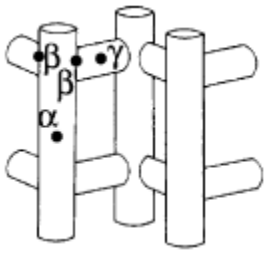

Figure 2.3 Cationic positions within the ZSM-5 (Wichterlova *et al.*, 2003)

Ammonia TPD studies of ZSM-5 showed "three main desorption peaks at about 140, 230 and 490 °C. The peaks observed at 140 °C and 230 °C are caused by weakly adsorbed NH_3 on Lewis acid sites, while the peak at about 490 °C is related to NH_3 adsorbed on Brønsted acid sites" (Brandenberger *et al.* 2009). Using NH_3–TPD–FTIR experiments and DRIFTS measurements, Brandenberger *et al.* (2009) showed that the concentration of Brønsted acid sites decreases with an increase in Fe loading, while the weakly adsorbed NH_3 desorption peaks tend to become larger with increasing iron content and which may be explained by the creation of new Lewis acid sites located on the Fe ion.

Temperature programed reduction (H_2-TPR) studies of Fe-Zeolites display three temperature zones, 240–480 °C, 480–680 °C and >680 °C. The first hydrogen consumption zone below

500 °C resembles the "reduction of Fe^{3+} (bare Fe^{3+} cations and oxo- or hydro-cations such as FeO^{+}, $Fe(OH)^{2+}$ or $[(OH)FeOFe(OH)]^{2+}$) into Fe^{2+}" (Delahay *et al.*, 2005; El-Malki *et al.*, 2000). The high temperature reduction zone above 680 °C is ascribed to the reduction of Fe^{2+} into Fe^{0} upon collapse of the zeolite framework (Delahay *et al.*, 2005; Krishna and Makkee 2006). α-Fe_2O_3 nanoparticles are reduced to Fe_3O_4 and subsequently to FeO at the broad reduction occurrence centred at 327 and 527 °C respectively (Delahay *et al.*, 2005). Brandenberger *et al.* (2011) found "H_2-TPR profiles of various H-ZSM-5 catalysts containing large Fe_2O_3 particles (particle size of 43–65 nm) and nanoparticles (particle sizes of about 22 and 9 nm, respectively) to exhibit broad reduction features between 300 and 650 °C correspond to the reduction sequence, $Fe_2O_3 \rightarrow Fe_3O_4 \rightarrow Fe$ and is in agreement with a H_2 to Fe ratio of 1.5". The typical X-ray powder diffraction pattern of α-Fe_2O_3 iron oxide aggregates, with particle sizes larger than 3–5 nm, shows the most intensive refraction from (1 0 4) and (1 1 0) planes at 33.1° and 35.6° 2Θ, respectively (Delahay *et al.*, 2005).

UV/visible spectroscopy provides information about the nuclearity and concentration of the different iron species corresponding "highly dispersed Fe(III) in/on a solid matrix from isolated hydrated and complexed Fe(III) ions, their hydrated oligomers and condensed nano- or microcrystalline Fe oxides or Fe-bearing silicates" (Wichterlova *et al.*, 2003; Ćapek *et al.*, 2005; Pérez-Ramírez *et al*., 2003). However, the broad overlapping bands and unknown excitation coefficients make quantification inaccurate as it is difficult to discriminate between oligomeric species and oxide particles (Brandenberger *et al.*, 2010b; Kumar *et al.*, 2004).

Absorption bands between 200 and 300 nm are attributed to Laporte-allowed ligand-to-metal charge transfer (LMCT, oxygen to iron) transitions of isolated Fe^{3+} species, either tetrahedrally coordinated in the zeolite framework or extra-framework positions, or octahedrally coordinated in extra framework positions (Wichterlova *et al.*, 2003; Ćapek *et al.*, 2005; Sun *et al.*, 2001; Sun *et al.*, 2006; Brandenberger *et al.*, 2010b; Pérez-Ramírez *et al*., 2003; Chávez-Rivas *et al.*, 2013; Schwidder *et al*., 2005 and Sklenak *et al.*, 2010). Octahedral ferric species in small oligonuclear clusters of Fe_xO_y-type inside the channels are characterized by strong absorptions between 300 and 400 nm, (Wichterlova *et al.*, 2003; Ćapek *et al.*, 2005; Schwidder *et al*., 2005; Sun *et al.*, 2006; Brandenberger *et al.*, 2010b; Chávez-Rivas *et al.*, 2013; Pérez-Ramírez *et al*., 2003 and Sklenak *et al.*, 2010). "The broad peaks at 360 nm and 550 nm in UV–visible spectra of Fe-ZSM-5 catalysts are mainly due to

the d–d transition of Fe^{3+} ion similar to those of Fe_2O_3. These peaks can be assigned to the transition of $^6S \rightarrow {}^4G$ and $^6S \rightarrow {}^4D$, respectively, based upon the Fe^{3+} ion existing in a form of high spin d^5 configuration containing octahedral symmetry" (Park *et al.* 2008). Broad absorption between 600 and 800 nm are assigned to ligand field d–d transitions in hematite (Ćapek *et al.*, 2005; Chávez-Rivas *et al.*, 2013).

Despite the above, UV/visible band assignment must be undertaken with care, as there exist significant discrepancies between the published observations and interpretations. Pirngruber *et al.* (2004) assumed UV bands in the 200 – 300 nm region can be assigned to both Fe monomers and dimers, while Brandenberger *et al.* (2010b) and many other authors assign them exclusively to monomers, however, these bands are also present in spectra of Fe(III) oxides (Smoláková *et al.*, 2010). Moreover, framework and extraframework species, as well as oxidation state, cannot be discriminated in UV/visible spectroscopy (Pérez-Ramírez *et al.*, 2004).

Mössbauer spectroscopy is an ideal tool to study iron species in zeolites. The advantage of Mössbauer spectroscopy is that there is no form of iron that is Mössbauer-unresponsive and iron species in different environments are all observed (Taboada *et al.*, 2005). The only limitation of Mössbauer spectroscopy is its sensitivity whereas low iron containing zeolites cannot successfully be analysed due to low ^{57}Fe isotope levels (Tabor *et al.*, 2011). Three main spectral parameters are used for the description of iron species - Fe isomer shift (IS), quadrupole splitting (QS) and the magnetic hyperfine field (Dubkov *et al.*, 2002; Tabor *et al.*, 2011). See Appendix A-3 for detail description.

Isomer shift reveals information about the s-electron density at the iron nucleus and the oxidation state where isomer shift values in the range 0.1 - 0.6 mm/s are assigned to Fe^{3+} and 0.7 - 1.4 mm/s assigned to Fe^{2+} (Dubkov *et al.*, 2002; Tabor *et al.*, 2011). In oxygen coordinated compounds like Fe-Zeolites, "the primary and the secondary coordination ligands around the iron" ions affects the hyperfine interaction (Taboada *et al.*, 2005). Isomer shifts below 0.3 mm/s at room temperature are usually assigned to Fe^{3+} ions in tetrahedral coordination (Fe^{3+}_{Th}), while isomer shifts above 0.3 mm/s are assigned to octahedral coordination (Fe^{3+}_{Oh}) (Dubkov *et al.*, 2002).

Quadrupole splitting reveals information about symmetry distortion of the Mössbauer atom in the ligand environment. 3d-orbitals have different shapes and different bond energy levels when present in a crystal matrix. In a tetrahedral environment, the e_g orbitals ($z^2–r^2$, $x^2–y^2$) have more favourable bonding overlaps with ligands than the t_{2g} orbitals (xz, yx, xy), whereas, for an octahedral environment the t_{2g} orbitals will have more favourable bonding overlaps than the e_g orbitals (Futz, 2011) . The spectrochemical strength of the ligand as pertained in the crystal field theory compliments the information obtained from the Mössbauer parameters which can reveal changes or differences of the Fe in the zeolite matrix environment (Futz, 2011).

The presence of a Mössbauer sextet is contradictory in the literature, nonetheless, large iron oxide particles with sizes above 8 nm displays a magnetic hyperfine field sextet whereas small particles with sizes below 2 nm display super paramagnetic properties with quadruple splitting and no magnetic hyperfine fields. Magnetic sextets indicate the presence of magnetic oxides, i.e. Fe_2O_3 and/or Fe_3O_4 (Boroń *et al.*, 2013).

El-Malki *et al*., (2000) demonstrated with ESR using samples prepared by both solid-state ion exchange (SSIE) and chemical vapour deposition (CVD) , at low Fe loading (Fe/Al < 0.55) only one kind of mononuclear Fe^{3+} species with a strong rhombic distortion of the tetrahedral coordination of this Fe that fills primarily the α and β sites, however, when the Fe loading increases, another mononuclear Fe^{3+} becomes visible, suggesting a less distorted tetrahedral coordination, which they attributed to a "binuclear complex or even a multinuclear Fe cluster with $[HO\text{-}Fe\text{-}OH]^+$ ion in a cationic exchange position". Similarly, Høj *et al.* (2009) demonstrated with UV/visible, EPR and EXAFS that low iron loadings below 1.2 wt.% produced predominantly iron monomers, whereas , intermediate to high Fe loadings between 2.5 and 5.1 wt.% produced a mixture of monomers, oligomers and hematite particles. With quantitative information they obtained from the UV/visible spectra, a good correlation between activity and monomer content was observed. On the other hand, Li *et al.* (2008) identified in all Fe-Zeolites with "multiple Fe^{3+} species, including isolated Fe^{3+} species (mononuclear or binuclear oxygen bridged), oligonuclear $Fe(III)_xO_y$ clusters and Fe_2O_3 nanoparticles", by means of UV/visible, TEM, H_2TPR and FTIR of adsorbed NO. They propose that only the isolated and oligonuclear iron species contributed to N_2O conversion,

while Fe_2O_3 nanoparticles reduced the accessibility to active sites of isolated/oligonuclear iron species in the channels due to channel blocking.

2.3. Catalytically active sites and the nature of the α-oxygen

Two distinctly different active sites (isolated Fe(III) species), where the α-oxygen reaction takes place, have been identified in the literature, viz. mononuclear $[FeO]^{3+}$ or binuclear oxygen bridged $[HO–Fe–O–Fe–OH]^{2+}$ (El-Malki *et al*., 2000). During the preparation of the Fe-Zeolite, the $FeCl^+$ or $FeCl_2^+$ (attached to the cation exchange position of the zeolite) is hydrolysed and calcined to form the active species (Pérez-Ramírez *et al.*, 2004). Washing was proved to be the key step for the formation of the binuclear Fe complexes, proposed as the catalytically active phase in Fe-ZSM-5 (Marturano *et al.*, (1999).

The conversion of N_2O is a fairly simple reaction which proceeds exclusively on the iron sites yielding gaseous molecular N_2 and O atoms deposited as α-oxygen on the Fe active sites over a broad temperature range (Kaucký *et al.*, 2006). During N_2O temperature programmed desorption (TPD) α-oxygen deposits from at 240 °C and desorbs as molecular O_2 between 365 and 380 °C (Panov *et al.*, 2008). The reactivity of α-oxygen is similar to that of the O^- radical anion (Pirngruber and Roy, 2005).

Kondratenko and Pérez-Ramírez (2007) studied Fe-silicalite with a high proportion of isolated iron species and a relative low degree of iron clustering by transient experiments of N_2O conversion using the temporal analysis of products (TAP) reactor in the temperature range of 500 – 575 °C. They found that N_2 releases instantaneously for 0.5 seconds with the N_2O pulse whereas the O_2 release does not decrease to zero intensity even after 2 seconds at 500 °C (Figure 2.4). In Figure 2.5 they found that the response time (t_{max}) for maximum O_2 release rate decreases from 0.56 to 0.17 seconds upon increasing reaction temperature from 500 to 575 °C, while the change in N_2 response time is much less noticeable from 0.065 to 0.046 seconds. The rate limiting step is a multi-step surface recombination of the deposited α-oxygen desorbing as molecular O_2 and in the process regenerates the active iron site (Kondratenko and Pérez-Ramírez, 2007; Pirngruber and Roy, 2005).

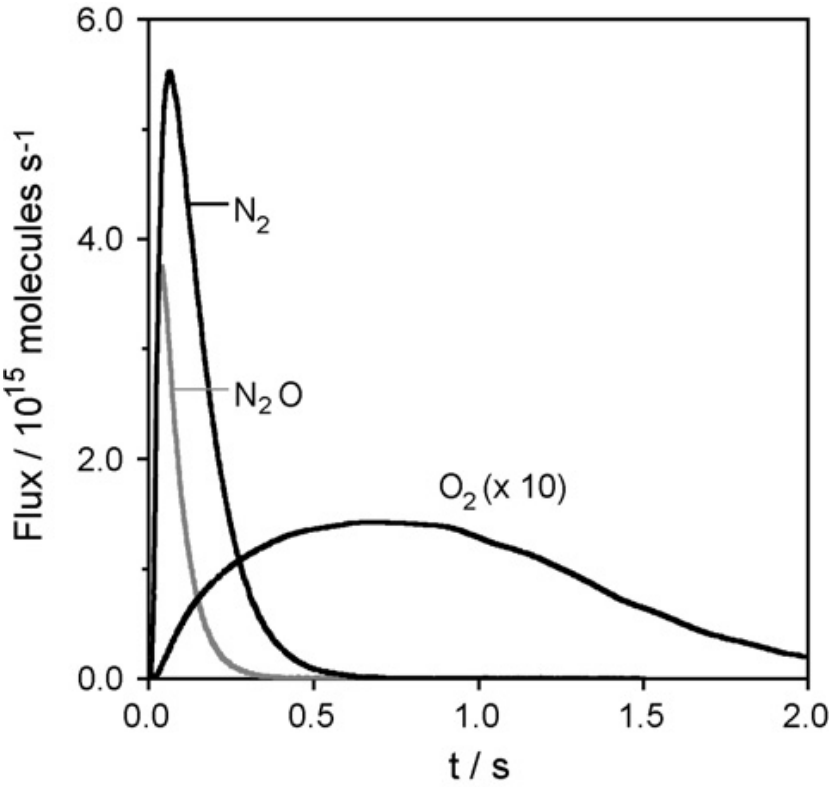

Figure 2.4 Temporal analysis of products (TAP) for N_2O conversion over mononuclear iron sites. Kondratenko and Pérez-Ramírez (2007)

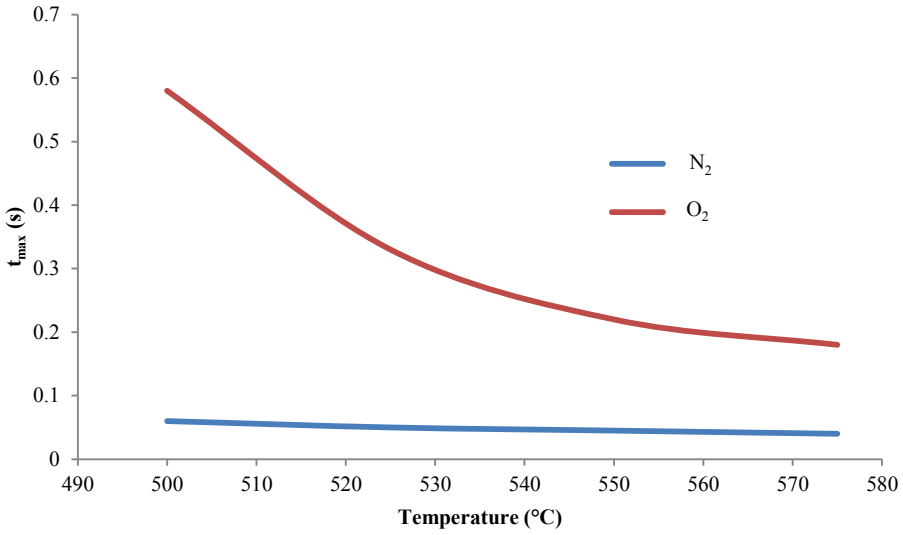

Figure 2.5 Temperature dependency for response time (t_{max}) for maximum O_2 and N_2 release during N_2O conversion. Kondratenko and Pérez-Ramírez (2007)

For isolated Fe^{2+} sites, Pirngruber and Roy (2005) propose that the formation of the α-oxygen occurs as expected, whereas Fe^{2+} can take up only one electron from N_2O and a Fe^{3+}-O^- species is formed in reaction (2).

$$Fe^{2+} + N_2O \rightarrow Fe^{3+}\text{-}O^- + N_2 \quad (2)$$

The formation of the α-oxygen on binuclear oxygen bridge sites is not clear in the literature. Pirngruber and Roy (2005) compared the behaviour of the catalyst after oxidative and reductive pre-treatment by treating either in H_2 or in O_2 at 400 °C. After the pre-treatment with H_2, the O deposited corresponded to one O atom for every two Fe ions in the catalyst, $O_\alpha/Fe_\alpha = 0.5$, as expected from the stoichiometry of Reaction (3):

$$2\ Fe^{2+} + N_2O \rightarrow Fe^{3+}\text{-}O\text{-}Fe^{3+} + N_2 \quad (3)$$

However, experiments by other groups showed that one oxygen atom from N_2O is deposited per active Fe ions, i.e. $O_\alpha/Fe_\alpha = 1$, suggesting that each Fe ion forms α-oxygen in reaction (4) for binuclear sites (Dubkov *et al.*, 2002; Kiwi-Minsker *et al.*, 2003).

$$Fe^{2+}\text{-}\mu\text{-}(OH)\text{-}Fe^{2+} + 2N_2O \rightarrow\ O^-\text{-}Fe^{3+}\text{-}\mu\text{-}(OH)\text{-}Fe^{3+}\text{-}O^- + 2N_2 \quad (4)$$

Furthermore, Jia *et al.*, (2002) have suggested from TPR profiles, in situ XANES and XAFS data, that oxygen atoms deposited via the conversion of N_2O on Fe–ZSM-5 are bonded to Fe^{4+}. Similarly, Guesmi *et al.* (2010) demonstrated with a DFT study that a change of the valence state of binuclear site species occur in which a single or both iron ions obtain a Fe^{4+} valence state.

2.4. The effect of temperature on the active sites.

Yakovlev *et al.*, (2001) studied Fe-ZSM-5 using the DFT approach that N_2O conversion catalysed by oxidized Fe clusters localized in the micropores of Fe-ZSM-5 has a binuclear cluster model of the active site. At temperatures below 200 °C the binuclear site is completely hydroxylated, between 200 and 500 °C the catalytic site has the $[HO\text{-}Fe\text{-}O\text{-}Fe\text{-}OH]^{2+}$ structure, and above 500 °C the site is predominantly $[Fe\text{-}O\text{-}Fe]^{2+}$. They

suggested that a different degree of hydroxylation results in different reaction mechanisms for N_2O conversion. At low temperature and high hydroxylation the active sites are inactive. The other two forms have similar reaction mechanisms of N_2O conversion: "N_2O dissociates on two separate Fe ions followed by oxygen recombination and desorption. The difference between the reaction pathways is that at high temperature (>500 °C) the reaction may involve $Fe^{2+} \rightarrow Fe^{3+}$ transitions, whereas at lower temperatures it is $Fe^{3+} \rightarrow Fe^{4+}$" (Yakovlev *et al.*, 2001). The reaction energy profile for the reactions over two sites, $[OH\text{-}Fe\text{-}O\text{-}Fe\text{-}OH]^{2+}$ and $[Fe\text{-}O\text{-}Fe]^{2+}$ suggesting that hydroxylated site is more favourable for N_2O conversion (Yakovlev *et al.*, 2001). Furthermore, El-Malki *et al.*, (2000) found for samples exposed to O_2 only had a CO_2/Fe ratio of 0.48 during CO-TPR, indicating reduction of Fe^{3+} to Fe^{2+}. In contrast, for the samples that had been exposed to N_2O at high temperature, the CO_2/Fe ratio is significantly higher during CO-TPR, reaching a value of 0.65 that is consistent with the presence of peroxy groups Fe–O–O–Fe (El-Malki *et al.*, 2000).

Pirngruber and Roy (2005) found that during medium temperature treatment between 400 to 600 °C of Fe-Zeolites, dehydroxylation of the Fe^{2+} sites occurs and that it creates vacancies in the coordination sphere of iron and lattice defects above 600 °C which are responsible for the higher catalytic activity (Roy *et al.*, 2007). Similarly, Zhang et al. (2014) showed that increasing the calcination temperature from 550 to 900 °C increased the catalytic activity. In Figure 2.6 the conversion temperature at 80 % N_2O conversion vs the calcination temperature are depicted for results obtained by Zhang *et al.* (2014) and Roy *et al.* (2008). The conversion temperature decreasing as the calcination temperature increases indicating that the catalytic activity increases with increasing calcination temperatures. Pirngruber and Roy (2005) proposed that "the high coordinative unsaturation of the dehydroxylated Fe^{2+} sites allows the deposition of two oxygen atoms from N_2O on one site, which can rapidly desorb as O_2" resulting in an increase of the α-sites at higher temperatures (Dubkov *et al.* 2002).

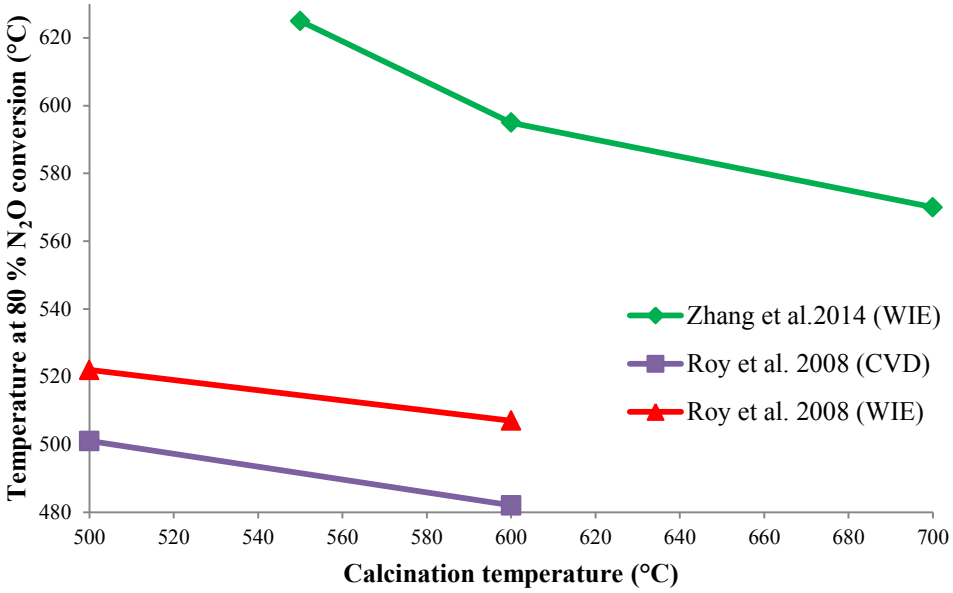

Figure 2.6 The effect of calcination temperature on the temperature at 80 % N_2O conversion Zhang et al., 2014; Roy et al., 2008.

2.5. Reaction mechanism

Given the diversity of the Fe-containing sites present in Fe-ZSM-5, theoretical methods has been used to complement experimental methods in order to obtain a clearer view of what types of Fe sites that might be involved in N_2O conversion to N_2 and O_2, and the mechanism by which this process occurs (Hansen *et al.*, 2007). Heyden *et al.* (2005) have reported the results of a density functional theory (DFT) investigation of the mechanism of the nitrous oxide conversion on mononuclear iron sites and various other groups (Hansen *et al.*, 2007; Guesmi *et al.*, 2010; Kiwi-Minsker *et al.*, 2003) reported results on binuclear oxygen bridged iron sites in Fe-ZSM-5.

Heyden *et al.* (2005) proposed the following mechanism (Figure 2.7) for N_2O conversion over mononuclear iron sites in a density functional theory (DFT) investigation. In the first reaction, N_2O adsorbs onto the zeolite (I) in a reversible adsorption/desorption reaction 9 forming the $Z^-[FeO]^+N_2O$ transitional state (II), which subsequently, decomposes and desorbs molecular nitrogen (N_2) in the irreversible reaction 10 forming the $Z^-[OFeO]^+$ transitional state (III). The reaction path can then proceed via two different paths, reaction 11, 14, 15 and reaction 12, 13, depending on the reaction temperature. Reaction path 11,14,15 is favourable at low temperatures and reaction path 12, 13 are favourable at high temperatures. The O atom

migrates in a reversible surface reaction (11) forming the $Z^-[FeO_2]^+$ transitional state (VI). Both $Z^-[OFeO]^+$ and $Z^-[FeO_2]^+$ are catalytic active to N_2O conversion and should be present under reaction conditions with $Z\text{-}[FeO_2]^+$ as the dominant species. N_2O adsorbs onto the $Z^-[OFeO]^+$ transitional state (III) in the reversible reaction (12) forming the $Z^-[OFeO]^+ON_2$ transitional state (IV), which subsequently, decomposes and desorbs molecular nitrogen in the irreversible reaction (13) forming the $Z^-[OFeO_2]^+$ transitional state (VII). Similarly, N_2O adsorbs onto the $Z^-[FeO_2]^+$ transitional state (V) in the reversible adsorption/desorption reaction (14) forming the $Z^-[FeO_2]^+ON_2$ transitional state (VI), which subsequently, decomposes and desorbs molecular nitrogen (N_2) in the irreversible reaction (15) forming the $Z^-[OFeO_2]^+$ transitional state (VII). $Z^-[O_2FeO]^+$ consists of a superoxide O^{2-} anion and an O^- anion on top of an Fe^{2+} or Fe^{3+} cation. The $Z^-[OFeO_2]^+$ transitional state (VII) decomposes with molecular oxygen (O_2) desorbing and forming $Z^-[FeO]^+$ in the irreversible reaction (16) completing the catalytic cycle.

$$Z^-[FeO]^+_{(s)} + N_2O_{(g)} \leftrightarrow Z^-[FeO]^+(ON_2)_{(s)} \quad (9)$$

$$Z^-[FeO]^+(ON_2)_{(s)} \rightarrow Z^-[OFeO]^+_{(s)} + N_{2(g)} \quad (10)$$

$$Z^-[OFeO]^+_{(s)} \leftrightarrow Z^-[FeO_2]^+_{(s)} \quad (11)$$

$$Z^-[OFeO]^+_{(s)} + N_2O_{(g)} \leftrightarrow Z^-[OFeO]^+(ON_2)_{(s)} \quad (12)$$

$$Z^-[OFeO]^+(ON_2)_{(s)} \rightarrow Z^-[OFeO_2]^+_{(s)} + N_{2(g)} \quad (13)$$

$$Z^-[FeO_2]^+_{(s)} + N_2O_{(g)} \leftrightarrow Z^-[FeO_2]^+(ON_2)_{(s)} \quad (14)$$

$$Z^-[FeO_2]^+(ON_2)_{(s)} \rightarrow Z^-[OFeO_2]^+_{(s)} + N_{2(g)} \quad (15)$$

$$Z^-[OFeO_2]^+_{(s)} \rightarrow Z^-[FeO]^+_{(s)} + O_{2(g)} \quad (16)$$

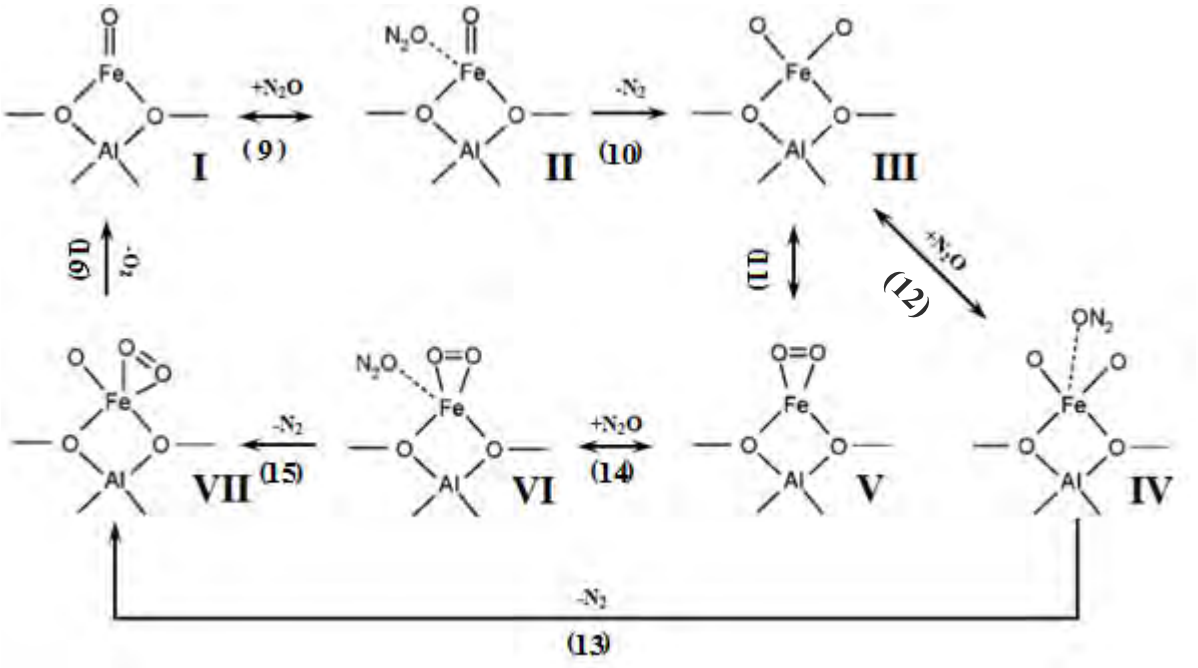

Figure 2.7 Reaction mechanism for the conversion of N_2O over mononuclear iron site (Heyden *et al.*, 2005)

Hansen *et al.* (2007) proposed the following mechanism (Figure 2.8) for N_2O conversion over binuclear oxygen bridged iron sites in a density functional theory (DFT) investigation. In the first reaction, N_2O adsorbs onto the zeolite (I) in a reversible adsorption/desorption reaction (17) forming the $Z^-[FeOFe]^+ON_2$ transitional state (II), which subsequently, decomposes and desorbs molecular nitrogen (N_2) in the irreversible reaction (18) forming the $Z^-[OFeOFe]^+$ transitional state (III). Similarly, N_2O adsorbs onto the $Z^-[OFeOFe]^+$ transitional state (III) in the reversible reaction (19) forming the $Z^-[OFeOFe]^+ON_2$ transitional state (IV), which subsequently, decomposes and desorbs molecular nitrogen in the irreversible reaction (20) forming the $Z^-[OFeOFeO]^+$ transitional state (V). The O atom migrates in a reversible surface reaction (21) forming the peroxo (O_2^{2-}) $Z^-[FeOOFeO]^+$ transitional state (VI) followed by the reversible surface reaction (22) forming the superoxide (O_2^-) $Z^-[FeO_2FeO]^+$ transitional state (VII) after which it rearranges by the reversible surface reaction (23) forming the superoxide (O_2^-) $Z^-[FeOFeO_2]^+$ transitional state (VIII) placing the superoxide O_2^- anion in a favourable position to desorbs. Subsequently, molecular oxygen (O_2) desorbs in an irreversible reaction (24) forming $Z^-[FeOFe]^+$ completing the catalytic cycle.

$$Z^{-}[FeOFe]^{+}_{(s)} + N_2O_{(g)} \leftrightarrow Z^{-}[FeOFe]^{+}ON_{2(s)} \quad (17)$$

$$Z^{-}[FeOFe]^{+}ON_{2(s)} \leftrightarrow Z^{-}[OFeOFe]^{+}_{(s)} + N_{2(g)} \quad (18)$$

$$Z^{-}[OFeOFe]^{+}_{(s)} + N_2O_{(g)} \leftrightarrow Z^{-}[OFeOFe]^{+}ON_{2(s)} \quad (19)$$

$$Z^{-}[OFeOFe]^{+}ON_{2(s)} \leftrightarrow Z^{-}[OFeOFeO]^{+}_{(s)} + N_{2(g)} \quad (20)$$

$$Z^{-}[OFeOFeO]^{+}_{(s)} \leftrightarrow Z^{-}[FeOOFeO]^{+}_{(s)} \quad (21)$$

$$Z^{-}[FeOOFeO]^{+}_{(s)} \leftrightarrow Z^{-}[FeO_2FeO]^{+}_{(s)} \quad (22)$$

$$Z^{-}[FeO_2FeO]^{+}_{(s)} \leftrightarrow Z^{-}[FeOFeO_2]^{+}_{(s)} \quad (23)$$

$$Z^{-}[FeOFeO_2]^{+}_{(s)} \leftrightarrow Z^{-}[FeOFe]^{+}_{(s)} + O_{2(g)} \quad (24)$$

Isolated Fe cations in the form of $Z^{-}[FeO]^{+}$ were found to be the most active centres for N_2O conversion (Hansen *et al.*, 2007; Heyden *et al.*, 2005). Similarly, Li *et al.* (2011) found during the oxidation of benzene to phenol that the initial formation of the reactive oxygen atom via the dissociation adsorption of N_2O is considerably less favourable for the binuclear complexes compared to mononuclear iron sites. However, El-Malki *et al.* (2000) found that binuclear sites and larger clusters are more active for N_2O conversion than mononuclear sites.

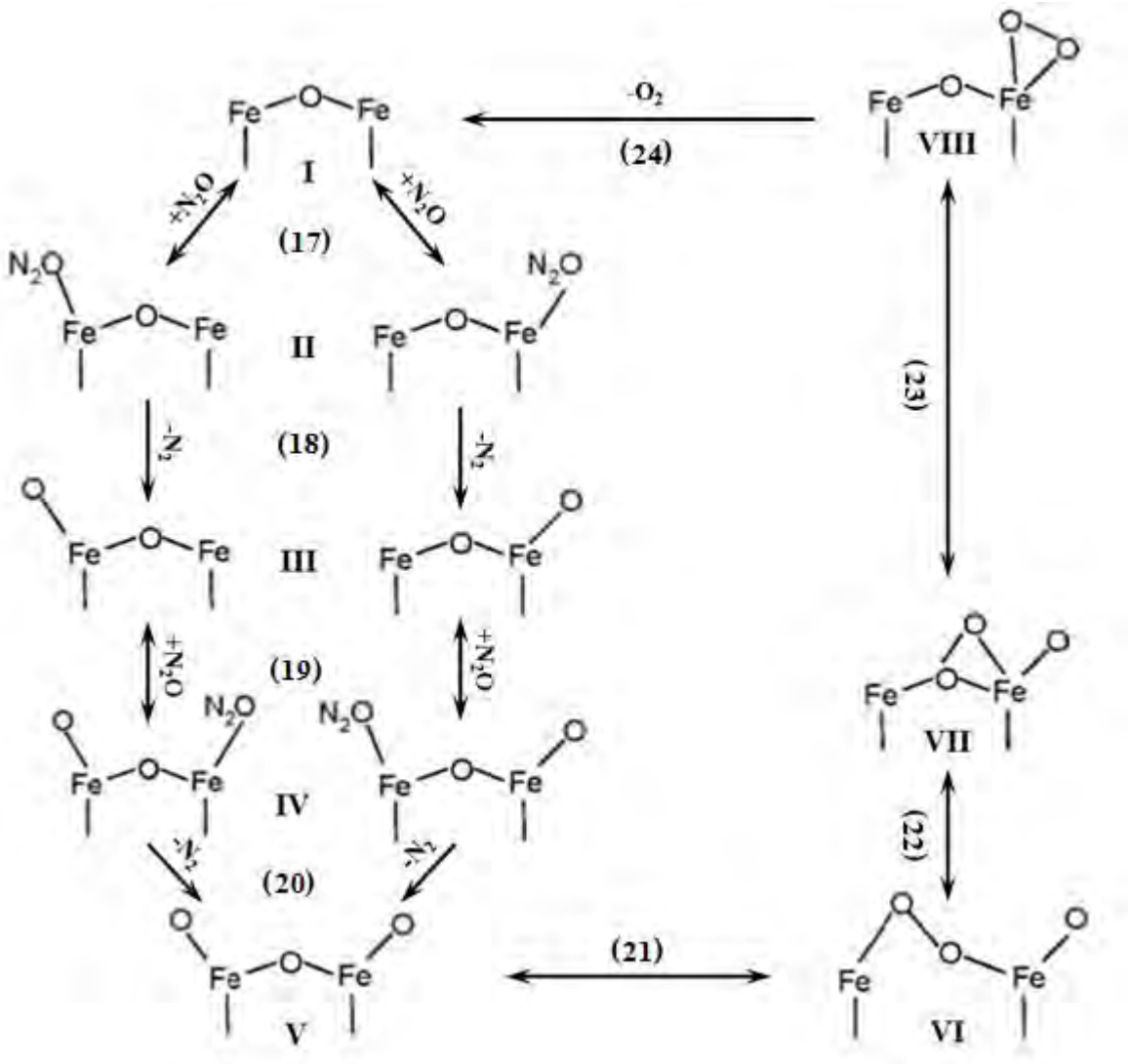

Figure 2.8 Reaction mechanism for the conversion of N_2O over binuclear iron site (Hansen *et al.*, 2007)

2.6. Reaction kinetics

Numerous studies of the mechanism and kinetics of N_2O conversion over iron-containing zeolites have been published in the literature. Fu *et al.* (1981) studied the conversion of N_2O by Fe(III)Y zeolite between 350 and 650°C. They found that the "concentration of oxygen in the gas stream had no apparent effect on the conversion rate of N_2O".

Although there is wide agreement that O_2 formation is rate-determining step, there is no consensus on the reaction pathways leading to gas-phase O_2. Two distinctly different active sites (isolated Fe^{3+} species) have been identified in the literature, viz. mononuclear $[FeO]^{3+}$ or binuclear oxygen bridged $[HO–Fe–O–Fe–OH]^{2+}$ (El-Malki *et al*., 2000).

In Figure 2.9 N_2O conversion curves over the mononuclear and binuclear oxygen bridged iron sites from the theoretical DFT investigation by Heyden *et al.* (2005) and Hansen *et al.* (2007). In Figure 2.10 Arrhenius plots over the mononuclear iron sites by Heyden *et al.* (2005) and in Figure 2.11 binuclear oxygen bridged iron sites (1ppb H_2O) by Hansen *et al.* (2007) indicating that the conversion is more favourable over mononuclear iron sites compared to binuclear iron sites by approximately 4 times. The gradual slope change between 390 and 500 °C of the Arrhenius plot in Figure 2.10 for the mononuclear iron site indicates that it gradually increases in activity as the reaction temperature increases due to the shift from $Z^-[FeO_2]^+$ (reaction 11) to $Z^-[OFeO]^+$ resulting in a higher rate due to the lower activation energy for the conversion of $Z^-[OFeO]^+ON_2$ to $Z^-[OFeO_2]^+$ (reaction 13) compared to the conversion of $Z^-[FeO_2]^+ON_2$ to $Z^-[OFeO_2]^+$ (reaction 15) (Heyden *et al.*, 2005).

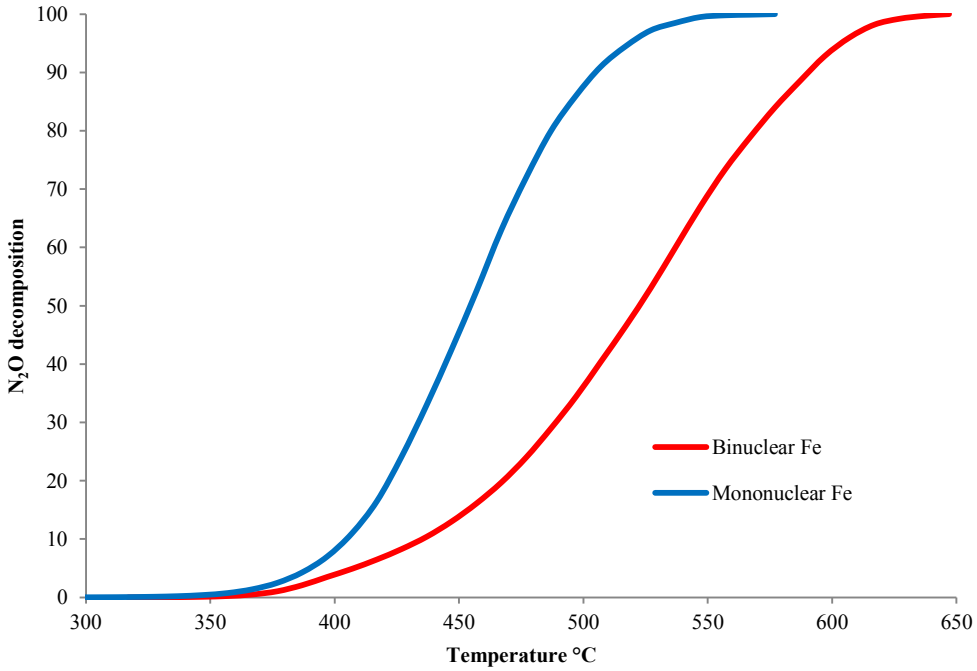

Figure 2.9 N_2O conversion curves over mononuclear and binuclear oxygen bridged iron sites (Hansen *et al.*, 2007).

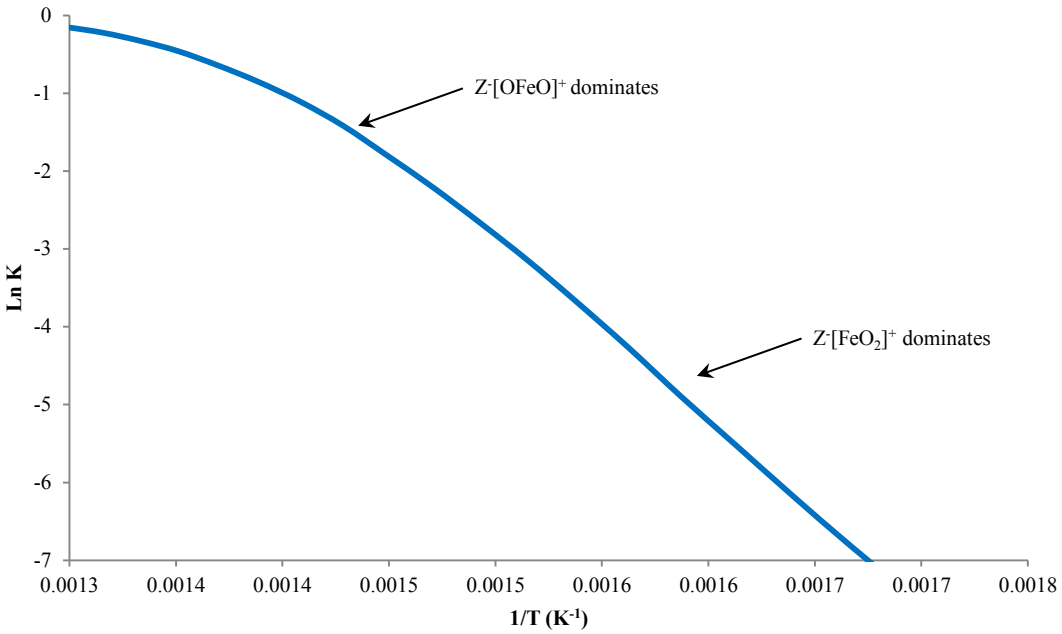

Figure 2.10 Arrhenius plots for N_2O conversion curves over mononuclear (Heyden *et al.*, 2005).

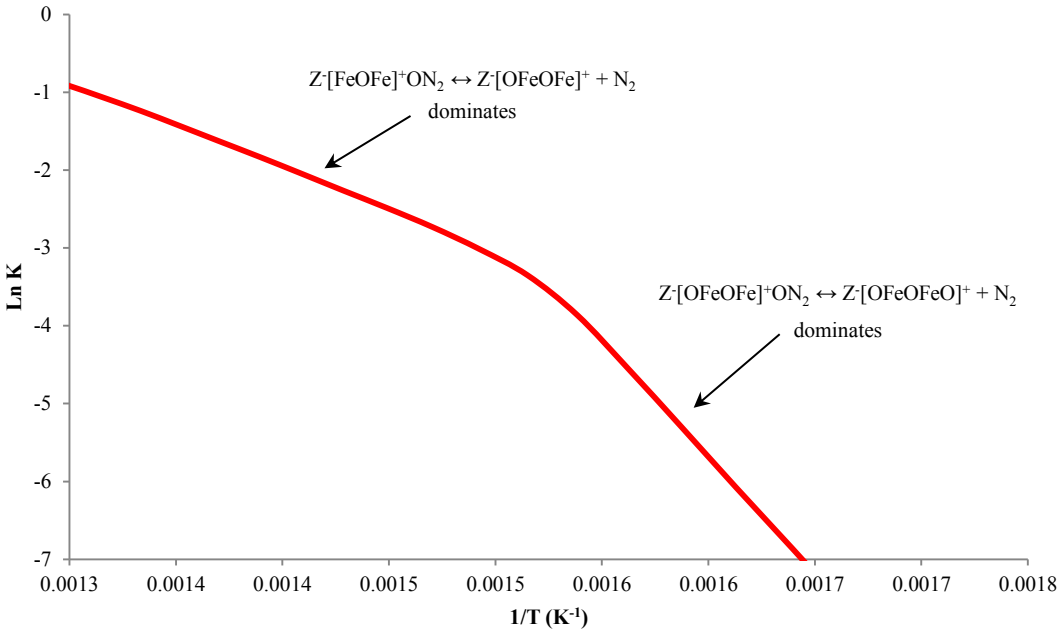

Figure 2.11 Arrhenius plots for N_2O conversion curves over binuclear oxygen (1 ppb H_2O) bridged iron sites (Hansen *et al.*, 2007).

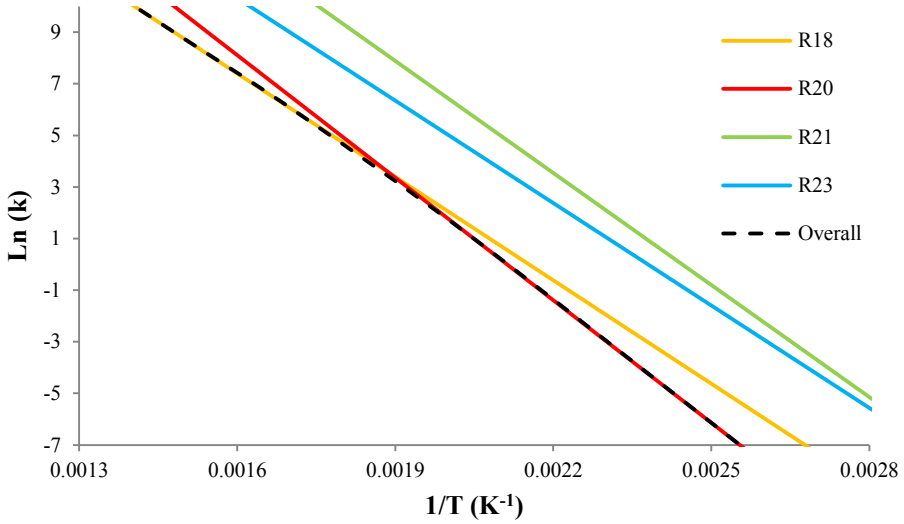

Figure 2.12 Arrhenius plot for the binuclear iron site for reactions 18, 20, 21, 23 and the overall rate limiting curve modelled with DFT by Hansen *et al.* (2007).

In Figure 2.11 the Arrhenius plot for the N_2O conversion reaction (1 ppb H_2O) modelled with DFT by Hansen *et al.* (2007) over binuclear oxygen bridged iron sites has two gradients, below and above 375 °C which is an indication of a mechanism change. Contrary, to the mononuclear iron site where the limiting steps were the surface oxygen reactions, the limiting reactions over the binuclear bridged oxygen site are the conversion of the N_2O to surface oxygen and the desorption of the molecular nitrogen. In Figure 2.12, initially the rate limiting step below 375 °C is the conversion of $Z^-[OFeOFe]^+ON_2$ to $Z^-[OFeOFeO]^+$ and N_2 (reaction 20) and at higher temperatures the conversion of $Z^-[FeOFe]^+ON_2$ to $Z^-[OFeOFe]^+$ and N_2 (reaction18) with the overall reaction progressing over the two limiting reactions (reaction 18 and 20). Reaction 21 and 23, the surface reaction, do not constitute to the limiting reactions.

3. Objectives of the study

This study consists of two parts, the first of which attempts to gain a deeper understanding of the solid-state ion exchange process and the dynamics involved. The process is evaluated at different stages before, during and after ion exchange, and during calcination. The study seeks to evaluate the two ion exchange mechanisms which are reported in the literature – contact induced ion exchange or ion exchange during thermal treatment. Powder X-ray diffraction, physical adsorption and thermal gravimetric analysis are employed to characterise the process.

The second part of the study looks at the characteristics of low, medium and high activity catalysts and the effect of the calcination temperature during extruding with a binder.

The study seeks to evaluate

- The nature of the iron species and their effect on catalytic activity.
- The relationship between the α-oxygen content and the catalytic activity.
- The effect of temperature during final calcination of the extruded catalyst.

4. Experimental

Details of the analytical methods employed are presented below mostly in terms of the experimental apparatus conditions and parameters applied. For the case of the less 'common' methods employed, viz. micropore adsorption, temperature programmed methods and Mössbauer spectroscopy, further general descriptions of these methods are provided in sections A-1, A-2 and A-3 respectively of Appendix A.

4.1. Preparation of the samples

Commercial NH_4-ZSM-5 (Clariant SM27) was used as the ZSM-5 zeolite substrate with a SiO_2:Al_2O_3 ratio of 27 containing approximately 5 % moisture. This substrate was subsequently converted into a range of experimental materials (powders) in the laboratory (section 4.1.1). In the second part of the study, commercial plant catalysts shaped into extrudates and calcined either in the commercial plant or in the laboratory (section 4.1.2) were used.

4.1.1. Powder catalytic materials

Table 4.1 summarises the laboratory prepared materials. The powder SM27 substrate, as prepared in the plant, is referred to as Z0. This same material from the same commercial batch was converted to the acid form (H-ZSM-5) via calcination in air for 6 hours at 500 ºC is referred to as Z500. Both these materials comprise zeolite only.

Solid-state ion exchanged materials were prepared by grinding powder SM27 substrate (material Z0 from the same commercial batch as Z0 and Z500) with $FeCl_2.4H_2O$ (Merck) in a vibrating mill at a 2:1 total Al to Fe molar ratio and subsequent calcination in air for 6 hours in a laboratory furnace in absence of air at 120, 200, 300, 400 and 500 ºC, individually. These materials are referred to as M0 (uncalcined), M120, M200, M300, M400 and M500 respectively.

Table 4.1 Powder sample identification – laboratory ground and calcined

Sample	Starting material	Calcination Temperature
Z0[a]	NH_4-ZSM-5	Ambient
Z500[b]	NH_4-ZSM-5	500 °C
M0[c]	NH_4-ZSM-5 + $FeCl_2.4H_20$	Ambient
M120[d]	NH_4-ZSM-5 + $FeCl_2.4H_20$	120 °C
M200[d]	NH_4-ZSM-5 + $FeCl_2.4H_20$	200 °C
M300[d]	NH_4-ZSM-5 + $FeCl_2.4H_20$	300 °C
M400[d]	NH_4-ZSM-5 + $FeCl_2.4H_20$	400 °C
M500[d]	NH_4-ZSM-5 + $FeCl_2.4H_20$	500 °C

a. As received from the commercial plant.
b. Sample Z0 laboratory calcined for 6 hours in air.
c. As laboratory ground.
d. Laboratory calcined for 6 hours in the absence of air at the specified temperature.

4.1.2. Shaped catalyst (extrudates)

Fe-ZSM-5 catalysts were prepared in the commercial plant from SM27 substrate and $FeCl_2.4H_2O$ in the same way as described for material M0 (section 4.1.1), followed by calcination in air at 500 ºC, mixing with an alumina binder and extruded (1/10" diameter) in a commercial plant. Fully commercial catalysts are subsequently produced by calcining this material in the commercial plant at 500 ºC in air for 5 hours. Similarly, experimental catalysts were prepared from commercial plant produced extrudates (uncalcined) by calcination in a laboratory furnace at temperatures 500, 550, 600, 650 and 900 ºC in air for 5 hours and are referred to as Fe-ZSM-5/500, Fe-ZSM-5/550, Fe-ZSM-5/600, Fe-ZSM-5/650 and Fe-ZSM-5/900 respectively (Table 4.2).

A number of samples with different N_2O conversion catalytic activities were selected from commercial production to characterise the material. Samples were selected from different plant produced batches with high-, mid- and low-range N_2O conversion catalytic activity (see section 4.2.9 for test method) and referred to as High-Fe-ZSM-5, Mid-Fe-ZSM-5, Low-Fe-ZSM-5 (Table 4.3). The commercial catalyst, EnviNOx® has a N_2O conversion (see section 4.2.9 for test method) specification ≥ 84 %.

Table 4.2 Shaped samples, laboratory calcined at different temperatures for 5 hours

Samples	Calcination temperature (in air)
Fe-ZSM-5/500[a]	500 ºC
Fe-ZSM-5/550[a]	550 ºC
Fe-ZSM-5/600[a]	600 ºC
Fe-ZSM-5/650[a]	650 ºC
Fe-ZSM-5/900[a]	900 ºC

a. Laboratory calcined for 5 hours in air at the specified temperature.

Table 4.3 Shaped catalyst samples studied with different activity

Samples	Activity N_2O conversion[a]
High Fe-ZSM-5	90.3 %
Mid Fe-ZSM-5	85.9 %
Low Fe-ZSM-5	71.0%

a. 1 000 ppm N_2O, 100 ppm NO, 2.5 % O_2 and 3 100 ppm H_2O in nitrogen at 10 000 h^{-1} at 425 °C.

4.2. Physicochemical characterisation methods

4.2.1. Powder X-ray diffraction

X-ray diffractograms were recorded on a Perkins diffractometer using Cu-K_α radiation in the range 5° – 50° 2θ, in 0.1° intervals at a scanning rate of 0.05°/s.

For X-ray analysis, the solid-state ion exchanged materials (Table 4.1) were transferred to a desiccator right after calcination where they were allowed to cool to room temperature. Similarly, shaped catalyst samples were calcined in the laboratory (Table 4.2) or received from the plant were dried at 120 ºC for 4 hours (Table 4.3) and then transferred to a desiccator were they were allowed to cool to room temperature. All series of samples were analysed one after another under unaltered instrumental conditions.

4.2.2. Surface area and porosity

Nitrogen adsorption isotherms were performed at liquid nitrogen temperature using a Micromeritics TRISTAR 3020 instrument. 0.1 g of sample was outgassed in vacuum at 300 ºC or at the calcination temperature if that temperature was lower (as in the case of M0, M120 and M200, see Table 4.1) for 16 hours prior to measurements.

The Brunauer-Emmet-Teller (BET) model for multilayer adsorption was applied for the determination of the adsorbate monolayer volume (V_m) and the surface area of the material. The micropore volume (pores with pore sizes smaller than 20 Å) was determined via the t-plot method and the pore sizes were determined by the MP model. The mesoporosity (pore sizes between 20 and 500 Å), was determined by the BJH method (Barrett, Joyner and Halenda method). The ultra-micropore volumes (pore sizes below 7 Å) were determined in accordance with the Dubinin-Radushkevich and the Dubinin-Astakhov methods.

For a more detailed description of the physical adsorption methods employed, refer to section A-1 in Appendix A.

4.2.3. Differential thermogravimetric analysis (DTGA)

Thermogravimetric analysis was conducted on the uncalcined, milled material, M0, on a NETZSCH STA 409 PC/PG instrument coupled to a QMS 403 D Aëolos® mass spectrometer. 25 mg of sample were heated to 500 ºC at a rate of 5 ºC/min in nitrogen with the sample weights recorded at 1 second intervals. Molecular masses of 18, 36 and 53 were used for H_2O, HCl and NH_4Cl identification, respectively.

For more detailed descriptions of temperature programmed methods see Appendix A.2.

4.2.4. Ammonia temperature programmed desorption (TPD)

Ammonia TPD was performed using a Micromeritics AutoChem II 2920 instrument. A 0.3 g sample was pre-treated by heating to 500 ºC at 10 ºC/min and kept at this temperature for 30 minutes in helium (5 cm^3/min STP). The sample was subsequently cooled to 120 ºC, saturated with 10 % (v/v) ammonia (Afrox, NH_3 = 10.0 %, He = 89.999%) in helium at 20 cm^3/min for 6 minutes, flushed with 20 cm^3/min helium (Afrox, He > 99.999%) at STP to remove excess ammonia until the baseline of the TCD was constant, whereafter it was heated at 10 ºC/min to 700 ºC. TCD concentrations were recorded at 1 second intervals.

TCD calibration was performed with mixtures of known concentrations of ammonia in helium (Afrox, NH_3 = 10.0 %, He = 89.999%) obtained from Afrox.

For more detailed descriptions of temperature programmed methods see Appendix A.2.

4.2.5. Temperature programmed N_2O conversion

Temperature programmed conversion of N_2O (4.8 vol % in helium) was conducted on a Micromeritics AutoChem II 2920 instrument. The catalysts were hydrated in demineralised water at 80 ºC for two hours followed by drying at 120 ºC. 0.3 g of catalyst was heated at a rate of 10 ºC/min to 500 ºC and kept at this temperature for 30 minutes in a stream of helium (5 cm^3/min at STP). The sample was subsequently cooled to 120 ºC and the gas flow was

changed to 20 cm^3/min helium (Afrox, He > 99.999%) and 1 cm^3/min N_2O (Afrox, N_2O > 99.9%) at STP, followed by heating to 600 ºC at a rate of 10 ºC/min. The unreacted N_2O in the effluent gas was trapped in a liquid nitrogen cold trap after which the gas (containing N_2 and O_2, the products from the conversion of N_2O) was analysed with a thermal conductivity detector (TCD).

The TCD calibration curve (Figure 4.1) was determined by comparing the TCD reading with unreacted N_2O (reaction gas bypassing the sample and the cold trap) and with fully decomposed N_2O in N_2 and O_2 (reaction gas passing through the sample and the cold trap at 600 °C) which had the same numeric value.

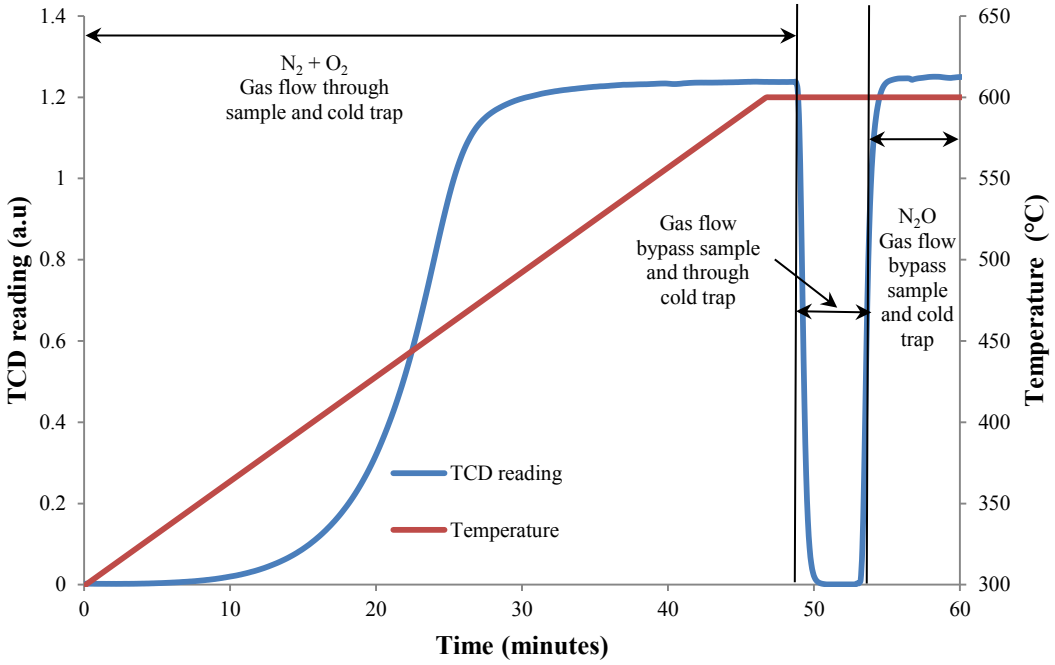

Figure 4.1 TCD calibration curve for temperature programmed N_2O conversion over samples Fe-ZSM-5 (TCD signal for N_2+O_2 and N_2O concentration, N_2O 4.8 vol % in helium, 10 ºC/min).

The concentration of reactive surface oxygen (α-oxygen) was determined from the N_2O temperature programmed conversion curves as described in the previous paragraph by integrating the area below the TCD peak between 200 and 350 °C, assuming that the oxygen atoms formed upon conversion of the N_2O were retained by adsorption on the catalyst and only nitrogen molecules desorb so that the amount of O could be calculated back. α-Oxygen deposits from N_2O at 240 °C and desorbs O_2 between 365 and 380 °C (Panov *et al.*, 2008).

For more detailed descriptions of temperature programmed methods see Appendix A.2.

4.2.6. Temperature programmed reduction (TPR)

Temperature programmed reduction of catalyst samples with ammonia was performed directly after the temperature programmed N_2O conversion (section 4.2.3). The sample was cooled to 100 ºC in 5 cm^3/min helium, where after, the gas flow was changed to 20 cm^3/min 1% (v/v) ammonia (Afrox, NH_3 = 10.0 %, He = 89.999%) in helium (Afrox, He > 99.999%) at STP. Once the TCD reading was constant the sample was heated to 800 ºC at a rate of 10 ºC/min. Unreacted ammonia and H_2O in the effluent gas were trapped in a liquid nitrogen cold trap before TCD analysis. TCD concentrations of the N_2 (product from the oxidation of ammonia) were recorded at 1 second intervals.

For more detailed descriptions of temperature programmed methods see Appendix A.2.

4.2.7. Diffuse reflectance UV/visible spectroscopy

Diffuse reflectance UV/visible spectra of the hydrated Fe-zeolite samples were collected in the range from 200 to 800 nm using a Perkin–Elmer Lambda 950 spectrometer equipped with a Spectralon™ integration sphere.

Band assignments are in accordance with literature. Bands between 200 and 300 nm are assigned to tetrahedral coordination isolated Fe^{3+} species (Schwidder *et al.*, 2006). Octahedrally coordinated ferric species in small Oligomeric Fe_xO_y in zeolite channel are characterized by strong absorptions bands between 300 and 400 nm (Wichterlova *et al.*, 2003; Ćapek *et al.*, 2005; Schwidder *et al.*, 2006; Sun *et al.*, 2006; Brandenberger *et al.*, 2010b; Pérez-Ramírez *et al.*, 2003; Sklenak *et al.*, 2010). The broad absorption bands between 400 and 600 are assigned to Fe_2O_3 clusters on the external zeolite surface and the bands between 600 and 800 nm are assigned to Fe^{3+} oxides and hydroxides (Chávez-Rivas *et al.*, 2013).

4.2.8. Mössbauer spectroscopy

The ideal radioactive source used in the study of iron based systems is ^{57}Co. In this work, a 10 mCi ^{57}Co source sealed in rhodium matrix was used.

In the present set-up, the source was mounted to a velocity transducer which was operated at a frequency of 6 Hz and oscillated at constant acceleration. The electromechanical drive system consists of the Mössbauer driving unit (MDU) model MR-350, function generator (FG) model FG-351 and a multi-channel scaling PCA3 card (supplied by Oxford Instruments) mounted in a computer.

About 0.2 g of fine powder from each sample was used as an absorber at ambient temperature. The detection system was placed behind the absorber and comprised of the detector plus power supply, a pre-amplifier (Tennelec, TC174) and a main amplifier (Tennelec, TC202BLR). The detectors used were Xe, CO_2 (tube type: 4546, operational voltage 2176 V) and Kr, CO_2 (tube type: 45431, operational voltage 1789 V) gas filled proportional counters (from LND, INC., USA). The γ-ray photons detected are those that are transmitted through the absorber. The 14.41 keV energy level has a mean lifetime of l.4x 10^{-7} s and a line width of r = 4.6 x 10^{-9} eV.

A 25 μm thick iron foil absorber at room was used for velocity calibration of the zero velocity channel (ZVC) and calibration factors (CF) of the Mössbauer spectrometer. Isomer shift values are referenced to metallic α-iron with a positional accuracy of ±0.03 mm/s. Spectrum deconvolution was performed by assuming Lorentzian line shapes.

4.2.9. Catalytic activity for N_2O conversion

N_2O conversion was carried out at 1.5 bar (absolute pressure) and 425 ºC in a fixed bed quartz reactor (18 mm i.d.), charged with 7.25 g catalyst at a gas hourly space velocity (GHSV) of 10 000 h^{-1}. The gas was a mixture of 1 000 ppm N_2O, 100 ppm NO, 2.5 % O_2 and 3 100 ppm H_2O in nitrogen - similar to the off gas composition of a typical nitric acid plant (Groves *et al.*, 2006). The inlet and outlet gas compositions were measured by FTIR

spectroscopy, making use of a two directional bypass system measuring both streams on the same analysers.

The N_2O conversion activity for all commercial catalysts High-Fe-ZSM-5, Mid-Fe-ZSM-5, Low-Fe-ZSM-5 are presented in Table 4.3 (section 4.1.2).

The test for the temperature programmed N_2O conversion test method in section 4.2.5 is dry gas (containing no moisture), containing no NO and O_2 with a N_2O concentration of 4.8 % in helium whereas the Catalytic activity N_2O conversion test gas composition is a mixture of 1 000 ppm N_2O, 100 ppm NO, 2.5 % O_2 and 3 100 ppm H_2O in nitrogen. Moisture depresses the N_2O decomposing catalytic activity whereas NO enhances it (Kaucký *et al.*, 2006; Park *et al.*, 2008; Pérez-Ramírez *et al.*, 2002a; Xia *et al.*, 2010), for this reason differences are expected between the respective test results.

5. Results

5.1. Structural/crystallographic characterisation

Powder XRD measurements were performed in order to follow the process of contact-induced ion exchange between ZSM-5 and ferrous chloride during milling and calcination. Details of the procedure are described in section 4.2.1. Figure 5.1 compares the XRD patterns of the NH_4-ZSM-5 and ferrous chloride mixture as milled at ambient temperature, M0, and calcined at 120, 200 and 300 °C (samples M120, M200 and M300) as well as ferrous chloride and ammonium chloride. As can be seen from Figure 5.1, all samples maintain the characteristic pattern of the ZSM-5 topology and no ammonium chloride reflections are visible during any stage of the solid-state ion exchange process (milling and calcination). No ferrous chloride reflections are visible in the uncalcined, milled sample M0. However, upon heating the material (samples M120 and M200) two reflections appear at 38.4 ° and 44.6 ° matching ferrous chloride, which are present up to 200 °C. The strong reflection at 38.4 ° which appeared after heating to 120 °C (sample M120), intensifies by heating to 200 °C (sample M200). The second reflection at 44.6 ° of approximately half the intensity of the 38.4 ° reflection of the 120 °C (sample M120) weakens upon heating to 200 °C (sample M200) and reduces to approximately 25 % of its original (120 °C) intensity. Both reflections disappear on heating to 300 °C (sample M300).

In Figure 5.2 it is shown that the relative crystallinity of the Fe-ZSM-5 solid-state ion exchanged sample calcined at 500 °C (M500), is considerably lower than that of the parent zeolite (Z500) calcined at 500 °C as determined by the relative intensities of the principal structural reflections at around 24° 2θ. In Figure 5.3 the intensities of the reflections at approximately 9° 2θ of the ground sample M0 are compared to the intensities of the respective reflections of the ground and calcined samples M120, M200, M400 and M500. The intensities of the reflections decrease by approximately one third from those of the ground sample, M0, upon heating to 120 °C (sample M120). On further heating, the intensities of the reflections increase slightly, and upon heating to 500 °C (sample M500) eventually increase beyond their intensities in the uncalcined sample (M0).

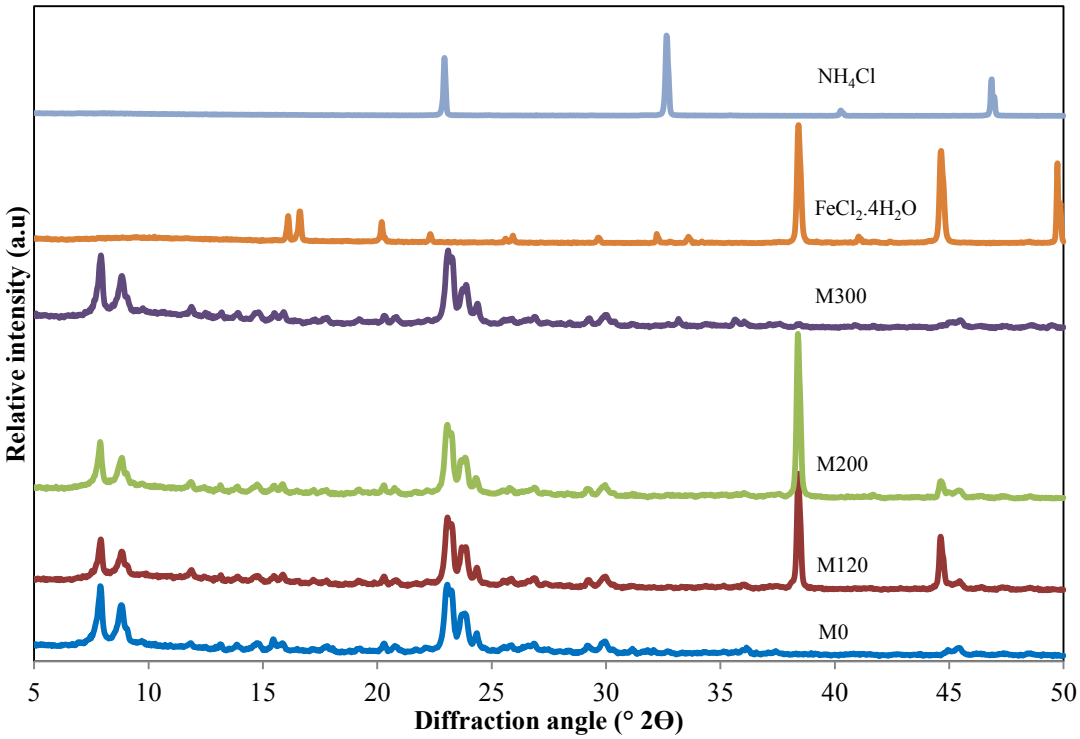

Figure 5.1 Powder XRD patterns for M0, M120, M200, M300, $FeCl_2.4H_2O$ and NH_4Cl

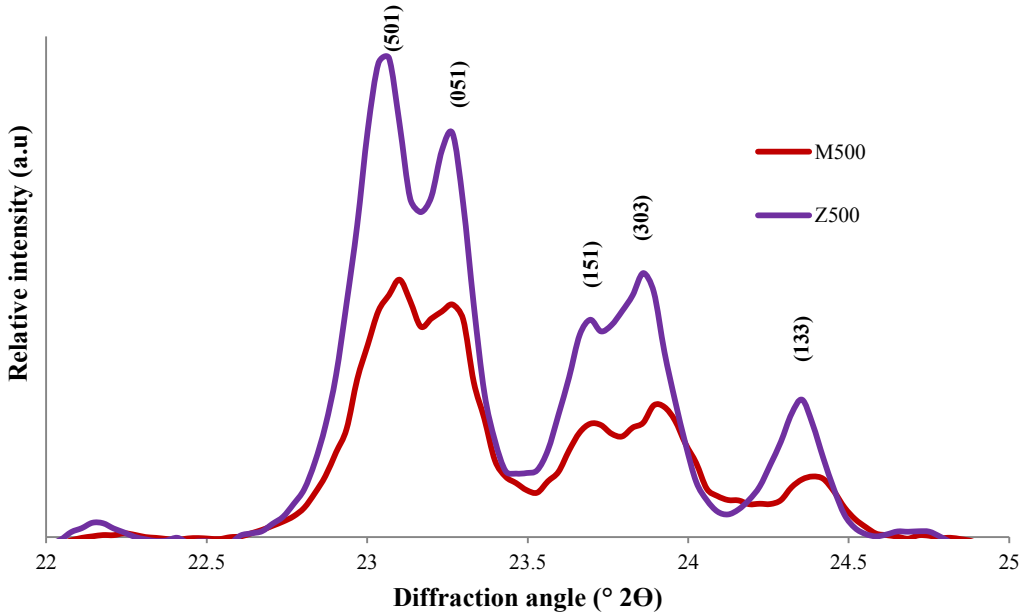

Figure 5.2 Section of powder XRD patterns of M500, and Z500

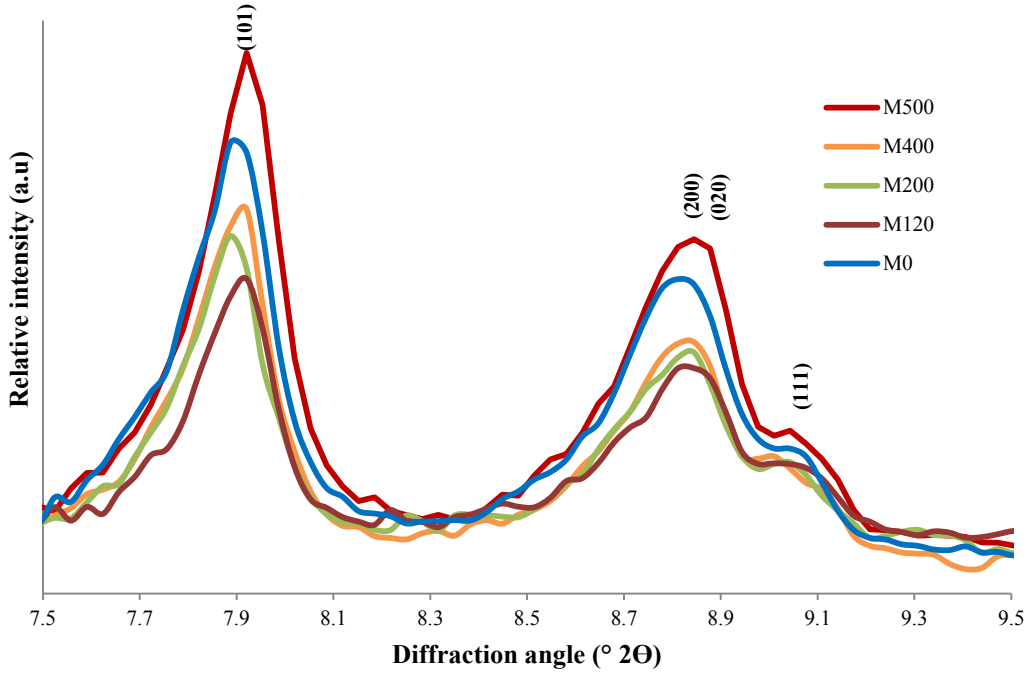

Figure 5.3 Section of powder XRD patterns of M0, M120, M200, M400, and M500

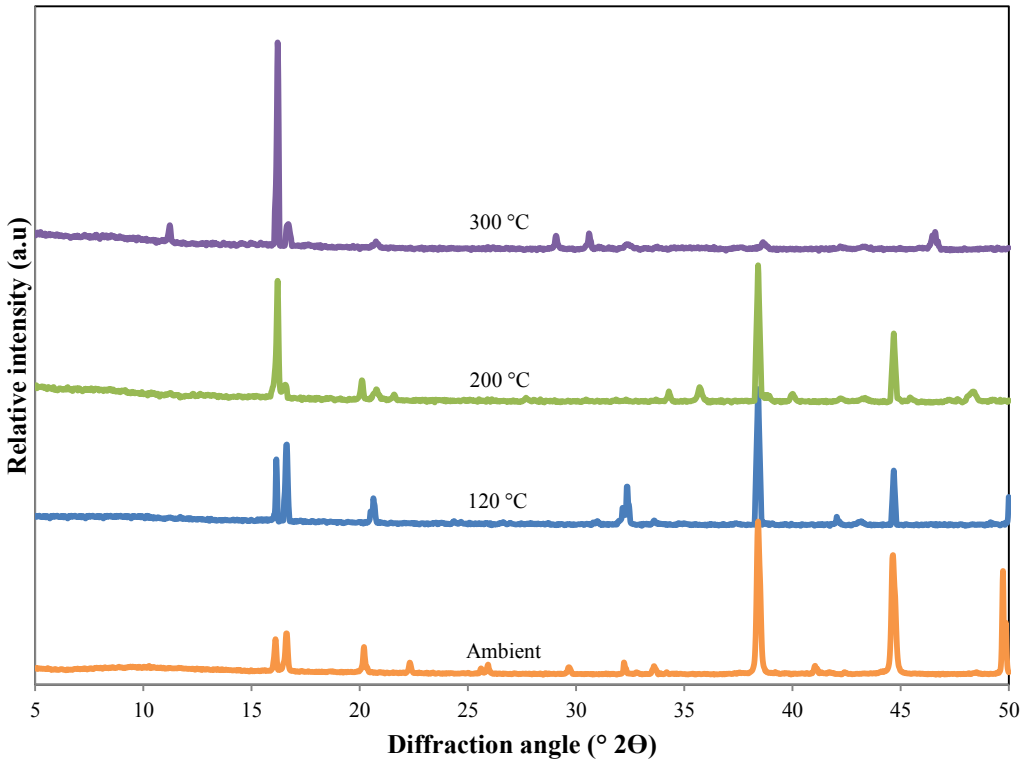

Figure 5.4 Powder XRD patterns for $FeCl_2.4H_2O$ at ambient temperature, 120, 200 and 300 °C

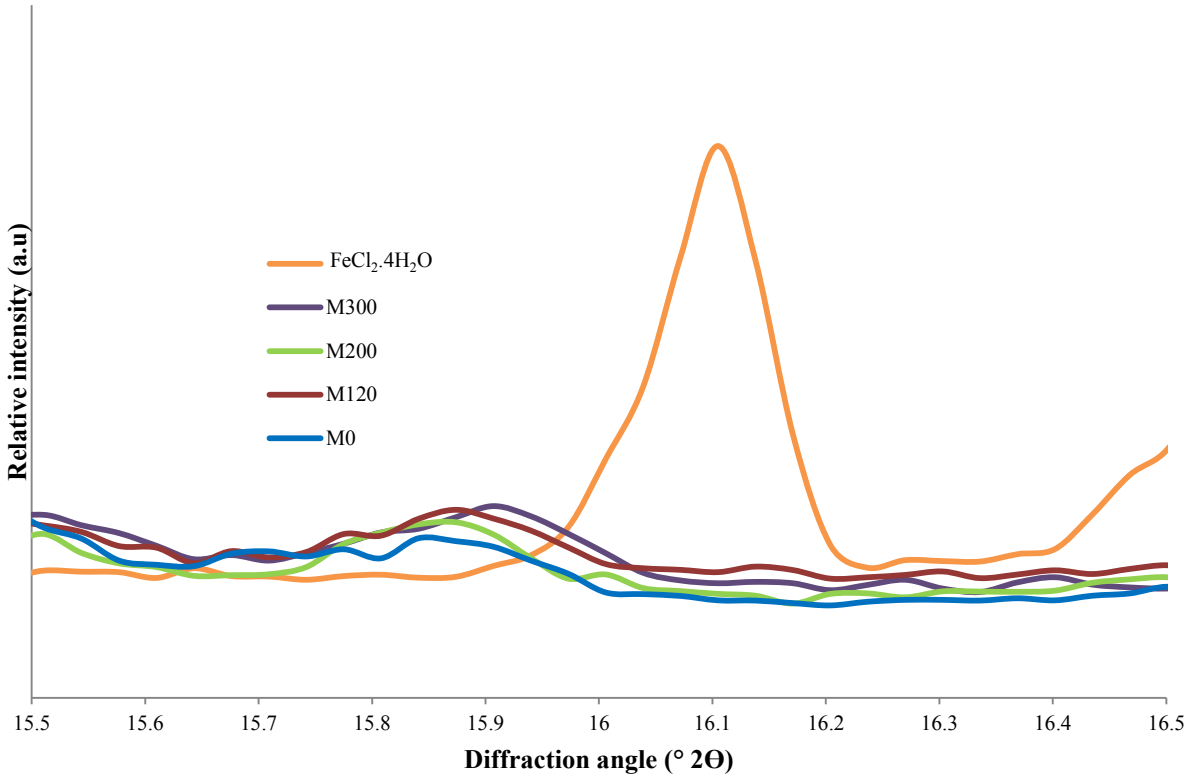

Figure 5.5 Section of powder XRD patterns for M0, M120, M200, M300, and $FeCl_2.4H_2O$

Upon heating the $FeCl_2.4H_2O$ to between 105 and 115 °C, it is dehydrated to the di-hydrate and, subsequently, to the monohydrate between 150 and 160 °C and, eventually, to the anhydride at 220 °C (Kirk and Othmer, 1984). In Figure 5.4 the powder spectra are presented for $FeCl_2.4H_2O$ as received, calcined at 120, 200 and 300 °C in the absence of air for 6 hours. Strong reflections at 38.4 ° 2θ are observed for the ambient temperature, 120 and 200 °C $FeCl_2$ samples. A second relatively strong reflection at 44.6 ° 2θ for the $FeCl_2.4H_2O$ at room temperature reduces intensity as the temperature increases to 200 °C. Both these reflections disappear on heating to 300 °C. A relative weak reflection around 16 ° 2θ in the original $FeCl_2.4H_2O$ sample increases intensity as it is heated to 300 °C. Noticeably, this peak is not visible in the spectra of the M300 sample in Figure 5.5.

In Figure 5.6 the powder XRD spectra are presented for samples Fe-ZSM-5/500, Low Fe-ZSM-5, High Fe-ZSM-5 and Z500. If recorded under identical conditions and instrument settings, relative peak intensities reflect relative quantities (provided there is no X-ray amorphous material present). The most intensive reflections for (1 0 4) and (1 1 0) planes at

33.1 ° and 35.6 ° of the X-ray powder diffraction pattern of α-Fe_2O_3 aggregates larger than 3-5 nm particle size (Delahay *et al.*, 2005) are observed. The peak intensities are tabulated in Table 5.1. The intensities of the said reflections for the Mid Fe-ZSM-5 sample are low, at 110 and 153 counts, increasing for the High Fe-ZSM-5 sample (262 and 210 counts), the Low Fe-ZSM-5 (365 and 327 counts) and the Fe-ZSM-5/500 sample (649 and 523 counts). No correlation is observed between the intensities of the α-Fe_2O_3 iron oxide reflections and the activity. However, this may be due to an artificial effect, since the reflections are slightly more intense than the signals in the XRD spectrum of the base material, Z500.

Powder XRD patterns are displayed in Figure 5.7 for the Fe-ZSM-5/500 and Fe-ZSM-5/900 samples. The zeolite maintained its characteristic XRD pattern with no significant weakening of the reflections at all calcination temperatures. The reflections at 33.1 ° and 35.6 ° related to α-Fe_2O_3 are similar in both the samples indicating that the higher temperature had no significant influence on the iron state.

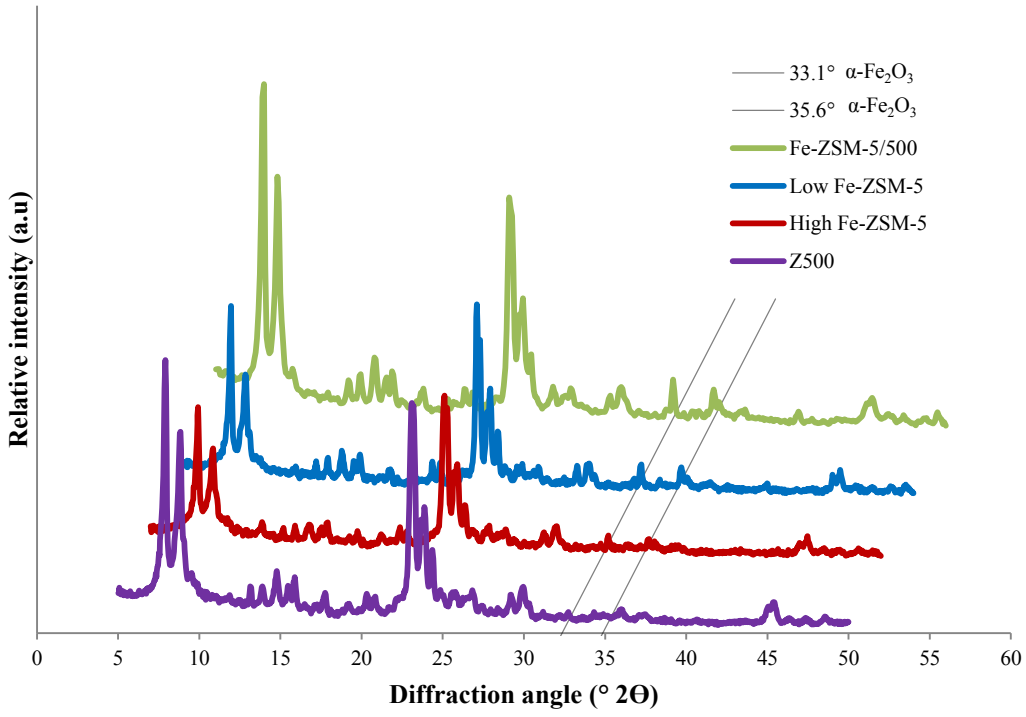

Figure 5.6 Powder XRD patterns for Fe-ZSM-5/500, Low Fe-ZSM-5, High Fe-ZSM-5 and Z500. α-Fe_2O_3 aggregates larger than 3-5 nm particle size peaks at 33.1° and 35.6° 2θ.

Table 5.1 Powder XRD intensities of α-Fe_2O_3 at 33.1 and 35.6 °

Sample	Calcination temperature °C	Activity N_2O conversion[a]	Peak count at 33.1°	Peak count at 35.6°
High Fe-ZSM-5	500	90 %	262	210
Mid Fe-ZSM-5	500	86 %	110	153
Low Fe-ZSM-5	500	71 %	365	327
Fe-ZSM-5/500	500	91 %	649	523
Fe-ZSM-5/550	550	87 %	615	613
Fe-ZSM-5/600	600	85 %	650	607
Fe-ZSM-5/650	650	78 %	651	601
Fe-ZSM-5/900	900	Not tested	653	534

a. 1 000 ppm N_2O, 100 ppm NO, 2.5 % O_2 and 3 100 ppm H_2O in nitrogen at 10 000 h^{-1} at 425 °C.

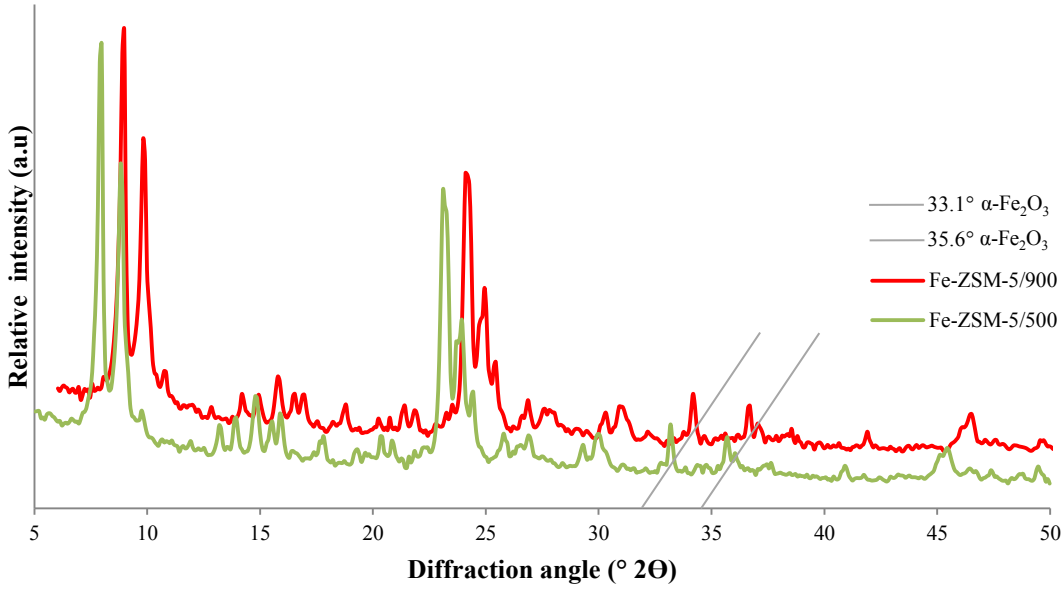

Figure 5.7 Powder XRD patterns for samples Fe-ZSM-5/500 and Fe-ZSM-5/900. α-Fe_2O_3 aggregates larger than 3-5 nm particle size peaks at 33.1° and 35.6° 2θ.

5.2. Porosity and surface area

Details of the procedure are described in section 4.2.2. Nitrogen adsorption/desorption isotherms recorded at liquid nitrogen temperature (-196 °C) are presented in Figure 5.8 and show type I (Web and Orr, 1997) characteristics with high microporosity – selected data are presented in Table 5.2. The milled and calcined materials, up to 200 °C calcination temperature, samples M0, M120 and M200, are virtually none porous. At 300 °C and above, samples M300, M400 and M500, porosity is observed and develops to almost the same extent as in the parent zeolite calcined at 500 °C (sample Z500).

In Figure 5.9 the pore volume distribution over pore sizes between 7 and 12 Å are presented for the parent zeolite Z500, samples M120, M300, M400 and M500. As Figure 5.8 and Table 5.2 indicate, the milled and calcined samples exhibit no microporosity for calcination temperatures of up to 200 ºC (samples M0, M120 and M200), while porosity shows for samples calcined at higher temperatures (M300, M400 and M500). Above of 300 °C pore sizes and pore volumes still shift to larger values with increasing calcination temperature, or as the catalyst progresses to its fully ion exchanged iron-zeolite state. Likewise, see Figure 5.8 and Table 5.2, the pore volume and pore size of the fully exchanged iron zeolite (M500) is only slightly lower than that of the parent zeolite (M500).

N_2 adsorption and desorption isotherms of plant produced and laboratory calcined extrudate samples Fe-ZSM-5/500 and Fe-ZSM-5/650 are depicted in Figure 5.10 which indicates that the porosity of the sample calcined at the higher temperature is significantly higher than that of the sample calcined at the lower temperature. Micropore volume (t-plot micropore volume) increased from 0.100 cm^3/g in the sample calcined at 500 °C to 0.116 cm^3/g with a significant increase in the pore volume around 9 Å (Figure 5.11) in the sample calcined at 650 °C but was still below that of M500, the corresponding powder sample (Table 5.2). The steepening-up at higher p/p_o of the N_2 adsorption and desorption isotherms of the extruded samples (Figure 5.10) compared to the powder samples (Figure 5.8) reflects the mesoporosity introduced by the binder.

The sample calcined at 650 °C displays a higher degree of hysteresis compared to the sample calcined at 500 °C indicating that mesoporosity increases with a further increase in calcination temperature. The mesopore volume increased from 0.147 to 0.169 cm^3/g by increasing calcination temperature from 500 to 650 ºC (see Table 5.2). It should be noted that

the mesoporosity is related to the shaping, as the comparison with the powder samples indicate (Table 5.2).

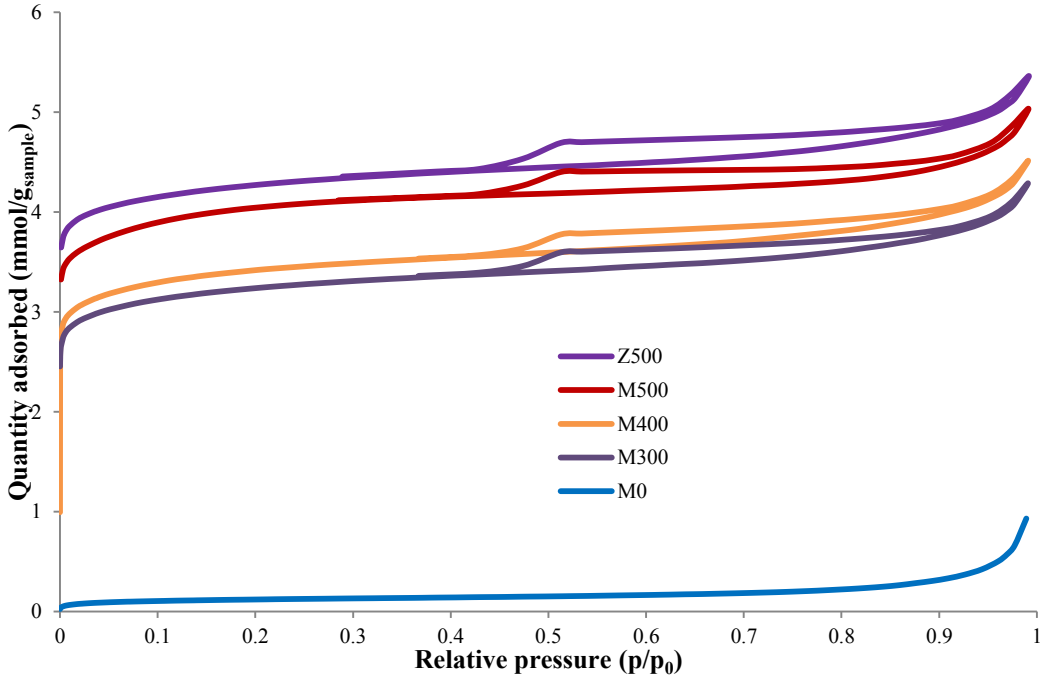

Figure 5.8 N_2 isotherms at recorded at liquid nitrogen temperature (-196 °C) of samples M0, M300, M400, M500 and Z500

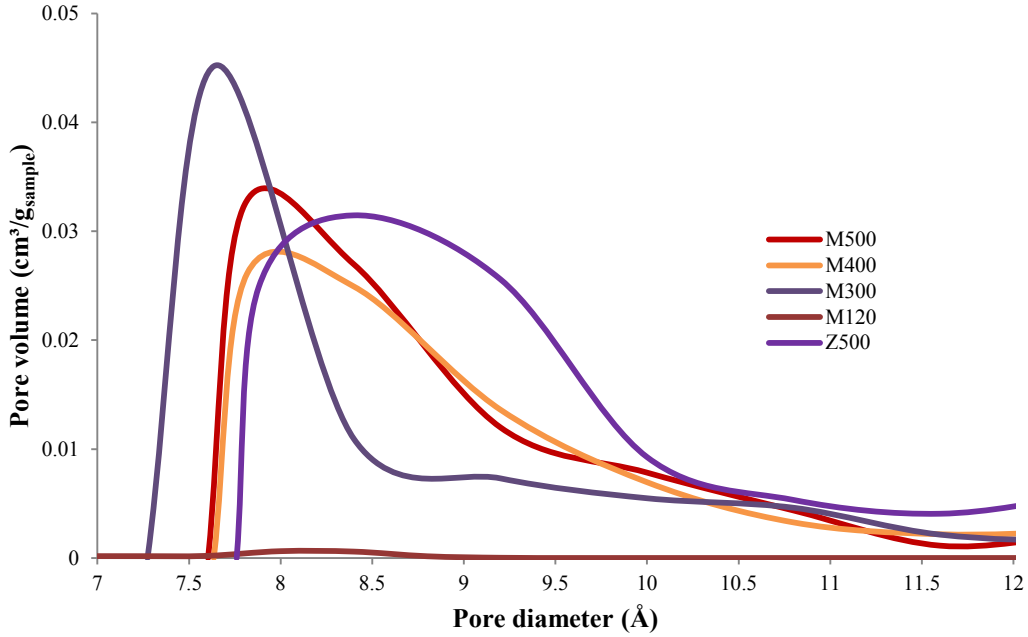

Figure 5.9 MP method plots of the supermicropore sizes and pore volumes for samples M120, M300, M400, M500 and Z500

Table 5.2 Nitrogen adsorption and desorption data

	Unit[a]	Z500	M120	M200	M 300	M400	M500	Fe-ZSM-5/500	Fe-ZSM-5/650	Low Fe-ZSM-5
BET surface area	m^2/g	297	9.3	9.5	227	239	283	259	302	307
t-Plot micropore surface area	m^2/g	264	3.8	4.4	195	206	252	200	231	241
BJH adsorption surface area	m^2/g	54.7	5.3	5.1	52.3	56.3	62.8	85.5	97.1	99.5
BJH desorption surface area	m^2/g	29.5	5.7	6.0	23.1	24.4	23.5	68.6	83.3	69.5
Dubinin-Radushkevich equivalent surface area	m^2/g	429	13.0	13.5	313	346	399	333	390	397
Dubinin-Astakhov equivalent surface area	m^2/g	502	10.7	10.6	374	373	461	412	462	498
Total pore volume	cm^3/g	0.186	0.032	0.034	0.149	0.157	0.175	0.233	0.282	0.262
t-Plot micropore volume	cm^3/g	0.133	0.002	0.002	0.098	0.103	0.126	0.100	0.116	0.121
BJH adsorption mesopore volume	cm^3/g	0.055	0.020	0.021	0.053	0.057	0.055	0.147	0.169	0.144
BJH desorption mesopore volume	cm^3/g	0.043	0.023	0.024	0.038	0.040	0.037	0.136	0.170	0.133
Dubinin-Radushkevich limiting micropore volume	cm^3/g	0.152	0.005	0.005	0.111	0.123	0.142	0.118	0.139	0.141
Dubinin-Astakhov limiting micropore volume	cm^3/g	0.158	0.006	0.005	0.119	0.129	0.149	0.129	0.151	0.153
MP method pore sizes between 7 and 12 Å	cm^3/g	0.063	0.002	0.002	0.045	0.046	0.048	0.048	0.054	0.058

a. Based on sample weight

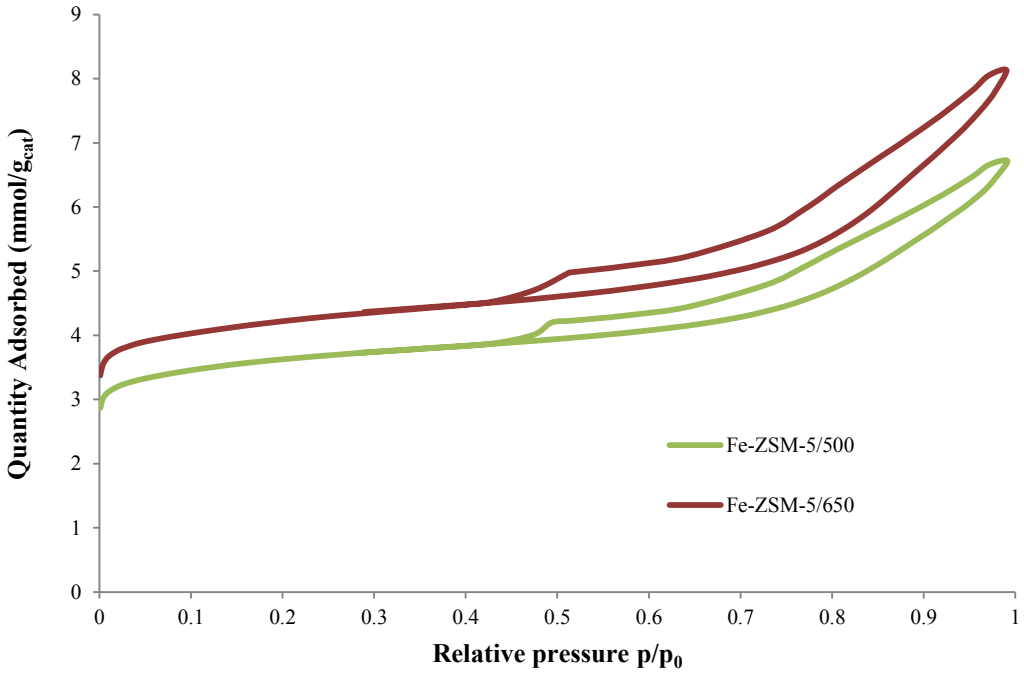

Figure 5.10 N_2 isotherms at recorded at liquid nitrogen temperature (-196 °C) of samples Fe-ZSM-5/500 and Fe-ZSM-5/650

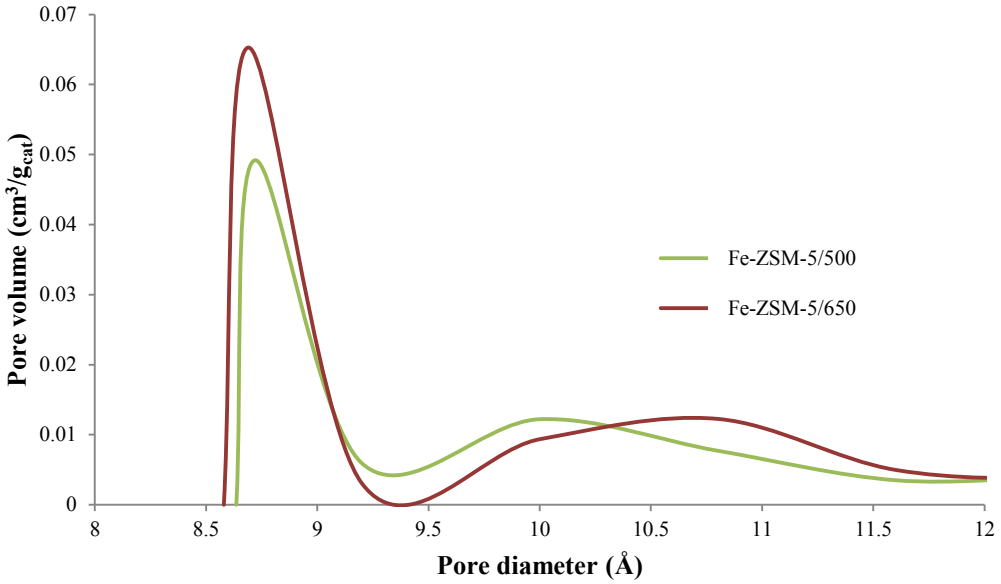

Figure 5.11 MP method plots of the of the supermicropore sizes and pore volumes for samples Fe-ZSM-5/500 and Fe-ZSM-5/650

The exponent of the Dubinin-Radushkevich equation is 2 and the optimised exponent of the Dubinin-Astakhov equation was 1, resulting in an improvement in the correlation factor from 0.9923 to 0.9997 respectively (see Appendix A-1.5 for the description of the method).

5.3. Differential thermogravimetric analysis (DTGA)

Details of the procedure are discussed in section 4.2.3. For the just milled NH_4-ZSM-5 + $FeCl_2.4H_2O$ mixed sample, M0, a weight loss of 9.87 % was recorded upon heating to 500 °C in nitrogen – this loss comprising of water, ammonium chloride and hydrogen chloride as 6.89, 2.39 and 0.59 %, respectively (Figure 5.12). The relatively high release of water compared to ammonium chloride is due to the residual moisture of approximately 5 % present in the SM27 substrate. Water contributed to the largest part of the weight loss with a major release at around 100 °C and a minor release between 300 and 340 °C. Ammonium chloride releases occurred at around 80, 195, 300 and 385 °C with the major peak at 300 °C. Hydrogen chloride showed a minor release between 150 and 300 °C and from 400 °C onwards a consistent release up to the end of the run.

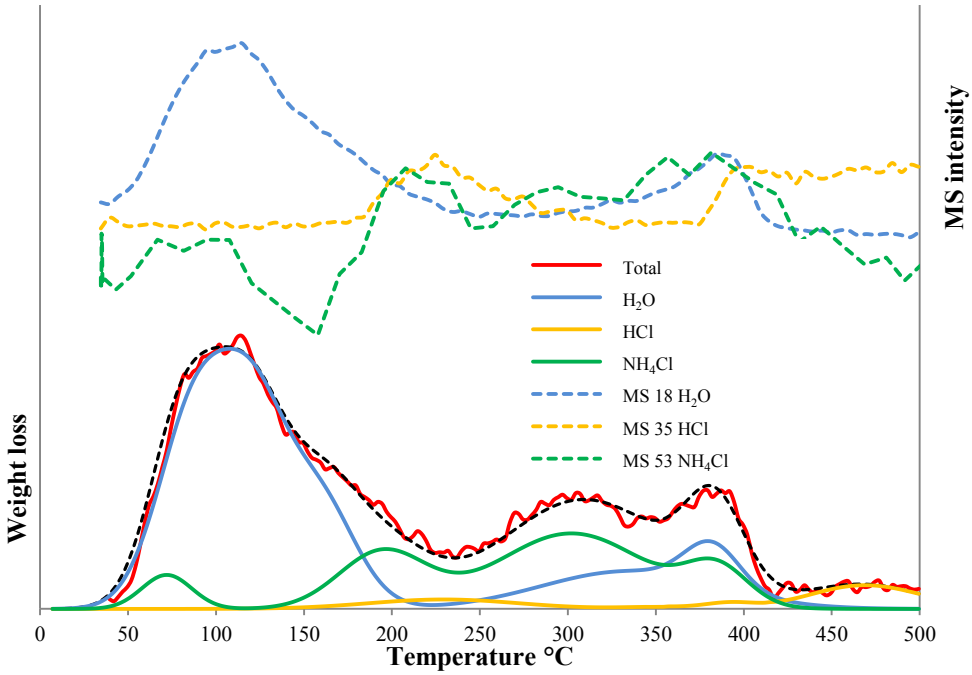

Figure 5.12 DTGA-MS of sample M0 (5 °C/min in nitrogen)

5.4. Ammonia temperature programmed desorption (TPD)

Details of the procedure are discussed in section 4.2.4. In Figure 5.13, a comparison of the ammonia TPD and the DTGA deconvolution traces of ammonium chloride are shown. No correlation is observed.

In Figure 5.14 ammonia temperature programmed desorption was performed on samples Z0 and plant produced and laboratory calcined extrudate samples Fe-ZSM-5/500 and Fe-ZSM-5/650 after calcination at 500 and 650 ºC in air for 5 hours which indicated that the acidity decreased up on higher calcination temperatures. Noticeable, the high temperature peak of the parent zeolite, Z0, decreases significantly after ion exchange of the Brønsted acid sites with iron in samples Fe-ZSM-5/500 and Fe-ZSM-5/650 which are in line with the observations of Brandenberger *et al*. (2009).

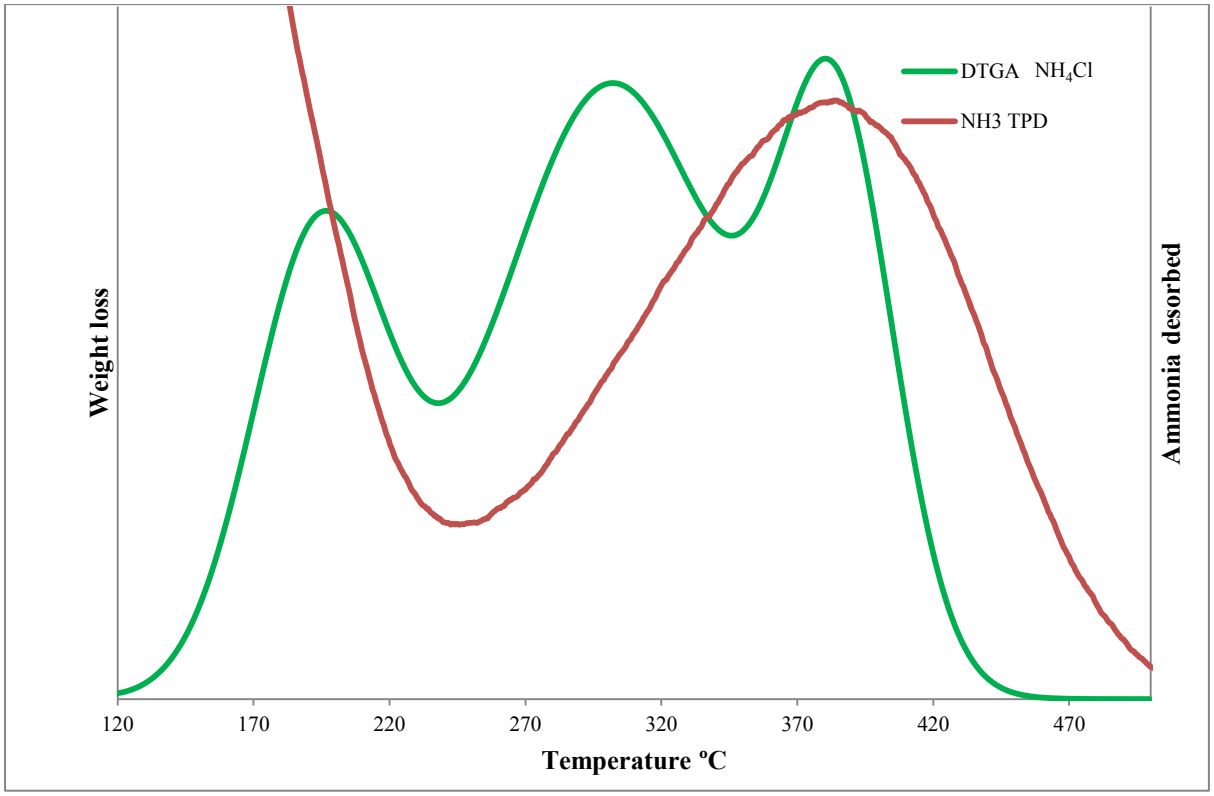

Figure 5.13 Section of ammonia TPD of Z0 (saturated with ammonia in helium, heated at 10 ºC/min to 700 ºC in 20 cm3/min helium at STP) and NH_4Cl DTGA of M0 (5 ºC/min in nitrogen)

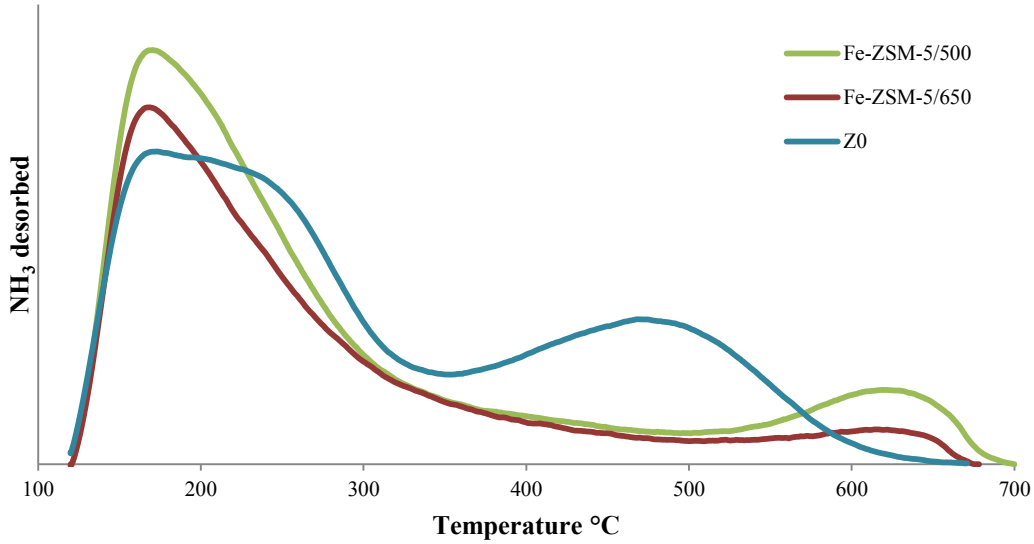

Figure 5.14 Ammonia TPD of samples Fe-ZSM-5/500, Fe-ZSM-5/650 and Z0 (saturated with ammonia in helium, heated at 10 ºC/min to 700 ºC in 20 cm^3/min helium at STP)

5.5. Temperature programmed N_2O conversion and α-oxygen concentration

Details of the procedure are discussed in section 4.2.5. Figure 5.15 and Figure 5.16 show N_2O conversion curves (traced by recording the combined N_2 + O_2 concentrations in the N_2O temperature programmed conversion effluent). In Table 5.3 the values derived from the curves are compiled for the iron content, α-oxygen concentration, activation energy, rate constant and temperatures required for 1, 50, 80 and 99 % N_2O conversion over the high temperature (≥ 500 °C) calcined samples.

Plant produced and laboratory calcined extrudate sample Fe-ZSM-5/500 shows a conversion curve at slightly lower temperatures than sample Fe-ZSM-5/650 (see Figure 5.15), whereas N_2O conversion starts and ends (at 1 and 99 % conversion respectively) at roughly the same temperatures for both catalysts. At medium temperature the Fe-ZSM-5/500 catalyst is more active by 5 - 14 °C (for 50 and 80 % N_2O conversion, respectively).

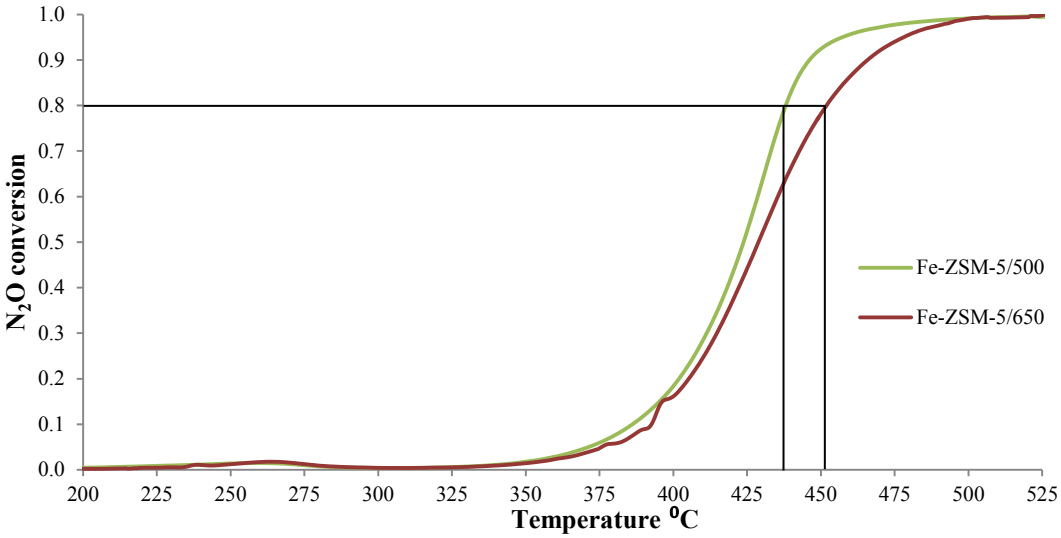

Figure 5.15 Temperature programmed N_2O conversion over samples Fe-ZSM-5/500 and Fe-ZSM-5/650 (TCD signal for N_2+O_2 concentration, N_2O 4.8 vol % in helium, 10 ºC/min, 0.3 g sample)

The curves for N_2O conversion over commercial extrudate samples High Fe-ZSM-5, Mid Fe-ZSM-5, Low Fe-ZSM-5, as well as samples Fe-ZSM-5/500 and Z0 are presented in Figure 5.16. The N_2O conversion activities as determined by tests method in section 4.2.9 (tested in the presence of NO and H_2O) compares reasonable well with the results as determined by temperature programmed N_2O conversion over the High Fe-ZSM-5, Mid Fe-ZSM-5 and Low Fe-ZSM-5 with plant produced samples in Figure 5.18 at 80 % conversion. Laboratory calcined extrudate sample Fe-ZSM-5/500 as an outlier indicating that the sample is behaving differently from the commercial catalysts (Figure 5.18).

For the commercial samples, High Fe-ZSM-5, Mid Fe-ZSM-5 and Low Fe-ZSM-5 N_2O conversion curves (see Figure 5.16), α-oxygen peaks were obtained in the low temperature range between 200 and 350 °C, but hardly so for laboratory specimen Fe-ZSM-5/500 and Fe-ZSM-5/650 (see Figure 5.15) or parent zeolite Z0 (Figure 5.16). The low temperature peak is ascribed to the conversion of N_2O to N_2 and adsorbed oxygen, the so called α-oxygen (see the description section 4.2.5). For samples Fe-ZSM-5/500 and Fe-ZSM-5/650 this signal is very weak (see Figure 5.15). The concentrations of α-oxygen were derived from the integral of the areas under the low temperature peaks (200 – 350 °C) in Figure 5.15 and Figure 5.16 are tabulated in Table 5.3.

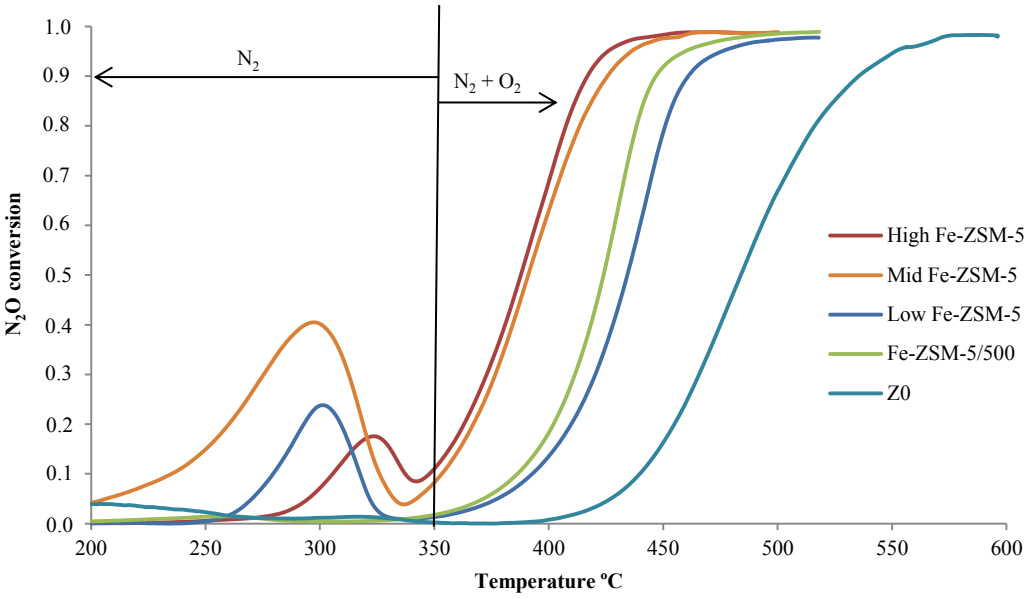

Figure 5.16 Temperature programmed N_2O conversion over samples High Fe-ZSM-5, Mid Fe-ZSM-5, Low Fe-ZSM-5, Fe-ZSM-5/500 and Z0 (TCD signal for N_2 below 350 °C and N_2+O_2 concentration above 350 °C, N_2O 4.8 vol % in helium, 10 °C/min, 0.3 g sample)

The apparent activation energies and pre-exponential factors (rate constants) determined by Arrhenius plots (Figure 5.17) are tabulated in Table 5.3. The apparent activation energies decrease from 181 to 156 kJ/mol for Low Fe-ZSM-5 and Mid Fe-ZSM-5 to the high activity sample High Fe-ZSM-5. However, no consistent relationship is observed with regards to the rate constants. The activation energies for N_2O conversion over laboratory specimen Fe-ZSM-5/500 and Fe-ZSM-5/650 are higher at 197 kJ/mol, but the rate constants are also rather high compared to the commercial samples High Fe-ZSM-5, Mid Fe-ZSM-5, Low Fe-ZSM-5.

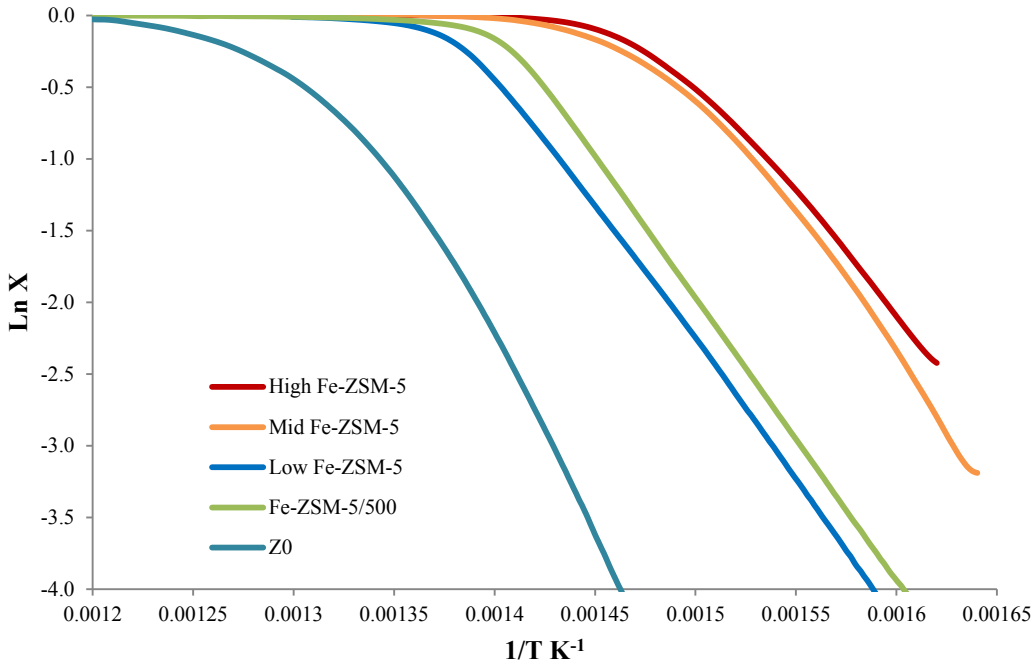

Figure 5.17 Arrhenius plots for N_2O conversion over samples High Fe-ZSM-5, Mid Fe-ZSM-5, Low Fe-ZSM-5, Fe-ZSM-5/500 and Z0 (N_2O 4.8 vol % in helium, 10 ºC/min, 0.3 g sample)

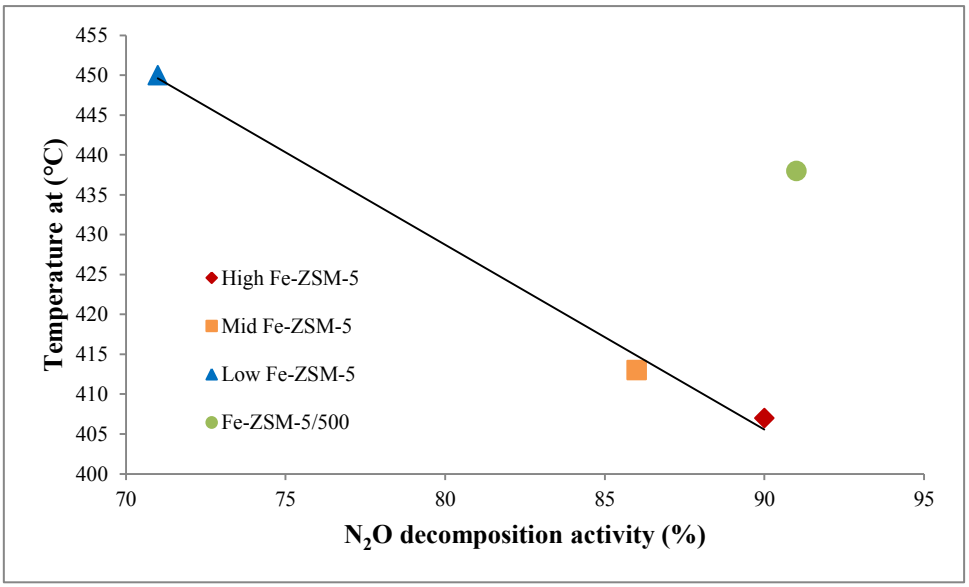

Figure 5.18 Catalytic activity N_2O conversion performance test results (1 000 ppm N_2O, 100 ppm NO, 2.5 % O_2 and 3 100 ppm H_2O in nitrogen at 10 000 h-1) vs the temperature at 80 % conversion during temperature programmed N_2O conversion (N_2O 4.8 vol % in helium, 10 ºC/min, 0.3 g sample).

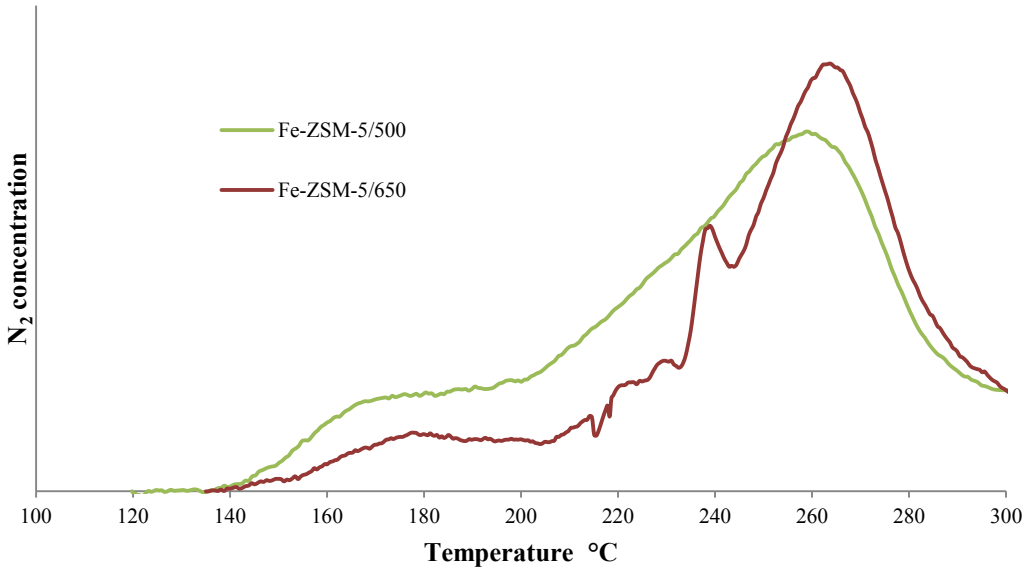

Figure 5.19 α-oxygen concentrations for Fe-ZSM-5/500 and Fe-ZSM-5/650 (TCD signal for N_2 concentration, N_2O 4.8 vol % in helium, 10 ºC/min, 0.3 g sample)

The apparent activation energies for N_2O conversion over all the samples (Table 5.3) investigated in the study ranges between 156 and 197 kJ/mol, which values are in line with the values published by Kiwi-Minsker *et al.* (2003): 169 kJ/mol, Kondratenko and Pérez-Ramírez (2007): 161 kJ/mol and Pirngruber *et al.*, (2004): 120 - 190 kJ/mol.

Table 5.3 α-Oxygen concentrations and N_2O conversion temperatures

Sample	Fe content wt %[a]	α-Oxygen content mmol/g[b]	α /Fe mol/mol	α-Oxygen peak temperature °C[b]	Activation energy KJ/mol[d]	Rate constant s^{-1} [d]	N_2O Conversion temperature °C[c] 1%	50%	80%	99%
Z0	0.02[e]	0.009	0.438	318	217	16×10^{11}	403	483	515	571
High Fe-ZSM-5	3.45	0.164	0.244	323	156	0.1×10^{11}		387	407	442
Mid Fe-ZSM-5	3.42	0.699	1	292	175	1.5×10^{11}		391	413	449
Low Fe-ZSM-5	3.42	0.298	0.487	301	181	0.9×10^{11}	339	434	450	497
Fe-ZSM-5/500	3.41	0.034	0.056	260	197	8.8×10^{11}	338	424	438	496
Fe-ZSM-5/650	3.41	0.017	0.028	263	197	7.9×10^{11}	341	429	452	500

a. Determined by ICP-AES, weight percentage Fe in sample

b. Determined from N_2O conversion (N_2O 4.8 vol % in helium, 10 ºC/min) in the temperature range between 200 and 350 °C.

c. Determined from N_2O conversion (N_2O 4.8 vol % in helium, 10 ºC/min)

d. Determined from N_2O conversion Arrhenius plots (N_2O 4.8 vol % in helium, 10 ºC/min) assuming first order reaction (Pirngruber *et al.*, 2004)

e. Commercial SM27 substrate contains 0.02 % Fe

5.6. Temperature programmed reduction (TPR)

Details of the procedure are discussed in section 4.2.6. Ammonia temperature programmed reduction (TPR) was carried out right after the end of the N_2O conversion experiment with each catalyst. Traces for plant produced and laboratory calcined extrudate samples Fe-ZSM-5/500 and Fe-ZSM-5/650 are presented in Figure 5.20. The sample calcined at 500 °C consumed considerably less reducing agent below 500 °C and, conversely, significantly more above 500 °C than the sample calcined at 650 °C. Above 600 °C ammonia is catalytically decomposed into nitrogen and hydrogen on metallic iron.

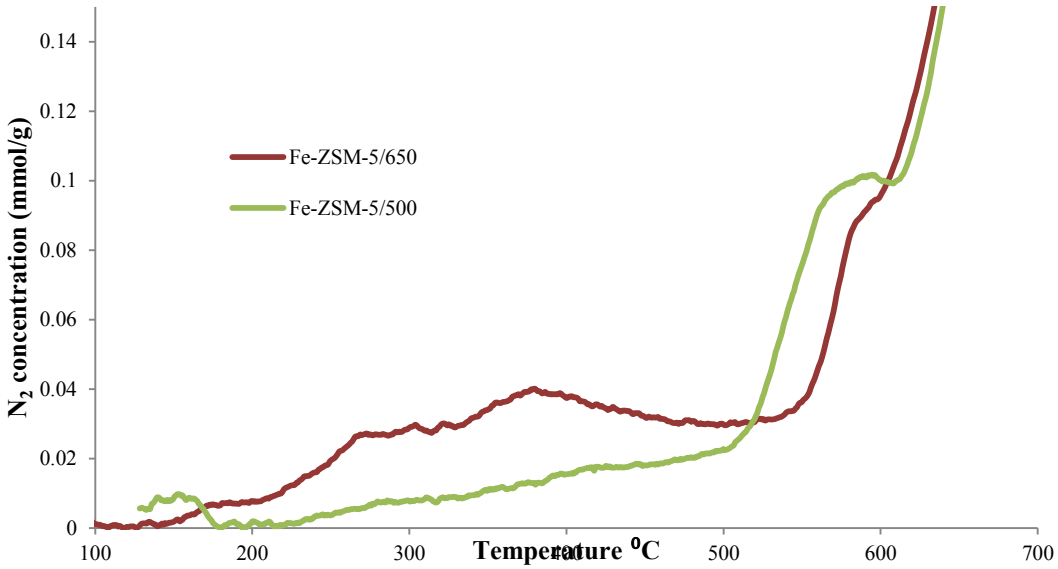

Figure 5.20 Ammonia TPR of samples Fe-ZSM-5/500 and Fe-ZSM-5/650

5.7. Diffuse reflectance UV/visible spectroscopy

Details of the procedure are discussed in section 4.2.7. The diffuse reflectance UV/visible spectra recorded for plant produced and laboratory calcined extrudate samples Fe-ZSM-5/500 and Fe-ZSM-5/650 are depicted in Figure 5.21. No differences are observed between the two spectra indicating that the different calcination temperatures (500 and 650 ºC) had no effect on the iron oxides that were formed. In Figure 5.22 the diffuse reflectance UV/visible spectra are presented, recorded for samples Fe-ZSM-5/500, Low Fe-ZSM-5, Mid Fe-ZSM-5 and High Fe-ZSM-5.

In Table 5.4 the relative band intensities are tabulated after spectrum deconvolution. In both, Figure 5.22 and Table 5.4, the wave length ranges are assigned to certain iron species. High Fe-ZSM-5 and Mid Fe-ZSM-5 samples contain a relatively high proportion of isolated Fe^{3+} species respectively (the bands below 300 nm) compared to Fe-ZSM-5/500 and Low Fe-ZSM-5, while the latter contains considerably higher proportions of small oligonuclear ferric clusters located in the zeolite channels (the bands between 300 and 400 nm). The broad overlapping bands and unknown excitation coefficients make quantification imprecise (Brandenberger *et al.*, 2010b).

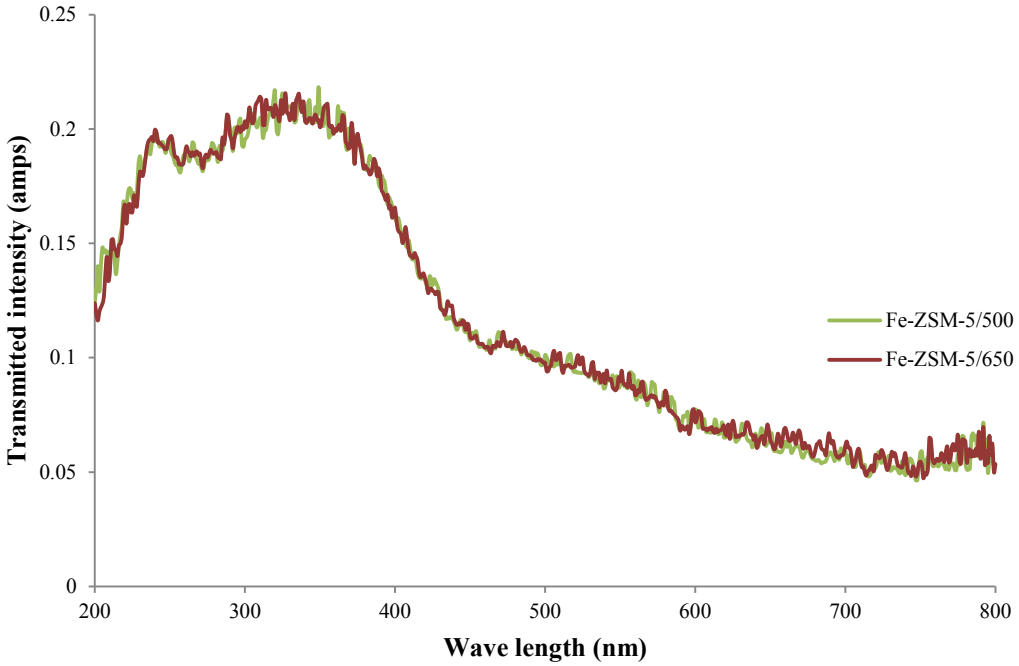

Figure 5.21 Diffuse Reflectance UV/visible spectra for samples Fe-ZSM-5/500 and Fe-ZSM-5/650

Table 5.4 Relative Diffused Reflectance UV/visible spectrum band intensities

Iron state	Wave length nm	High Fe-ZSM-5	Mid Fe-ZSM-5	Low Fe-ZSM-5	Fe-ZSM-5/500	Fe-ZSM-5/650
Fe^{3+} isolated species	200 – 300	36 %	37 %	23 %	22 %	22 %
Oligomeric Fe_xO_y in zeolite channel	300 – 400	25 %	28 %	38 %	35 %	35 %
Fe_2O_3 cluster on external surface	400 – 600	20 %	19 %	23 %	20 %	20 %
Fe^{3+} oxides and hydroxides	600 – 800	19 %	16 %	16 %	23 %	23 %

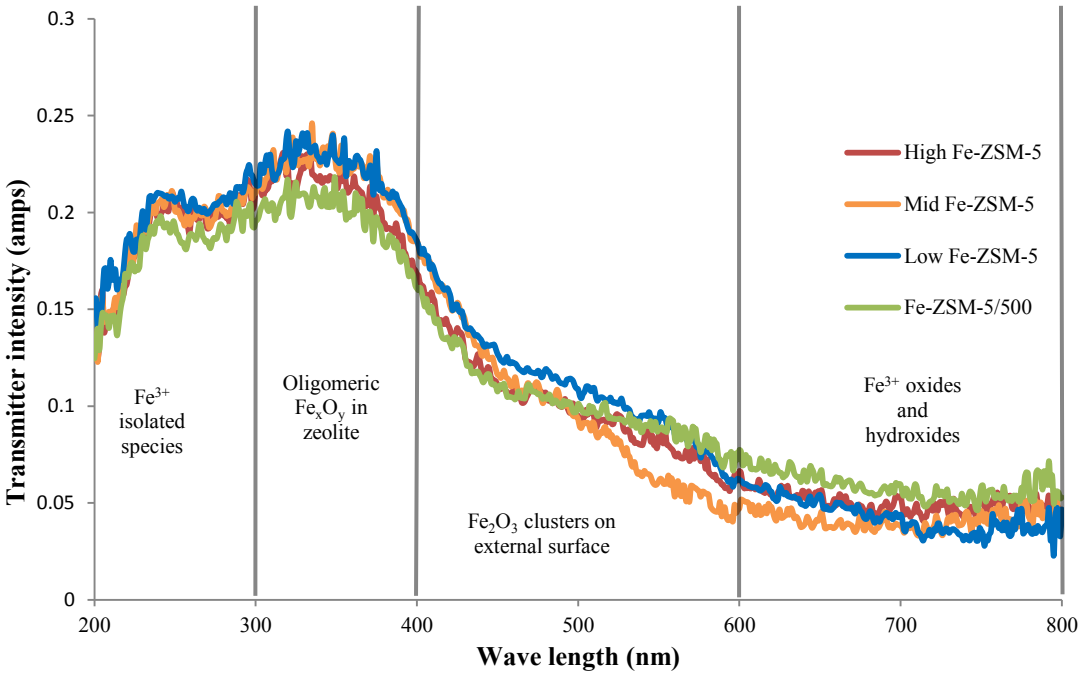

Figure 5.22 Diffuse Reflectance UV/visible spectra for samples Fe-ZSM-5/500, Low Fe-ZSM-5, Mid Fe-ZSM-5 and High Fe-ZSM-5. See section 4.2.7 for assignments.

5.8. Mössbauer spectroscopy

Details of the procedure are discussed in section 4.2.8. Figure 5.23 presents Mössbauer spectra recorded at room temperature in air. The Mössbauer parameters are tabulated in Table 5.5 for the High Fe-ZSM-5, Mid Fe-ZSM-5, Low ZSM-5, Fe-ZSM-5/500 and Fe-ZSM-5/650 samples. The Mössbauer spectra of samples Mid Fe-ZSM-5 and High Fe-ZSM-5 display relatively high proportions of doublets, whereas samples Low Fe-ZSM-5, Fe-ZSM-5/500 and Fe-ZSM-5/650 display relatively high proportions of sextets. Sample Fe-ZSM-5/650 displays two sextets whereas sample Fe-ZSM-5/500 only displays a single one.

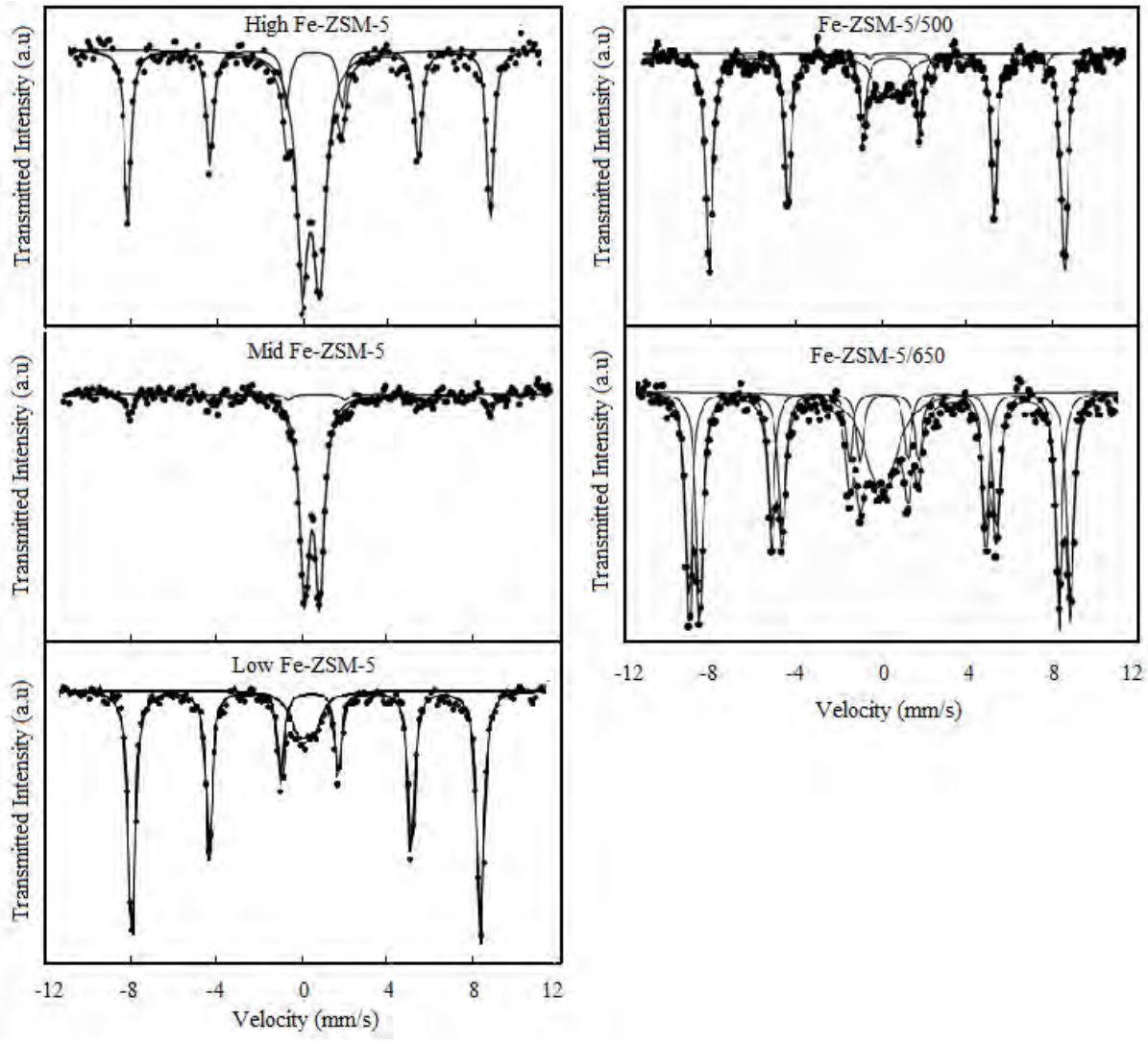

Figure 5.23 Mössbauer spectra, recorded at room temperature in air of, High Fe-ZSM-5, Mid Fe-ZSM-5, Low Fe-ZSM-5, Fe-ZSM-5/500 and Fe-ZSM-5/650 with curves derived from deconvolution.

Table 5.5 Mössbauer spectra parameters

Sample		IS[a] (mm/s)	QS_{Doub}[b] (mm/s)	H[c] (T)	*f* (%)
High Fe-ZSM-5	Doublet	0.35	0.83		53.9
	sextet A	0.37		51.6	46.1
Mid Fe-ZSM-5	Doublet	0.37	0.70		82.9
	sextet A	0.43		51.5	17.1
Low Fe-ZSM-5	Doublet	0.25	0.59		14.8
	sextet A	0.36		50.2	85.2
Fe-ZSM-5/500	Doublet	0.41	0.96		15.9
	sextet A	0.37		51.4	84.1
Fe-ZSM-5/650	Doublet	0.37	0.61		41.7
	sextet A	0.64		53.6	37.4
	sextet B	0.13		53.6	20.9

6.1. See Appendix A-3.1
6.2. See Appendix A-3.2
6.3. See Appendix A-3.3

5.9. Catalyst activity

Details of the procedure are discussed in section 4.2.9. The catalytic activities at 425 °C (1 000 ppm N_2O, 100 ppm NO, 2.5 % O_2 and 3 100 ppm H_2O in nitrogen at 10 000 h^{-1}) of all the Fe-ZSM-5 plant produced and laboratory calcined extrudate between 500 and 650 °C are tabulated in Table 5.1 and presented in Figure 5.24. The activity decreases steadily as the calcination temperature increased.

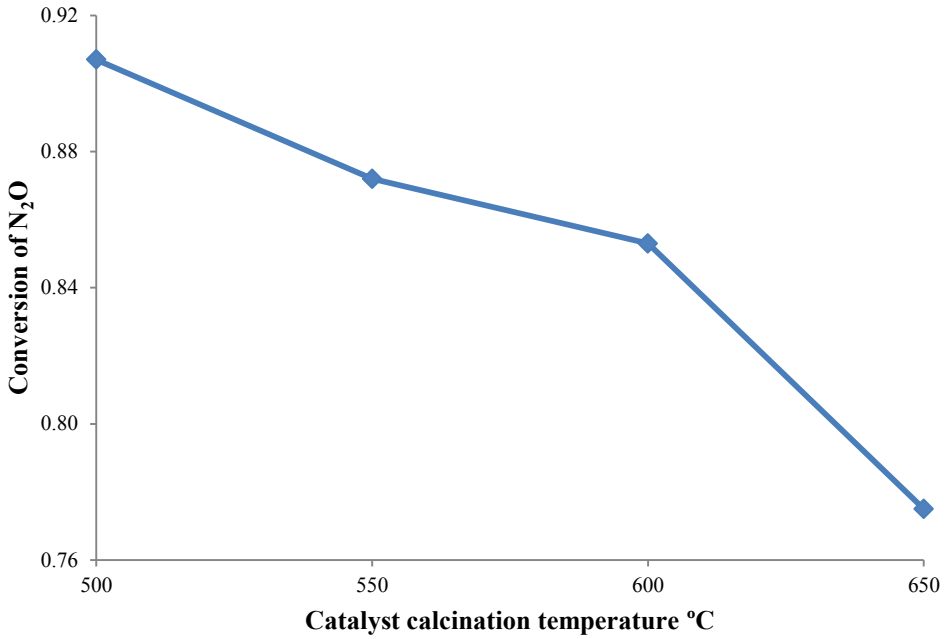

Figure 5.24 N_2O selective catalytic conversion at 425°C over catalyst Fe-ZSM5/500, Fe-ZSM5/550, Fe-ZSM5/600 and Fe-ZSM5/650, as a function of final catalyst calcination temperature. (1 000 ppm N_2O, 100 ppm NO, 2.5 % O_2 and 3 100 ppm H_2O in nitrogen at 10 000 h^{-1} at 425 °C)

6. Discussion

6.1. Characterisation of the solid-state ion exchange

After milling the zeolite and ferrous chloride combination (M0), no reflections characteristic of ferrous chloride are detected via powder XRD analysis (Figure 5.1). This is ascribed to the substantial amount of mechanical energy which is transferred to the ferrous salt and consequently, leads to the destruction of the crystal and the formation of an X-ray amorphous ferrous chloride phase. Nitrogen adsorption findings (Figure 5.8 and Table 5.2) suggest that the ferrous chloride is condensed in the zeolite mesopores and plugs micropore mouths, resulting in a pseudo non-porous material.

XRD diffractogram of $FeCl_2.4H_2O$ as received and heated to 120, 200 and 300 °C (Figure 5.4) indicates that the reflections characteristic of $FeCl_2.4H_2O$ at 38 ° and 45 ° 2θ decreases in intensity and completely disappears at 300 °C. A reflection at 16 ° 2θ increase from a relatively weak reflection in $FeCl_2.4H_2O$ at ambient temperature to strong reflection after heating to 300 °C. These observations are consistent with the fact that upon heating the $FeCl_2.4H_2O$ to between 105 and 115 °C, it is dehydrated to the di-hydrate and, subsequently, to the monohydrate between 150 and 160 °C and, eventually, to the anhydride at 220 °C (Kirk and Othmer, 1984).

After heating of the M0 sample to 120 °C, sample M120 exhibits two strong reflections at 38 ° and 45 ° 2θ (Figure 5.1), characteristic of iron(II) chloride – likely, the ferrous chloride dissolves completely in its crystal water and residual moisture from the SM27 which contains approximately 5 % moisture (ferrous chloride has a solubility of 94.9 g $FeCl_2$/100g H_2O at 100 °C with a melting point of 105 °C (Patnaik, 2002)), diffuses into the zeolite micropores and with the cooling of the samples to room temperature (samples M120 and M200) resulting in the crystallisation of ferrous chloride and pore mouth blockage until the temperature exceeds 200 °C (Figure 5.8 and Table 5.2). The ferrous chloride reflections (Figure 5.1) disappear completely after heating the sample to 300 °C (sample M300).

The intensity of the (0 2 0) and (2 0 0) reflections of the zeolite in the XRD diffractogram (Figure 5.3) are sensitive to filling of the zeolite channels (Kharitonov *et al*., 1995). Initially,

after milling the zeolite with the ferrous chloride (sample M0), the intensity of the reflections is relatively strong but decreases by about 30% upon heating the sample to 120 °C (sample M120). The reduction in intensity is due to the pore filling that occurs when the ferrous chloride tetrahydrate liquefies (see previous paragraph) and diffuses into the micropores. By increasing the temperature to 120 °C, material is driven off mostly in the form of moisture, ammonium chloride and a trace of hydrogen chloride (Figure 5.12), resulting in recovery of porosity (Figure 5.8and Figure 5.9) and a concomitant increase in the intensity of the (0 2 0) and (2 0 0) lines (Figure 5.3).

Some desorption of ammonium chloride is detected during the TGA at approximately 180 °C (Figure 5.12) consistent with the ammonium chloride sublimation temperature of approximately 180 °C (Kirk and Othmer, 1984), but most of it desorbs at higher temperature (250 – 400 °C), see Figure 5.12. The reflection at 16 ° 2θ characteristic of anhydrous $FeCl_2$ (Figure 5.4) is not visible in the M300 sample calcined at 300 °C (Figure 5.5) whereas the reflection at 45 ° 2θ characteristic of hydrated $FeCl_2$ (see paragraph 2 on page 60) is still visible at 200 °C (Figure 2.1) which is an indication that the ion exchange process of $FeCl_2$ with the zeolite has occurred between 200 and 300 °C. In an ion exchange reaction, ammonium desorbs and ferrous chloride adsorbs simultaneously and directly at the two neighbouring oxygen atoms of the aluminium ion in the zeolite structure, a chloride ion separate from the bonded ferrous chloride reacting with ammonium ion forming ammonium chloride, as depicted in Figure 6.1, which diffuses out of the zeolite pores into the TGA carrier gas resulting in an increase in the zeolite micropore volume (Figure 5.9 and Table 5.2) and an increase in the intensity of the (020) and (200) X-ray reflections (Figure 5.3).

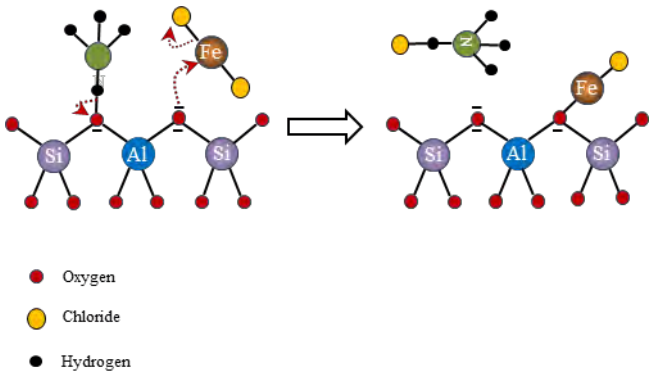

Figure 6.1 Ion exchange mechanism

Lázár *et al*. (1995) reported evidence of solid-state ion exchange, namely, a decrease in the intensity of the XRD reflections of iron(II) chloride and the appearance of reflections typical of crystalline ammonium chloride in the diffractogram of the ground mixture. On the other hand, Abu-Zied *et al*. (2008) found that, the ion exchange between the NH_4^+ ions of the zeolite and the metal cations of the salt takes place during thermal treatment of the milled material (up to 550 °C). During the thermal treatment, the ion exchange reaction is accompanied by evolution of HCl or NH_4Cl gases depending on the form of the zeolite used, namely H- or NH_4-zeolite. As can be seen from powder XRD measurements in this study (Figure 5.1), no ammonium chloride reflections are visible at any stage of the solid-state ion exchange process. However, NH_4Cl is detected during thermogravimetric analysis between 150 and 420 ºC (Figure 5.12). Hence, it may be concluded from this study that the process of solid-state ion exchange occurs as observed by Abu-Zied *et al*. (2008). From the respective results of this study it can be concluded further that it is a simultaneous process of direct ion exchange of NH_4^+ and Fe^{2+}.

6.2. The nature of the iron species and effect on catalytic activity

Fe_2O_3 oxides are widely accepted as being catalytically inactive in reactions with nitrous oxide (Schwidder *et al.*, 2004; Marturano *et al.*, 2000). The catalytic activity in most instances is inversely related to the free iron oxide content of the catalyst, that is, when the content of free iron oxide is low, the activity is high. Li *et al*. (2008) reported that Fe_2O_3 nanoparticles in Fe-zeolite catalysts played an even negative role since they block the channels of the zeolites and reduce the accessibility of the catalytically active isolated/oligonuclear iron species in the channels. Reflections from planes (1 0 4) and (1 1 0) at 33º and 36º 2θ, characteristic of α-Fe_2O_3, have been observed during powder XRD of the catalysts samples (Figure 5.6). Intensities and activities for N_2O conversion of the respective samples are given in Table 5.1. Both are plotted vs. each other are plotted in Figure 6.2 which shows that, regardless if the Low Fe-ZSM-5 sample (71 % conversion) is considered or not, there is no correlation between the content of free iron oxides (α-Fe_2O_3) and catalytic activity. There is also no correlation between the group of plant produced and laboratory calcined extrudate samples Fe-ZSM5/500, Fe-ZSM-5/550, Fe-ZSM-5/600 and Fe-ZSM-5/650, whose content in free iron oxides hardly varies with calcination temperature, while activity does.

This is not a surprise, since activity is related to the, X-ray amorphous content of isolated/oligonuclear iron species not the free iron oxides.

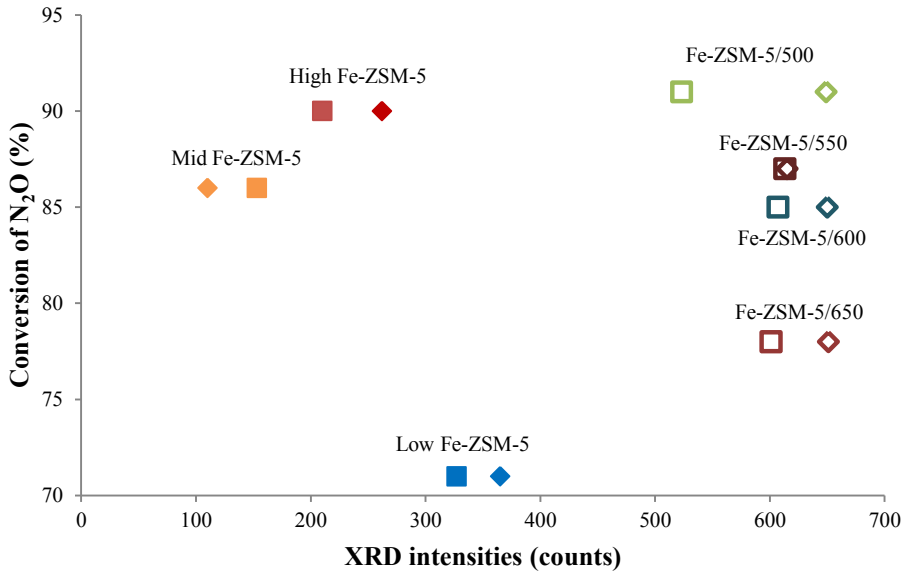

Figure 6.2 Conversion of N_2O (1 000 ppm N_2O, 100 ppm NO, 2.5 % O_2 and 3 100 ppm H_2O in nitrogen at 10 000 h^{-1} at 425 °C) over ion exchanged samples High Fe-ZSM-5, MiD Fe-ZSM-5 and Low Fe-ZSM-5 (full symbols) and Fe-ZSM-5/500, Fe-ZSM-5/550, Fe-ZSM-5/600 and Fe-ZSM-5/650 (open symbols) vs the respective XRD intensities of α-Fe_2O_3 at 33.1° and 35.6° (diamonds and squares, respectively).

Of the samples that were finally calcined at 500 °C, plant produced and laboratory calcined extrudate specimen Fe-ZSM-5/500 has a somewhat lower area between 200 and 300 nm in the UV/visible spectrum, characteristic of isolated Fe^{3+} species in the extra-framework positions, compared to the commercial Fe-ZSM-5 samples (Figure 5.22 and Table 5.4). On the other hand, it has comparable concentrations of octahedral ferric species in small oligonuclear clusters, which are characterized by strong absorptions between 300 and 400 nm, with the Low Fe-ZSM-5. It also has the highest band intensity above 600 nm which are ascribed to α-Fe_2O_3 of all the samples.

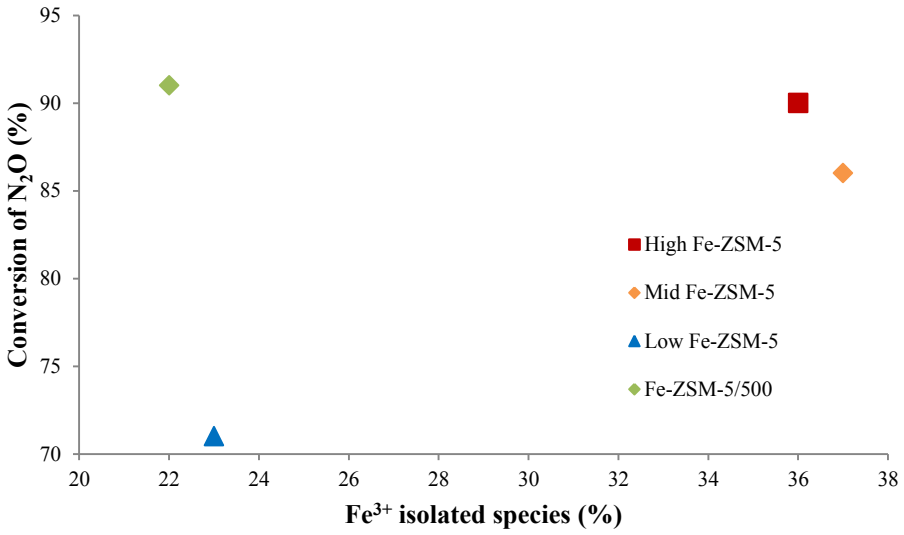

Figure 6.3 Conversion of N_2O (1 000 ppm N_2O, 100 ppm NO, 2.5 % O_2 and 3 100 ppm H_2O in nitrogen at 10 000 h^{-1} at 450 °C) over ion exchanged samples High Fe-ZSM-5, MiD Fe-ZSM-5, Low Fe-ZSM-5 and Fe-ZSM-5/500 vs the percentage Fe^{3+} isolated species (wave lengths between 200 and 300 nm).

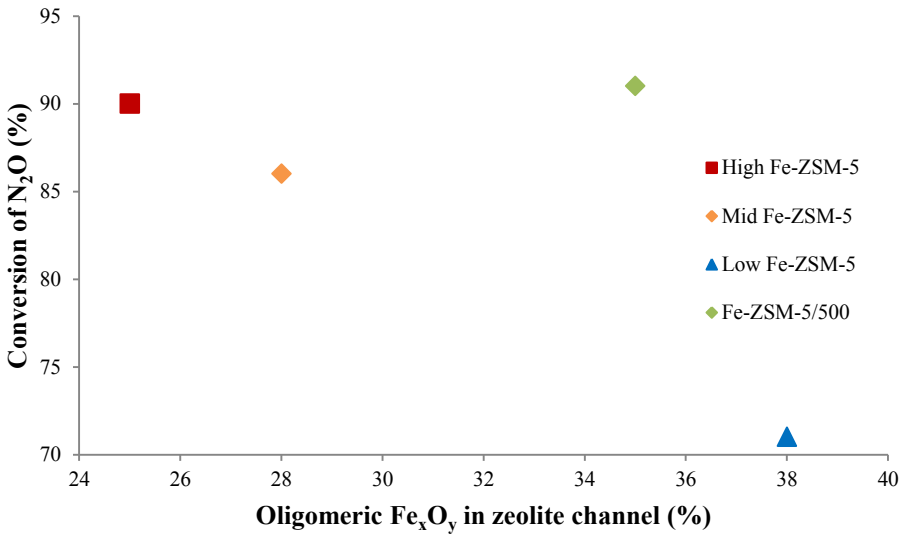

Figure 6.4 Conversion of N_2O (1 000 ppm N_2O, 100 ppm NO, 2.5 % O_2 and 3 100 ppm H_2O in nitrogen at 10 000 h^{-1} at 425 °C) over ion exchanged samples High Fe-ZSM-5, MiD Fe-ZSM-5, Low Fe-ZSM-5 and Fe-ZSM-5/500 vs the percentage Oligomeric Fe_xO_y in zeolite channel (wave lengths between 300 and 400 nm).

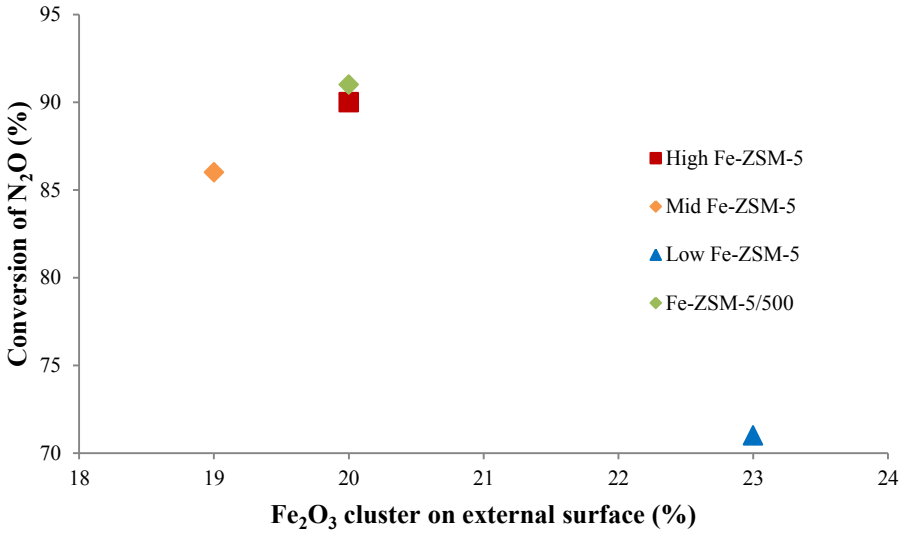

Figure 6.5 Conversion of N_2O (1 000 ppm N_2O, 100 ppm NO, 2.5 % O_2 and 3 100 ppm H_2O in nitrogen at 10 000 h^{-1} at 425 °C) over ion exchanged samples High Fe-ZSM-5, MiD Fe-ZSM-5, Low Fe-ZSM-5 and Fe-ZSM-5/500 vs the percentage Fe_2O_3 cluster on external surface (wave lengths between 400 and 600 nm).

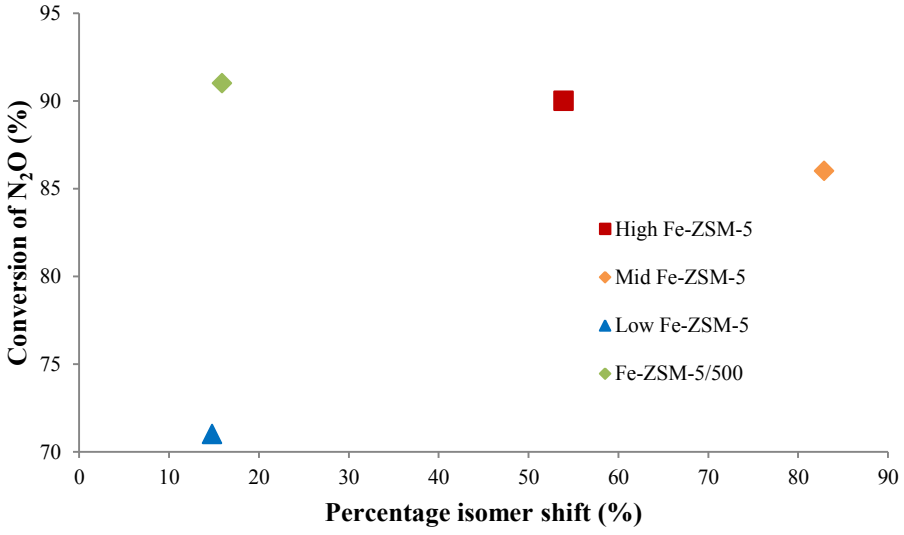

Figure 6.6 Conversion of N_2O (1 000 ppm N_2O, 100 ppm NO, 2.5 % O_2 and 3 100 ppm H_2O in nitrogen at 10 000 h^{-1} at 450 °C) over ion exchanged samples High Fe-ZSM-5, MiD Fe-ZSM-5, Low Fe-ZSM-5 and Fe-ZSM-5/500 vs the percentage Mössbauer isomer shift.

From Mössbauer spectroscopy it is observed that significant magnetic hyperfine field sextets are present in all Fe-ZSM-5 samples except sample Mid Fe-ZSM-5. Moreover, in Figure 6.7 Fe-ZSM-5/500 and Low Fe-ZSM-5 samples contain roughly the same percentage magnetic hyperfine field sextet in the Mössbauer spectra (Table 5.5 and Figure 5.23).

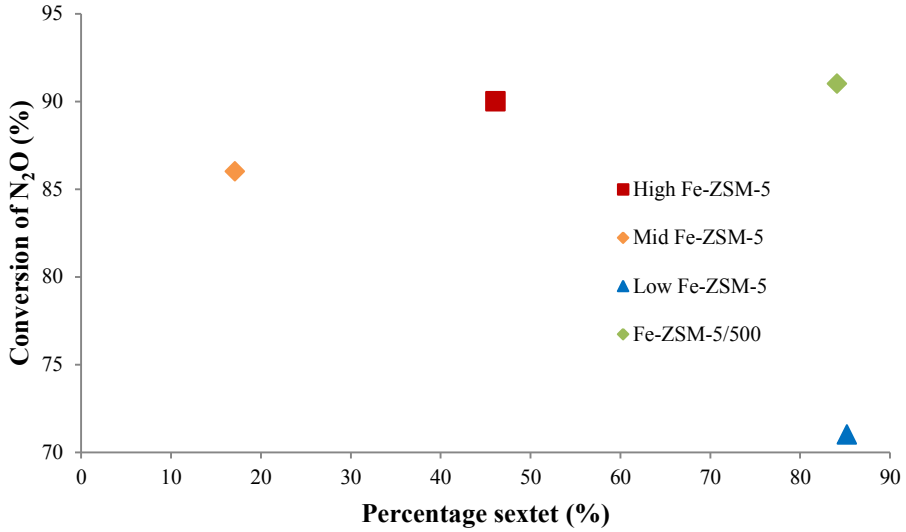

Figure 6.7 Conversion of N_2O (1 000 ppm N_2O, 100 ppm NO, 2.5 % O_2 and 3 100 ppm H_2O in nitrogen at 10 000 h^{-1} at 450 °C) over ion exchanged samples High Fe-ZSM-5, MiD Fe-ZSM-5, Low Fe-ZSM-5 and Fe-ZSM-5/500 vs the percentage Mössbauer sextet.

The comparable activities for N_2O conversion over High Fe-ZSM-5 and the Fe-ZSM-5/500 (Table 4.3 and Table 5.1) samples are surprising when the characteristics are compared (Figure 6.2 to Figure 6.7). On the other hand the remarkable similarity of the characteristics between the Low Fe-ZSM-5 and the Fe-ZSM-5/500 samples and the large difference in catalytic activity are surprising. The high peak counts from the (1 0 4) and (1 1 0) planes at 33.1° and 35.6° 2Θ on the powder XRD (Table 5.1and Figure 6.2), the high percentage of octahedral ferric species in small oligonuclear clusters characterized by strong absorptions between 300 and 400 nm (Table 5.4 and Figure 6.4), the low α-oxygen sites (Table 5.3 and Figure 6.8), the high percentage magnetic hyperfine field sextet on the Mössbauer spectrum (Table 5.5 and Figure 6.7) and the high activity for N_2O conversion (Table 4.3 and 5.1) over

Fe-ZSM-5/500 compared to the other Fe-ZSM-5 samples indicates that there are possibly different active sites and different mechanisms involved in the catalytic reaction.

Two generic iron forms, isolated iron ions and oligonuclear iron clusters, have been equivocally designated as the active sites in various reactions (Pérez-Ramírez, 2004). Battiston *et al.* (2003b) showed that the majority of iron appears to be present as Fe-binuclear complexes. The predominant active iron species in the Fe-ZSM-5/500 sample can probably be assigned to the oligonuclear iron clusters in the group $[(OH)FeOFe(OH)]^{2+}$ into isolated extra framework positions.

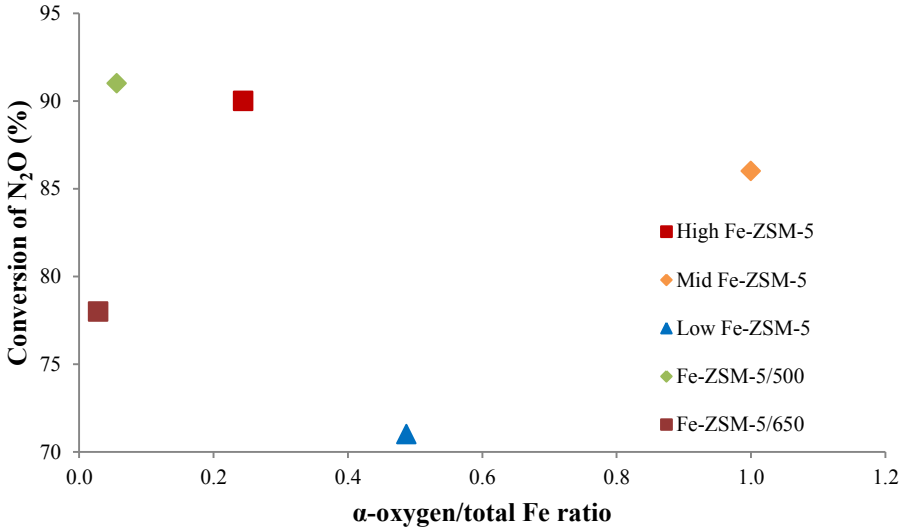

Figure 6.8 Conversion of N_2O (1 000 ppm N_2O, 100 ppm NO, 2.5 % O_2 and 3 100 ppm H_2O in nitrogen at 10 000 h^{-1} at 425 °C) over ion exchanged samples High Fe-ZSM-5, MiD Fe-ZSM-5, Low Fe-ZSM-5, Fe-ZSM-5/500 and Fe-ZSM-5/650 vs the α-oxygen/total Fe ratio.

From the large doublet area in the Mössbauer spectra (Figure 5.23 and Figure 6.6), the relatively high proportion of isolated Fe^{3+} species (the bands below 300 nm) in the UV/visible spectra (Table 5.4and Figure 5.22 and Figure 6.3) and the large α-oxygen/total Fe ratio (Table 5.3 and Figure 6.8), suggests that sample Mid Fe-ZSM-5 contains a high degree of isolated mononuclear iron species. On the other hand, sample High Fe-ZSM-5 displayed a similar doublet and sextet areas, 54 and 46 %, respectively on the Mössbauer spectra (Table 5.5 and Figure 6.6 and Figure 6.7) suggests that that it contains a lower amount of isolated

mononuclear and a higher amount binuclear oxygen bridged iron species compared to the other samples.

The large sextet area in the Mössbauer spectra (Figure 5.23 and Figure 6.7), the relatively low proportion of isolated Fe^{3+} species (the bands below 300 nm) in the UV/visible spectra (Table 5.4 and Figure 5.22 and Figure 6.3), the strong XRD reflections (Figure 5.6 and Figure 6.2) at 33.1° and 35.6° 2Θ (characteristic of α-Fe_2O_3) and the very low α-oxygen/total Fe ratio (Table 5.3 and Figure 6.8), suggests that Fe-ZSM-5/500 contains a very low proportion mononuclear iron species compared to the other samples. The high activity of this sample, and the fact that binuclear oxygen bridge iron species forms α-oxygen/total Fe ratio of 0.5 (Pirngruber and Roy, 2005), can probably be assigned to a low concentration very active catalytic sites as pointed out by Kubánek *et al.* (2002). On the other hand, the low activity of sample Low Fe-ZSM-5 which displays a large sextet area in the Mössbauer spectra (Figure 5.23 and Figure 6.7) and a relatively high proportion Fe_2O_3 clusters on the external surface (400 to 600 nm) in the UV/visible spectra (Table 5.4 and Figure 5.22 and Figure 6.5) with α-oxygen/total Fe ratio of 0.49 (Table 5.3 and Figure 6.8), can probably be ascribed to pore mouth blocking which reduces the diffusion rate in and out of the zeolite channel.

The Arrhenius plots for N_2O conversion of the different Fe-ZSM-5 range samples are considerably different for the High Fe-ZSM-5 and Mid Fe-ZSM-5 samples compared to the Low Fe-ZSM-5 and Fe-ZSM-5/500 samples (Figure 5.17). Figure 6.9 shows the shape and position of the High Fe-ZSM-5 and Mid Fe-ZSM-5 samples' Arrhenius plots compares reasonably well with the curves obtained from modelling over mononuclear iron sites as shown in Figure 2.10 by Hansen *et al.* (2007). While the shape and position of the Arrhenius plots for N_2O conversion over Low-Fe-ZSM-5 and the Fe-ZSM-5/500 samples, Figure 2.10, compare reasonable well with the result obtained from DFT modelling of the reactions over binuclear oxygen bridged iron sites with 65 % modelled as binuclear iron sites (Figure 2.11) and 35 % as Fe_2O_3 clusters on the external surface by Hansen *et al.* (2007).

Kinetic modelling of N_2O over mononuclear iron site by Heyden *et al.* (2005) (see section 2.5) indicates that the surface reactions of the surface oxygen (the α-oxygen) changes at different temperatures. At lower temperatures, the formation of the superoxide O^{2-} in the form of $Z^-[FeO_2]^+$ is preferred in a surface reaction of $Z^-[OFeO]^+$ to $Z^-[FeO_2]^+$ (reaction 11,

page 19) followed by adsorption of N_2O to form the transitional state $Z^-[OFeO_2]^+$ (reaction 14 and 15, page 19) whereas at higher temperature, the superoxide O^{2-} forms after the adsorption N_2O on $Z^-[OFeO]^+$ (reaction 12, page 19) forming the transitional state $Z^-[OFeO_2]^+$ (reaction 13, page 19). As the temperature increases the equilibrium shifts from the formation of $Z^-[FeO_2]^+$ superoxide in a surface reaction (reaction 11, page 19) to the adsorption of N_2O and the concomitant formation of the $Z^-[OFeO_2]^+$ superoxide (reaction 12 and 13, page 19). As stated in section 2.5, the gradual increase in the gradient of the Arrhenius plots is an indication that the decomposition over commercial samples High Fe-ZSM-5 and Mid Fe-ZSM-5 follows the mechanism proposed by Heyden *et al.* (2005) for mononuclear iron sites.

In Table 5.2 the micropore volume of Low Fe-ZSM-5 (0.121 cm^3/g) compared to Fe-ZSM-5/500 (0.100 cm^3/g) is considerable higher and slightly lower compared to the parent zeolite Z500 (0.133 cm^3/g) which is an indication that the ion exchange is considerably lower and that the sample contains a significant amount of Fe_2O_3 clusters on the external surface. The large difference in catalytic activity in the presence of H_2O and NO (see method in section 4.2.9) between Low Fe-ZSM-5 and Fe-ZSM-5/500 (71 and 91 % respectively), the relatively similar temperature programed N_2O conversion curve (see section 4.2.5) in Figure 5.16 and the slope of the Arrhenius plots in Figure 6.10 can be probably ascribed to pore blocking in the Low Fe-ZSM-5 sample.

Kinetic modelling of N_2O over binuclear oxygen bridged iron site by Hansen *et al.* (2007) (see section 2.5) indicates that the decomposition reactions changes at different temperatures. In Figure 6.10 the slope of the Arrhenius plots for Low Fe-ZSM-5 and Fe-ZSM-5/500 are consistent over the temperature range of 350 to 430 °C which indicates that a single reaction mechanism is present. The reaction can either be the formation of the $Z^-[OFeOFe]^+$ (reaction 17 and 18, page 21) or $Z^-[OFeOFeO]^+$ (reaction 19 or 20, page 21). The available data in this study is not sufficient to distinguish which reaction is the limiting reaction.

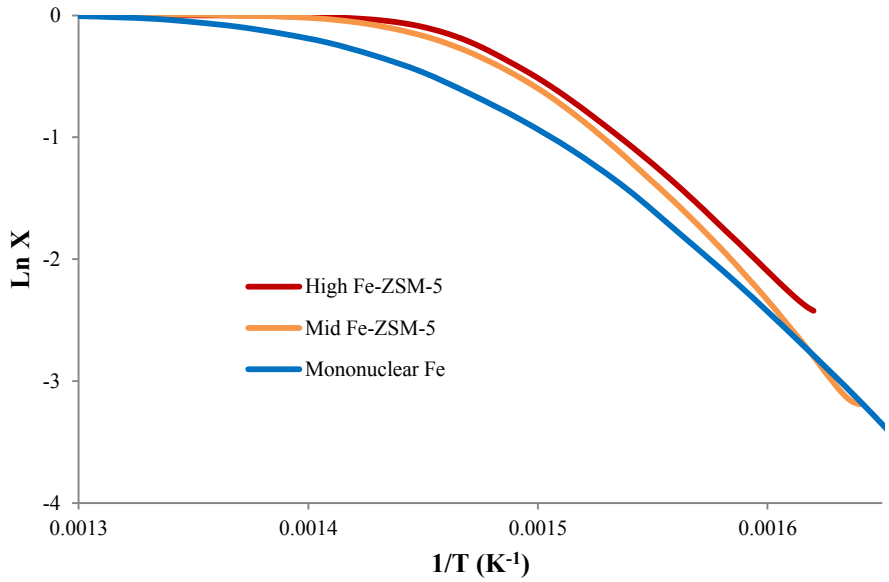

Figure 6.9 Arrhenius plots of N_2O conversion over High Fe-ZSM-5, Mid Fe-ZSM-5 (N_2O 4.8 vol % in helium, 10 ºC/min, 0.3 g sample) and Mononuclear Fe site determined with DFT (Hansen *et al.*, 2007)

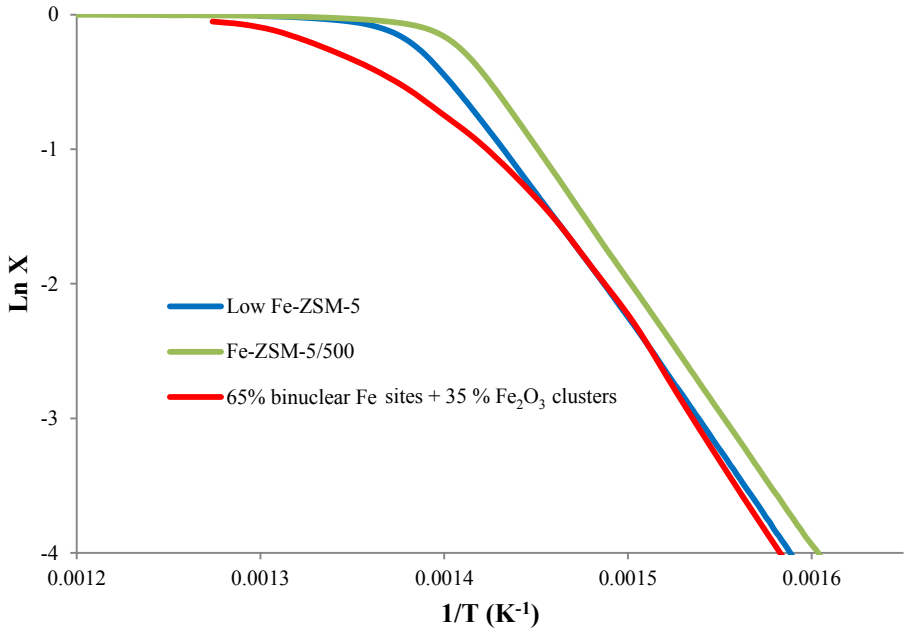

Figure 6.10 Arrhenius plots of N_2O conversion over Low Fe-ZSM-5, Fe-ZSM-5/500 (N_2O 4.8 vol % in helium, 10 ºC/min, 0.3 g sample) and 65 % binuclear Fe sites with 35 % Fe_2O_3 clusters as modelled with DFT (Hansen *et al.*, 2007)

Hence, it can be concluded from this study that samples High Fe-ZSM-5 and Mid Fe-ZSM-5 contains a large degree of active mononuclear iron sites which follows the reaction mechanism modelled by Heyden *et al.* (2005) and samples Low-Fe-ZSM-5 and the Fe-ZSM-5/500 contains a large degree of active binuclear oxygen bridged iron sites and is comparable with the reactions modelled over binuclear oxygen bridged iron sites with 65 % modelled as binuclear iron sites (Figure 2.11) and 35 % as Fe_2O_3 clusters on the external surface by Hansen *et al.* (2007).

6.3. The relationship between the α-oxygen content and the catalytic activity.

For the series of plant produced and laboratory calcined extrudate samples at different temperatures, samples Fe-ZSM-5/500 – Fe-ZSM-5/650, increasing calcination temperature results in a steady decrease in catalytic activity (Figure 5.24 and Table 5.1) and α-oxygen content (Figure 5.19 and 6.8 and Table 5.3). However, no correlation between α-oxygen content and catalytic activity is evident when considering the performance of all catalyst tested. This is best seen from the High-/Mid-/Low Fe-ZSM-5 series in Figure 6.8 where no monotonic relationship exist between α-oxygen content (Table 5.3) and N_2O conversion activity (Table 5.1), despite the High-/Mid-/Low Fe-ZSM-5 series showing a similar result to that of the Fe-ZSM-5/500 and Fe-ZSM-5/650 couple (Table 4.3 and Table 5.1). Moreover, whereas the performance of the Low-/Mid-/High Fe-ZSM-5 series (~ 70 - 90 % N_2O conversion, Table 4.3) is similar to that of the Fe-ZSM-5/500 and Fe-ZSM-5/650 couple (~ 78 – 91 % N_2O conversion, Table 5.1), the α-oxygen contents of the latter are more than an order of magnitude lower than those of the former. Similarly, given the very similar Fe contents of the catalysts tested (Table 5.3), there exist also no relationship between α-oxygen/Fe ratio and catalytic activity (Table 4.3, Table 5.1and Table 5.3).

In Figure 6.11 it is observed that the Mössbauer spectroscopy results of the doublet area and the α-oxygen content are not related, sample Mid Fe-ZSM-5 has an α-oxygen/Fe ratio of one and a doublet area of 82.9 %, on the other hand, sample Low Fe-ZSM-5 has an α-oxygen/Fe ratio of 0.49 and a doublet area of 14.8 %, while sample High Fe-ZSM-5 has an α-oxygen/Fe ration of 0.24 and a doublet area of 53.9 % (Figure 6.11 and Table 5.3 and Table 5.5).

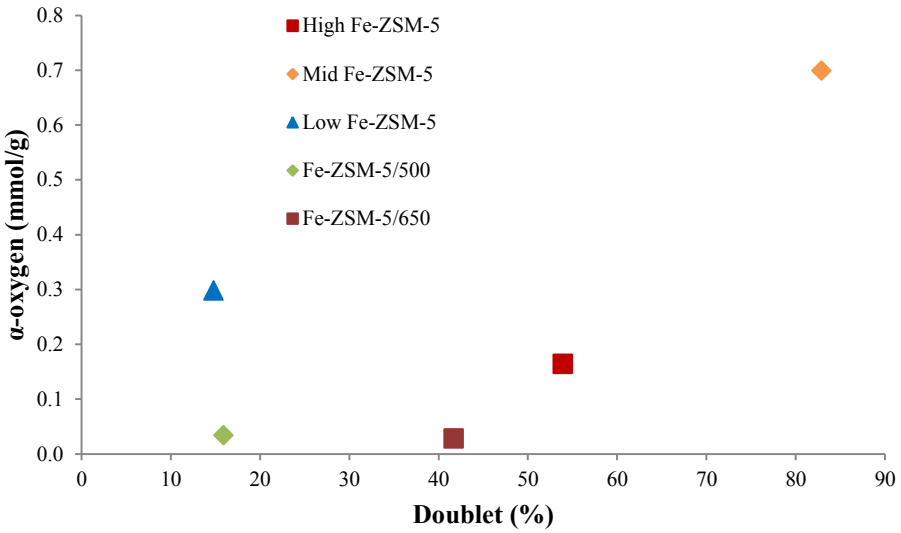

Figure 6.11 α-oxygen content for samples High Fe-ZSM-5, MiD Fe-ZSM-5 and Low Fe-ZSM-5 and Fe-ZSM-5/500 vs the α-oxygen/total Fe ratio.

Two distinctly different α-oxygen sites have been identified in the literature, mononuclear ($[FeO]^{3+}$) and binuclear oxygen bridged iron species ($[HO\text{-}Fe\text{-}O\text{-}Fe\text{-}OH]^{2+}$) (El-Malki *et al.*, 2000). For the mononuclear α-oxygen sites, Pirngruber and Roy (2005) proposed that the formation of α-oxygen is straight forward and that a 1:1 ratio of α-oxygen to iron exists and a ratio of 0.5 for the binuclear oxygen bridge iron species. From this study, a 1:1 ratio of α-oxygen to iron was obtained for the Mid Fe-ZSM-5 sample believed to contain a high degree of mononuclear iron sites and 0.5 ratio of α-oxygen to iron for the Low Fe-ZSM-5 sample believed to contain a high degree of binuclear oxygen bridged iron sites but for the High Fe-ZSM-5 sample a lower value (0.25) and hardly anything for samples Fe-ZSM-5/500 and Fe-ZSM-5/650 (0.056 and 0.028 respectively) were obtained (Table 5.3). Therefore it is concluded from this study that the α-oxygen content is not related to the N_2O conversion activity for Fe-ZSM-5 (Figure 6.8).

6.4. The effect of temperature during the final calcination of the extruded catalyst.

Contrary to the literature where it was found that the activity increases with increasing temperature (see section 2.4), an increase in calcination temperature of the plant produced and laboratory calcined extrudate samples results in a drop in catalytic activity for N_2O conversion (

Table 5.1 and Figure 5.24). This cannot be ascribed to either a change in the zeolite relative crystallinity which is unaffected (Figure 5.7), nor a change in the content of α-Fe_2O_3 which is also unaffected (Table 5.1 – the intensities of iron oxide reflections at 33.1° and 35.6° 2θ). Likewise, the UV/visible spectra for samples calcined at 500 and 650 °C are identical (Figure 5.21) such that it is evident that the iron species present are stable during calcination between 500 and 650 °C and that no migration of the iron from the different cation positions occurs forming additional iron oxide particles. Both these methods are insensitive to the oxidation state of iron. Consequently, the change in N_2O conversion activity cannot be ascribed to any change in the nature of the iron species.

The increase in reducing agent consumption below 500 °C during the ammonia TPR of sample Fe-ZSM-5/650 calcined at 650 °C compared to sample Fe-ZSM-5/500 calcined at 500 °C (Figure 5.20) is an indication that hydroxide groups in the $[(OH)FeOFe(OH)]^{2+}$ species have been dehydroxylated at the higher temperature to two $[OFe]^{+}$ or an [OFeOFeO] species (Battiston *et al*., 2003b). Support for this transition to have occurred is the reduction in acidity observed for the sample calcined at 650 °C compared to that calcined at 500 °C (Figure 5.14) as a result of the dehydroxylation of hydroxide groups in the $[(OH)FeOFe(OH)]^{2+}$ species. The increase in both micro and meso pore volumes during high temperature calcination (Figure 5.10 and Figure 5.11 and Table 5.2) is consistent with mass being transported out of the zeolite pore structure in this process in which the oxo-bridged binuclear $[HO\text{-}Fe\text{-}O\text{-}Fe\text{-}OH]^{2+}$ complexes undergo reversible reduction at 500 °C (Marturano *et al.*, 2000).

The dihydroxylation of the $[(OH)FeOFe(OH)]^{2+}$ species upon increase in calcination temperature from 500 to 650 °C (as for samples Fe-ZSM-5/500 and Fe-ZSM-5/650) also strong influences the electronic environment of the Fe ions as showing in the different Mössbauer spectra (Figure 5.23 and Table 5.5). The magnetic hyperfine field sextet of the 500 ºC sample is converted into two sextets after heating to 650 ºC, each with an approximately equal chemical shift off-set on either side and both sextets exhibit magnetic hyperfine field strength of 53.6 T. This is indicative of the partial dehydroxylation of the iron complex without change in oxidation state, resulting in a loss of hydroxyl groups and the formation of oxide species. The oxygen atom in these species has a stronger electron withdrawing effect than the hydroxyl group resulting in a second magnetic hyper field and

second sextet in the Mössbauer spectrum (Figure 5.23). Roy *et al.* (2007) also reported that dihydroxylation of the Fe species took place during high temperature treatment of the catalysts, which according to Roy *et al.* (2007), lead to the formation of oxygen vacancies (i.e. lattice defects). These lattice defects then lead to a change in the electronic properties of the iron sites, which are associated with electron withdrawing Al Lewis centres.

The drop in catalytic activity for N_2O conversion with the increase in calcination temperature is in line with the findings of Yakovlev *et al.* (2001) that the hydroxylated site ($[OH\text{-}Fe\text{-}O\text{-}Fe\text{-}OH]^{2+}$) is more favourable for N_2O conversion than the dehydroxylated site ($[Fe\text{-}O\text{-}Fe]^{2+}$).

7. Conclusion

The solid ion exchange process of NH_4-ZSM-5 with ferrous chloride was studied. The release of small amounts of ammonium chloride at low temperature (< 100 °C) may indicate to some contact induced ion exchange of ammonia for iron that may have occurred during grinding, but most of the ion exchange proceeds only at elevated temperature. Initially, the milled ferrous chloride tetrahydrate blocks the pore mouths of the zeolite. On heating, the ferrous chloride tetrahydrate dissolves in its crystal water and the residual moisture of the SM27 substrate and diffuses into the zeolite micropores. On further heating, ferrous chloride reacts with the NH_4-zeolite in a Lewis acid/base reaction and ammonium chloride is released indicating that the ion exchange reaction is taking place, concomitantly porosity is restored. At 400 °C the ion exchange is completed, given that no more ammonium chloride desorbs. The restoration of the porosity, desorption of water (which can be attributed to the dehydration of the hydrated ferrous chloride and the residual moisture of the SM27 substrate) are also completed at around 400 °C and the lack of $FeCl_2$ XRD reflections at 300 °C, supporting the above conclusion.

For the α-oxygen content and correspondingly the concentrations of the respective iron oxides and iron hydroxides in the Fe-ZSM-5 samples no correlation to N_2O conversion activity could be found. Apparently the different forms of active iron species present in the samples (isolated extra framework Fe oxo-ions and binuclear oxo-iron complexes) form different α-oxygen sites and react differently with the N_2O.

The similarities in characteristics of the Fe-ZSM-5/500 sample and the low performing Low Fe-ZSM-5 sample (UV/visible, Mössbauer and N_2O conversion kinetics) and the distinct difference in there characteristics compared to those of more active High and Mid Fe-ZSM-5 samples indicate that there are possibly different active sites present in the catalysts. As described in the literature review (section 2.3 – 2.5), the dominating active iron species in the Low Fe-ZSM-5 and Fe-ZSM-5/500 samples may be binuclear oxygen bridged iron ($Z^-[(OH)FeOFe(OH)]^{2+}$) and for the High Fe-ZSM-5 and Mid Fe-ZSM-5 samples may be mononuclear iron ($[Z^-[FeO]^+$) in extra framework positions. The Low Fe-ZSM-5 sample contains a significant amount of Fe_2O_3 clusters on the external surface which reduces the

catalytic activity due to a reduction in pore diffusion of the reaction gases to and from the active sites.

However, a constant decline catalytic activity was observed when the plant produced and laboratory calcined extrudate samples was calcined at increasing temperatures. Powder XRD and UV/visible spectrums indicate that the zeolite structure and the state of the iron do not change at higher temperatures, but the Mössbauer spectra show a second magnetic hyperfine field sextet developed at higher calcination temperatures. This can be related to the dehydration and dehydroxylation of the Fe-binuclear complex.

The outcome of this study indicates towards the temperature in the final calcination stage as being the crucial factor. Low calcination temperatures even below 500 °C applied in the current process appear to be advantageous.

.

References

Abu-Zied B.M., Schwieger W., Unger A. Nitrous oxide conversion over transition metal exchanged ZSM-5 zeolites prepared by the solid-state ion-exchange method. Applied Catalysis B: Environmental 84 (2008) 277–288.

BalÁž P. Extractive Metallurgy of Activated Minerals. Process Metallurgy. 10 (2000).

Battiston A.A., Bitter J.H., de Groot F.M.F., Overweg A.R., Stephan O., van Bokhoven J.A., Kooyman P.J., van der Spek C., Vankó G., Koningsberger D.C. Evolution of Fe species during the synthesis of over-exchanged Fe/ZSM-5 obtained by chemical vapor deposition of $FeCl_3$. Journal of Catalysis 213 (2003a) 251–271.

Battiston A.A., Bitter J.H., Koningsberger D.C. Reactivity of binuclear Fe complexes in over-exchanged Fe/ZSM-5, studied by in situ XAFS spectroscopy 2. Selective catalytic reduction of NO with isobutene. Journal of Catalysis 218 (2003b) 163–177.

Barrett E.P., Joyner L.G., Halenda P.P. The determination of pore volume and area distributions in porous substances. I. Computations from nitrogen isotherms. Journal of the American Chemical Society 73 (1951) 373–380.

Berry F.J. Characterisation of heterogeneous catalysts by Mössbauer spectroscopy. Studies in Surface Science and Catalysis, 57, (1990), 299–372.

Bitter J.H., Battiston A.A., van Donk S., de Jong K.P., Koningsberger D.C. Accessibility of the Fe-species in Fe/ZSM-5 prepared via $FeCl_3$ sublimation. Microporous and Mesoporous Materials 64 (2003) 175–184.

Boroń P., Chmielarza L., Gurgul J., Łątka K., Shishido T., Krafft J., Dzwigaj S. BEA zeolite modified with iron as effective catalyst for N_2O conversion and selective reduction of NO with ammonia. Applied Catalysis B: Environmental 138–139 (2013) 434–445.

Brandenberger S., Kröchera O., Casapua M., Tissler A., Althoff R. Hydrothermal deactivation of Fe-ZSM-5 catalysts for the selective catalytic reduction of NO with NH_3. Applied Catalysis B: Environmental 101 (2011) 649–659.

Brandenberger S., Kröcher O., Tissler A., Althoff R. The determination of the activities of different iron species in Fe-ZSM-5 for SCR of NO by NH_3. Applied Catalysis B: Environmental 95 (2010a) 348–357.

Brandenberger S., Kröcher O., Tissler A., Althoff R. Estimation of the fractions of different nuclear iron species in uniformly metal-exchanged Fe-ZSM-5 samples based on a Poisson distribution. Applied Catalysis A: General 373 (2010b) 168–175.

Brandenberger S., Kröcher O., Wokaun A., Tissler A., Althoff R. The role of Brønsted acidity in the selective catalytic reduction of NO with ammonia over Fe-ZSM-5. Journal of Catalysis 268 (2009) 297–306.

Brunauer S., Bodor E.E., Mikhail R.S. Investigations of a Complete Pore Structure Analysis. Journal of Colloid and Interface Science 26, (1968) 45–53.

Brunauer S., Deming L.S., Deming W.S. and Teller E. Journal of the American Chemical Society, 62 (1940) 1723.

Brunauer S., Emmett P.H. and Teller E.J. Adsorption of Gases in Multimolecular Layers. Journal of the American Chemical Society, 60 (1938) 309.

Ćapek L., Kreibich V., Dědeček J., Grygar T., Wichterlová B., Sobalík Z., Martens J.A., Brosius R., Tokarová V. Analysis of Fe species in zeolites by UV–VIS–NIR, IR spectra and voltammetry. Effect of preparation, Fe loading and zeolite type. Microporous and Mesoporous Materials 80 (2005) 279–289.

Chen B., Liu N., Liu X., Zhang R., Li Y., Li Y., Sun X. Study on the direct conversion of nitrous oxide over Fe-beta zeolites: From experiment to theory. Catalysis Today 175 (2011) 245– 255.

Chen H.Y., Sachtler W.M.H. Activity and durability of Fe/ZSM-5 catalysts for lean burn NOx reduction in the presence of water vapour. Catalysis Today 42 (1998) 73–83.

Chávez-Rivas F., Rodríguez-Fuentes G., Berlier G., Rodríguez-Iznaga I., Petranovskii V., Zamorano-Ulloa R., Coluccia S. Evidence for controlled insertion of Fe ions in the framework of clinoptilolite natural zeolites Microporous and Mesoporous Materials 167 (2013) 76–81.

Coats, A.W., Redfern, J.P. Thermogravimetric Analysis: A review. The Analyst 88 (1963) 906–924.

Condon, J.B. Surface Area and Porosity Determinations by Physisorption Measurements and Theory. Elsevier. 2006.

Dickson D.P.E., Berry F.J. Mössbauer Spectroscopy. Cambridge University Press. 2012.

Delahay G., Valade D., Guzmán-Vargas A., Coq B. Selective catalytic reduction of nitric oxide with ammonia on Fe-ZSM-5 catalysts prepared by different methods. Applied Catalysis B: Environmental 55 (2005) 149–155.

Dubinin M.M. On Physical Feasibility of Brunauer's Micropore Analysis Method. Journal of Colloid and Interface Science, 46 (1974) 351–356.

Dubkov K.A., Ovanesyan N.S., Shteinman A.A., Starokon E.V., and Panov G.I. Evolution of Iron States and Formation of α-Sites upon Activation of Fe-ZSM-5 Zeolites. Journal of Catalysis 207 (2002) 341–352.

El-Malki, E.M., van Santen, R.A., and Sachtler, W.M.H. Active Sites in Fe/MFI Catalysts for NOx Reduction and Oscillating N_2O Conversion. Journal of Catalysis, 196 (2000) 212–223.

Fadoni M., Lucarelli L. Temperature programmed desorption, reduction, oxidation and flow chemisorption for the characterisation of heterogeneous catalysts. Theoretical aspects, instrumentation and applications. Studies in Surface Science and Catalysis, 120 (1999) 177–225.

Fierro G., Moretti G, Ferraris G, Andreozzi G.B. A Mössbauer and structural investigation of Fe-ZSM-5 catalysts: Influence of Fe oxide nanoparticles size on the catalytic behaviour for the NO-SCR by C_3H_8. Applied Catalysis B: Environmental 102 (2011) 215–223.

Gasser, R.P.H. An introduction to chemisorption and catalysis by metals, Clarendon Press, Oxford. (1985).

Fu C.M., Korchak V.N., Halls W.K. Conversion of Nitrous Oxide on FeY Zeolite. Journal of Catalysis, 68 (1981) 166–171.

Garten R.L., Delgass W.N., Boudart M. A Mössbauer Spectroscopic Study of the Reversible Oxidation of Ferrous Ions in Y Zeolite. Journal of Catalysis, 18 (1970) 90–107.

Gregg S.J. and Sing K.S.W. Adsorption, Surface Area and Porosity, Academic Press, London, ISBN 0-12-300956-1, (1982).

Groves M., Maurer R., Schwefer M., Siefert R. Abatement of N_2O and NO_x emissions from Nitric Acid Plants with Uhde EnnviNOx® process. Nitrogen 2006 International Conference, Vienna, Austria, (2006).

Guesmi H., Berthomieu D., Kiwi-Minsker L. Reactivity of oxygen species formed upon N_2O dissociation over Fe–ZSM-5 zeolite: CO oxidation as a model. Catalysis Communications, 11 (2010) 1026–1031.

Hansen N., Heyden A., Bell A.T., Keil F.J. Microkinetic modeling of nitrous oxide conversion on binuclear oxygen bridged iron sites in Fe-ZSM-5. Journal of Catalysis, 248 (2007) 213–225.

Heyden A., Bell A.T., Keil F.J. Kinetic modeling of nitrous oxide conversion on Fe-ZSM-5 based on parameters obtained from first-principles calculations. Journal of Catalysis, 233 (2005) 26–35.

Heinrich F., Schmidt C., Löffler E., Menzel M., Grünert W. Fe–ZSM-5 Catalysts for the Selective Reduction of NO by Isobutane - The Problem of the Active Sites. Journal of Catalysis, 212 (2002) 157–172.

Hensen E.J.M., Zhu Q., Hendrix M.M.R.M., Overweg A.R., Kooyman P.J., Sychev M.V., Van Santen R.A. Effect of high-temperature treatment on Fe/ZSM-5 prepared by chemical vapor deposition of $FeCl_3$ I. Physicochemical characterization. Journal of Catalysis, 221 (2004) 560–574.

Hensen E.J.M., Zhu Q., Van Santen R.A. Extraframework Fe-Al-O species occluded in MFI zeolite as the active species in the oxidation of benzene to phenol with nitrous oxide. Journal of Catalysis, 220 (2003) 260–264.

Høj M., Beier M.J., Grunwaldt J., Dahl S. The role of monomeric iron during the selective catalytic reduction of NOx by NH_3 over Fe-BEA zeolite catalysts. Applied Catalysis B: Environmental 93 (2009) 166–176.

Ito S., Hukunaga K., Kaneko Y. Preparation of cobalt potassium phosphate pigment by mechanochemical solid phase reaction. Shikizai Kyokaishi. 52 (1970) 677–681.

Jia J., Sun Q., Wen B., Chen L.X., Sachtler W.M.H. Identification of highly active iron sites in N20-activated Fe/MFI. Catalysis Letters, 82 (2002) 7–11.

Karge H.G. Solid-state Reactions of Zeolites. Studies in Surface Science and Catalysis, 83 (1994) 135–146.

Kaucký D., Sobalík Z., Schwarze M., Vondrová A., Wichterlová B. Effect of FeH-zeolite structure and Al-Lewis sites on N_2O conversion and NO/NO_2-assisted reaction. Journal of Catalysis, 238 (2006) 293–300.

Kharitonov A.S., Fenelonov V.B., Voskresenskaya T.P., Rudina N.A., Molchanov V.V., Plyasova L.M., Panov G.I. Mechanism of Fe-ZSM-5 milling and its effect on the catalytic performance in benzene to phenol oxidation. Zeolites, 15 (1995) 253–258.

Kirk R.E., Othmer D.F. Encyclopedia of chemical technology, third edition. Wiley, (1984).

Kiwi-Minsker L., Bulushev D.A., Renken A. Active sites in HZSM-5 with low Fe content for the formation of surface oxygen by decomposing N_2O: is every deposited oxygen active? Journal of Catalysis 219 (2003) 273–285.

Kondratenko E.V., Pérez-Ramírez J. Micro-kinetic analysis of direct N_2O conversion over steam-activated Fe-silicalite from transient experiments in the TAP reactor. Catalysis Today 121 (2007) 197–203.

Kosanović C., Čižmek A., Subotić B., Šmit I., Stubićar M., Tonejc A. Mechanochemistry of zeolites: Part 3. Amorphization of zeolite ZSM-5 by ball milling. Zeolites, 15 (1995) 51–57.

Krishna K., Makkee M. Preparation of Fe-ZSM-5 with enhanced activity and stability for SCR of NOx. Catalysis Today, 114 (2006) 23–30.

Kubánek P., Wichterlová B., Sobalék Z. Nature of Active Sites in the Oxidation of Benzene to Phenol with N_2O over H–ZSM-5 with Low Fe Concentrations. Journal of Catalysis, 211 (2002) 109–118.

Kumar M.S., Schwidder M., Grünert W., Brückner A. On the nature of different iron sites and their catalytic role in Fe-ZSM-5 DeNOx catalysts: new insights by a combined EPR and UV/VIS spectroscopic approach. Journal of Catalysis 227 (2004) 384–397.

Kurian R. First principles theoretical modelling of the isomer shift of Mössbauer spectra. Rijksuniversiteit Groningen. (2011).

Lázár K., PáI-Borbély G., Beyer H.K., Karge H.G. Catalysts by solid-state ion exchange: Iron in zeolite. Preparation of catalysts VI. Scientific Bases for the Preparation of Heterogeneous Catalysts (1995) 551–559.

Lefelshtel N., Nadiv S., Lin I.J., Zimmels Y. Production of zinc ferrite in a mechanochemical reaction in a ball mill. Powder Technology 20 (1978) 211–217.

Li Y., Armor J.N. Ammoxidation of ethane V. Solid-state ion exchange to prepare cobalt zeolite catalysts. Applied Catalysis A: General 188 (1999) 211–217.

Li L., Shen Q., Li J., Hao Z., Xu Z.P., Maxlu G.Q. Iron-exchanged FAU zeolites: Preparation, characterization and catalytic properties for N_2O conversion. Applied Catalysis A: General 344 (2008) 131–141.

Li L.D., Shen Q., Yu J., Hao Z. , Xu Z., Maxlu G.Q. Fe-USY Zeolite Catalyst for Effective Conversion of Nitrous Oxide. Environmental Science & Technology Letters 41 (2007) 7901–7906.

Li G., Pidko E.A., van Santen R.A., Feng Z., Li C., Hensen E.J.M. Stability and reactivity of active sites for direct benzene oxidation to phenol in Fe/ZSM-5: A comprehensive periodic DFT study. Journal of Catalysis 284 (2011) 194–206.

Lodewyckx P., Verhoeven L. The applicability of the Dubinin-Radushkevich equation to the very low pressure region of isotherms of various microporous solids. Studies in Surface Science and Catalysis 144 (2002) 731–735.

Long J., Wang X., Ding Z., Zhang Z., Lin H., Dai W., Fu X. Binuclear μ-hydroxo-bridged iron clusters derived from surface organometallic chemistry of ferrocene in cavities of HY zeolite: Local structure, bound sites, and catalytic reactivity. Journal of Catalysis 264 (2009) 163–174.

Long R.Q., Yang R.T. Temperature-Programmed Desorption/Surface Reaction (TPD/TPSR) Study of Fe-Exchanged ZSM-5 for Selective Catalytic Reduction of Nitric Oxide by Ammonia. Journal of Catalysis 198 (2001) 20–28.

Malet P. Thermal desorption methods. Chapter 6. Studies in Surface Science and Catalysis 57 (1990) 333–382.

Marturano P., Drozdová L., Kogelbauer A., Prins R. Fe/ZSM-5 Prepared by Sublimation of $FeCl_3$: The Structure of the Fe Species as Determined by IR, ^{27}Al MAS NMR, and EXAFS Spectroscopy. Journal of Catalysis 192 (2000) 236–247.

Marturano P., Drozdová L , Pirngruber G.D., Kogelbauer A., Prins R. The mechanism of formation of the Fe species in Fe/ZSM-5 prepared by CVD. Physical Chemistry Chemical Physics 3 (2001) 5585–5595.

Marturano P., Kogelbauer A. and Prins R. Different methods for preparation of Fe-ZSM-5 as catalyst for the selective catalytic reduction of nitrogen oxides. Studies in Surface Science and Catalysis 125 (1999) 619–625.

Mohamed M.M., Ali I.O., Eissa N.A. Effect of thermal treatment on surface and bulk properties of Fe/ZSM-5 zeolites prepared by different methods. Microporous and Mesoporous Materials 87 (2005) 93–102.

Moulijn J.A., Van Leeuwen P.W.N.M., Van Santen R.A. Temperature programmed reduction and sulphiding. Studies in Surface Science and Catalysis (1993) 401–417.

Øygarden A.H., Pérez-Ramírez J. Activity of commercial zeolites with iron impurities in direct N_2O conversion. Applied Catalysis B: Environmental 65 (2006) 163–167.

Overweg A.R., Crajé M.W.J., Van der Kraan A.M., Arends I.W.C.E., Ribera A., Sheldon R.A. Remarkable N_2 affinity of a steam-activated Fe-ZSM-5 catalyst: a ^{57}Fe Mössbauer study. Journal of Catalysis 223 (2004) 262–270.

Panov G.I., Kharitonov A.S., Soholev V.I. Oxidative hydroxylation using dinitrogen monoxide: a possible route for organic synthesis over zeolites. Applied Catalysis A: General, 98 (1993) 1–20.

Panov G.I, Sobolev V. I., Dubkov K. A., Kharitonov A. S. Biomimetic oxidation on Fe complexes in zeolites. Studies in Surface Science and Catalysis, 101 (1996) 493–502.

Panov G.I., Starokon E.V., Pirutko L.V., Paukshtis E.A. and Parmon V.N. New reaction of anion radicals O^- with water on the surface of FeZSM-5, Journal of Catalysis 254 (2008) 110–120.

Park J, Choung J, Nam I, Ham S. N_2O conversion over wet- and solid-exchanged Fe-ZSM-5 catalysts Applied Catalysis B: Environmental 78 (2008) 342–354.

Patnaik P. Handbook of Inorganic Chemicals. McGraw-Hill, 2002.

Pérez-Ramírez J. Active iron sites associated with the reaction mechanism of N_2O conversions over steam-activated FeMFI zeolites. Journal of Catalysis 227 (2004) 512–522.

Pérez-Ramírez J., Kapteijn F., Groen J.C., Doménech A., Mul G., Moulijn J.A. Steam-activated FeMFI zeolites. Evolution of iron species and activity in direct N_2O conversion. Journal of Catalysis 214 (2003) 33–45.

Pérez-Ramírez J., Kapteijn F., Mul G., Moulijn J.A. NO-Assisted N_2O Conversion over Fe-Based Catalysts: Effects of Gas-Phase Composition and Catalyst Constitution. Journal of Catalysis 208 (2002a) 211–223.

Pérez-Ramírez J., Kumar M.S., Brückner A. Reduction of N_2O with CO over FeMFI zeolites: influence of the preparation method on the iron species and catalytic behaviour. Journal of Catalysis 223 (2004) 13–27.

Pérez-Ramírez, J., Mul G., Kapteijn F., Moulijn J.A., Overweg A.R., Doménech A., Ribera A., Arends I.W.C.E. Physicochemical Characterization of Isomorphously Substituted Fe-ZSM-5 during Activation. Journal of Catalysis 207 (2002) 113–126.

Pieterse J.A.Z., Pirngruber G.D., Van Bokhoven J.A. Booneveld S. Hydrothermal stability of Fe-ZSM-5 and Fe-BEA prepared by wet ion-exchange for N_2O conversion. From Zeolites to Porous MOF Materials – the 40th Anniversary of International Zeolite Conference. (2007).

Pirngruber G.D., Luechinger M., Roy P.K., Cecchetto A. Smirniotis P. N_2O conversion over iron-containing zeolites prepared by different methods: a comparison of the reaction mechanism. Journal of Catalysis 224 (2004) 429–440.

Pirngruber G.D. and Roy P.K. A look into the surface chemistry of N_2O conversion on iron zeolites by transient response experiments. Catalysis Today 110 (2005) 199–210.

Qi G., Gatt J.E., Yang R.T. Selective catalytic oxidation (SCO) of ammonia to nitrogen over Fe-exchanged zeolites prepared by sublimation of $FeCl_3$. Journal of Catalysis 226 (2004) 120–128.

Randall H., Doepper R., Renken A. Reduction of nitrogen oxides by carbon monoxide over an iron oxide catalyst under dynamic conditions. Applied Catalysis B: Environmental 17 (1998) 357–369.

Rauscher M., Kesore K., MoÈnnig R., Schwieger W., Tiβler A., Turek T. Preparation of a highly active Fe-ZSM-5 catalyst through solid-state ion exchange for the catalytic conversion of N_2O. Applied Catalysis A: General 184 (1999) 249–256.

Rettner, C.T, Auerbach, D.J. Chemical Dynamics at the Gas-Surface Interface. Journal of Physical Chemistry 100 (1996) 13021–13033.

Roy P.K., Prins R., Pirngruber G.D. The effect of pretreatment on the reactivity of Fe-ZSM-5 catalysts for N_2O conversion: Dehydroxylation vs. steaming. Applied Catalysis B: Environmental 80 (2008) 226–236.

Salvador F., Sánchez-Jiménez C., Sánchez-Montero M. J., Salvador A. A review of the application of the BET equation to experimental data: the C parameter. Studies in Surface Science and Catalysis 144 (2002) 379–386.

Schwidder M., Grünert W., Bentrup U., Brückner A. Selective reduction of NO with Fe-ZSM-5 catalysts of low Fe content: Part II. Assessing the function of different Fe sites by spectroscopic in situ studies. Journal of Catalysis 239 (2006) 173–186.

Schwidder M., Heinrich F., Kumar M.S., Brückner A., Grünert W. Fe-ZSM-5 catalysts for the selective reduction of no: influence of preparation route on structure and catalytic activity. Studies in Surface Science and Catalysis 154 (2004) 2484–2492.

Sherman D.M., Waite T.D. Electronic spectra of Fe^{3+} oxides and oxide hydroxides in the near IR to near UV. American Mineralogist 70 (1985) 1262–1269.

Sklenak S., Andrikopoulos P.C., Boekfa B., Jansang B., Nováková, J., Benco L., Bucko T., Hafner J., Dédeček J. , Sobalík Z. N_2O conversion over Fe-zeolites: Structure of the active sites and the origin of the distinct reactivity of Fe-ferrierite, Fe-ZSM-5, and Fe-beta. A combined periodic DFT and multispectral study. Journal of Catalysis 272 (2010) 262–274.

Smoláková L., Tomáš Gryga T., Čapek L., Schneeweiss O., Zbořil R. Speciation of Fe in Fe-modified zeolite catalysts. Journal of Electroanalytical Chemistry 647 (2010) 8–19.

Sobolev V.I., Kharitonov A.S., Paukshtis Y.A., Panov G.I. Stoichiometric reaction of benzene with a-form of oxygen on Fe-ZSM-5 zeolites. Mechanism of aromatics hydroxylation by N_2O. Journal of Molecular Catalysis 84 (1993) 117–124.

Sobolik J.L., Ludlow D.K., Hessevick W.L. Parametric sensitivity comparison of the BET and Dubinin- models for determining char surface area by CO_2 adsorption. FUEL 71 (1992) 1195–1202.

Sun K., Xia H., Hensen E, Van Santen R., Li C. Chemistry of N_2O conversion on active sites with different nature: Effect of high-temperature treatment of Fe/ZSM-5. Journal of Catalysis 238 (2006) 186–195.

Sun Q., Gao Z.X., Chen H.Y., Sachtler W.M.H. Reduction of NOx with Ammonia over Fe/MFI: Reaction Mechanism Based on Isotopic Labeling. Journal of Catalysis 201 (2001) 89–99.

Taboada J.B., Hensen E.J.M., Arends I.W.C.E., Mul G., Overweg A.R. Reactivity of generated oxygen species from nitrous oxide over [Fe,Al]MFI catalysts for the direct oxidation of benzene to phenol. Catalysis Today 110 (2005) 221–227.

Tabor E., Závêta K., Sathua N.K., Tvarůžková Z., Sobalík Z. Characterization of iron cationic sites in ferrierite using Mössbauer spectroscopy. Catalysis Today 169 (2011) 16–23.

Thiessen P.A., Meyer K., Heinicke G. Grundlagen der Tribochemie, Akademie Verlag, Berlin, (1967).

Townsend R.P., Coker E.N. Ion exchange in zeolites. Chapter 11. Studies in Surface Science and Catalysis 137 (2001).

Varga J., Fudala Á., Halász J., Schõbel G., Kiricsi I. ZSM-5 zeolites modified by solid-state ion-exchange for NO conversion. Catalysis by Microporous Materials. Studies in Surface Science and Catalysis 94 (1995) 665–672.

Venkataraman K.S., Narayanan K.S. Energetics of collision between grinding media in ball mills and mechanochemical effects. Powder Technology 96 (199) 190–201.

Voskresenskii P.I. Solid-state reactions in analytical chemistry. Talanta. Pergamon Press Ltd 12 (1965) 11–16.

Webb P.A., Orr C. Analytical methods in fine particle technology. Micromeritics Instrument Corporation. 1997.

Wichterlova B., Sobalik Z., Dědeček J. Redox catalysis over metallo-zeolites: Contribution to environmental catalysis. Applied Catalysis B: Environmental 41 (2003) 97–114.

Xia H., Sun K., Liu Z., Feng Z., Ying P., Li C. The promotional effect of NO on N2O conversion over the bi-nuclear Fe sites in Fe/ZSM-5. Journal of Catalysis 270 (2010) 103–109.

Yakovlev A.L., Zhidomirov G.M., Van Santen R.A. DFT Calculations on N_2O Conversion by Binuclear Fe Complexes in Fe/ZSM-5. The Journal of Physical Chemistry B 105 (2001) 12297–12302.

Yoshizawa K., Shiota Y., Kamachi T. Mechanistic Proposals for Direct Benzene Hydroxylation over Fe-ZSM-5 Zeolite. The Journal of Physical Chemistry B 107 (2003) 11404–11410.

Yuranov I., Bulushev D.A., Renken A., Kiwi-Minsker L. Benzene hydroxylation over Fe-ZSM-5 catalysts: which Fe sites are active? Journal of Catalysis 227 (2004) 138–147.

Zecchina A., Rivallan M., Berlier G., Lambertia C. and Ricchiardia G. Structure and nuclearity of active sites in Fe-zeolites: comparison with iron sites in enzymes and homogeneous catalysts. Physical Chemistry Chemical Physics 9 (2007) 3483–3499.

Zhang B., Liu F., He H, Xue L. Role of aggregated Fe oxo species in N_2O conversion over Fe/ZSM-5. Chinese Journal of Catalysis 35 (2014) 1972–1981.

Appendix A: Analytical Methods – Extended Description

A-1. Physical adsorption

The term "physical adsorption" or "physisorption" refers to the phenomenon whereby gas molecules stick to a surface at a pressure less than the vapour pressure. The forces of attraction between the molecules being adsorbed and the surface are relatively weak van der Waals forces (Condon, 2006).

Surface analysis is performed on solid materials at temperatures where the adsorbing gas is below its triple point and above its freezing point (Condon, 2006). Nitrogen is frequently used under isothermal cryogenic conditions, usually at 77K, and the adsorption isotherm is the measurement of amount the adsorbed versus the adsorption pressure at constant temperature. Six isotherm types have been observed, labelled I through VI according to the classification developed by de Boer, codified by Brunauer *et al*., (1940) and supplemented by Gregg and Sing (1982).

There are several isotherm interpretations available. The most widely used is that of Brunauer, Emmett and Teller (BET) and its various modifications including the Brunauer, Deming, Deming and Teller (BDDT). Also widely used, especially for porous materials, are the Dubinin–Radushkevich (DR) and the Dubinin–Atackhov (DA) methods (Condon, 2006).

A-1.1 BET

The BET method is essentially an extension of the Langmuir theory for monolayer molecular adsorption to multilayer adsorption with the following hypotheses: (a) gas molecules physically adsorb on a solid in layers infinitely; (b) there is no interaction between each adsorption layer; and (c) the Langmuir theory can be applied to each layer (Brunauer et. al, 1938).

The model has persisted and the BET equation continues to be one of those most frequently used. Moreover, the BET method for determining the surface area of solids is internationally accepted and is routinely used in the determination of this parameter. In practice, the authors

of the model observed that the linearity of the BET representation was reduced to a small range (p/p_0= 0,05 - 0,3). Later studies have shown that for many systems that range is much more reduced, although there is still no criterion to select the range. Moreover, for Type III and V isotherms, the BET plot is never linear (Salvador et. al, 2002).

A-1.2 Micro porosity analysis

Micro porosity is defined as that pertaining to pore widths smaller than 2 nm with a further sub classification of supermicropores for pore sizes between 8 and 20 Å and ultramicropores for pore sizes below 8 Å (Dubinin, 1974).

Micro porosity may be measured via various methods which include the BET method, the de Boer t-plots, the MP method and the Dubinin–Radushkevich method for ultramicropores.

A-1.3 t-plot method

The micro porosity is determined with t-plot method by extrapolating the linear portion to the adsorption curve at low relative pressure by obtaining the intercept on the quantity of gas absorbed axis which is equivalent to the micro pore volume.

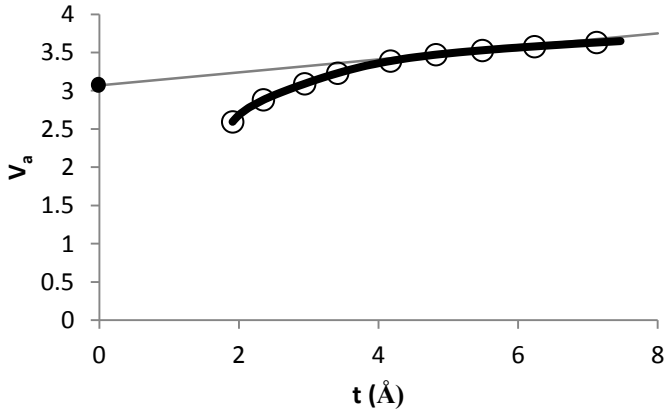

Figure I.1 Illustration of t-plot method for the determination of pore volume (Webb and Orr, 1997)

A-1.4 MP method

The MP method is applied for the determination of pore volume and surface area distributions of micropores, i.e., pores having widths of the order of 16 Å or less. The method is an extension of the "t-method" of de Boer. The MP-method of analysis uses a modeless characteristic of pore sizes, namely the hydraulic radius, r_h, which is equal to the ratio of the surface area of the normal cross section of the pore to its perimeter. The equivalent radius for the cylindrical model corresponds to the doubled hydraulic radius (Dubinin, 1974). The MP-method is based on the t-curve, which is a plot of the statistical thickness of the adsorbed film against p/p_0 for nonporous adsorbents. For porous solids, a straight line is usually obtained at least in the low pressure region, the slope of which the v_l - t plot gives the surface area of the adsorbent. Tangents drawn to the isotherm (Figure I.1) at different relative pressures determine surface area as a function of the hydraulic radius.

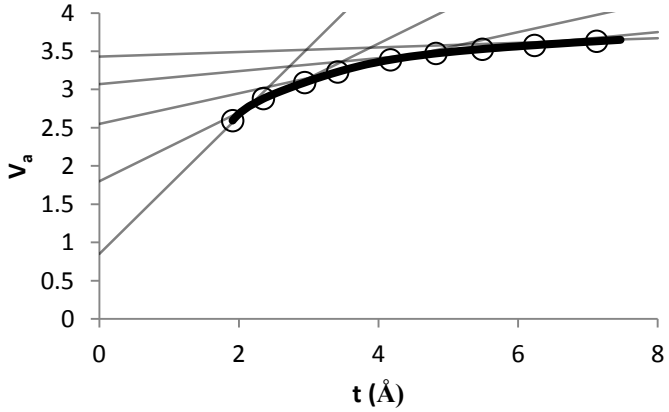

Figure I.2 Illustration of MP method for the determination of pore volume at different points along the nonlinear t-curve (Webb and Orr, 1997)

Dubinin (1974) pointed out that neither the MP- nor the BET-method is applicable to adsorbents which contain a significant fraction of ultra-micropores. The BET model uses a layer by layer structure of adsorption on the surface. It assumes that all sites on the surface are energetically homogeneous and that the heats of adsorption for all layers, except the first, are the same. Layer by layer adsorption is limited by the requirement that the monolayer must be filled before the outer layers can form. The validity of the assumption regarding the

equality of the heats of adsorption for the 'outer' layers has been questioned. Most surfaces are energetically heterogeneous which contradicts the BET model assumptions and this is the reason the model fails in the lower pressure region. Similarly, at higher relative pressures, the failure of the model is suspected to be due to the decrease in adsorption heat as the amount adsorbed increases (Sobolik *et al*, 1992).

A-1.5 Dubinin-Radushkevich models

The DR model has been developed for microporous surfaces, where the heat of adsorption is typically higher than for non-porous substances. Dubinin showed that heats of adsorption are typically greater for adsorption on energetically heterogeneous microporous surfaces than for adsorption on non-porous surfaces. This results in an increase in adsorption energy within the micropores, which Dubinin termed the adsorption-force field. The adsorption-force field enhances adsorption energy because the force fields in neighbouring pore walls are superimposed. The possibility of overlapping adsorption-force fields in the micropores leads to Dubinin's concept that the micropore volume is filled, in which case the physical model of layer by layer adsorption loses its significance. Dubinin's model also allows for micropore filling prior to monolayer formation and the adsorbate molecules may be shared by several surfaces (Sobolik *et al*., 1992).

The Dubinin-Radushkevich equation has the following form:

$$W = W_0 e^{\left(-\left(\frac{A}{\beta E_0}\right)^2\right)}$$

where W is the quantity adsorbed at relative pressure P/P_0 and temperature T, W_0 the limiting micropore volume, E_0 the characteristic energy of adsorption for the reference vapour and β the affinity coefficient. The characteristic curve is presented in Figure I.2. At higher log (P_0/P) a steep slope is observed which is due to micropore adsorption. Once the microporous area is completely covered, micropore filling as evident by the negative slope in Figure I.2. The intercept with the y-axis is the limiting micropore volume. When micropore filling is completed, monolayer adsorption occurs on the non-porous surfaces (Lodewyckx and Verhoeven, 2002).

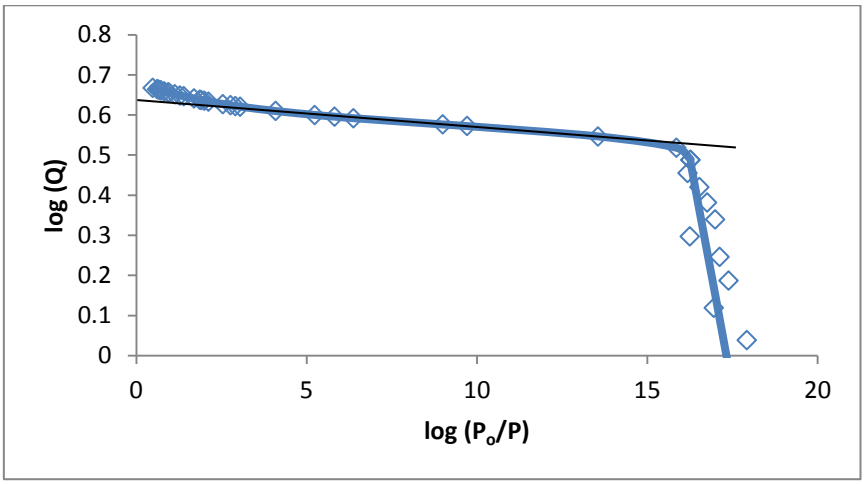

Figure I.3 Example of a typical N_2-isotherm with corresponding Dubinin-Radushkevich plot. (Lodewyckx and Verhoeven, 2002)

The Dubinin-Atackhov method is an extension of the Dubinin-Radushkevich method where the exponent n is optimised to give the best linear regression fit (Lodewyckx and Verhoeven, 2002). The Dubinin-Atackhov equation has the following form:

$$W = W_0 e^{\left(-\left(\frac{A}{\beta E_0}\right)^n\right)}$$

A-1.6 Mesoporosity

Mesoporosity is classified as porosity between 2 and 50 nm. Isotherms of mesoporous materials have a characteristic hysteresis between the adsorption and desorption branches. The extent of the hysteresis increases with the increase of mesoporocity and is determined via the BJH method.

The Barrett-Joyner-Halenda (BJH) method for calculating pore size distributions is based on a model of the adsorbent as a collection of cylindrical pores. The theory accounts for capillary condensation in the pores using the classical Kelvin equation, which in turn assumes a hemispherical liquid-vapor meniscus and a well-defined surface tension. The BJH theory also incorporates thinning of the adsorbed layer through the use of a reference isotherm; the Kelvin equation is only applied to the "core" fluid (Barrett *et al*., 1951).

A-2. Temperature programmed methods

A-2.1 Temperature programmed desorption (TPD)

There are different methods to perform the TPD, via static volumetric, static gravimetric and flow methods. In the volumetric method, the sample is kept under high vacuum before the analysis. The analytical instrument then introduces known doses of reactive gas into the sample holder, measuring afterwards the equilibrium pressure that will be established between the sample and the gaseous phase. The gravimetric technique is in principle the same as the volumetric one, the difference is that the amount of gas adsorbed is measured by the weight change of the sample during the adsorption process. Flow methods are carried out at atmospheric pressure by passing an inert carrier gas through the sample in a suitable sample cell and then over a detector to determine the change in gas composition (Fadoni and Lucarelli, 1999).

Thermal desorption experiments can be described in the following way. A probe gas is absorbed on a surface at a given temperature. During the adsorption, gas molecules chemically adsorb at the active sites forming chemical bonds. After adsorption, the sample is purged at the same temperature for a period of time with an inert carrier gas to remove any reversible physically adsorbed gas species. The sample is then heated at a constant rate usually following a linear programme, hence the technique is referred to as Temperature Programmed Desorption (TPD). During heating, the temperature and evolution of adsorbed species to the gas phase are continuously monitored. The TPD spectrum is a plot of the concentration of the desorbed gas vs. temperature, and is determined by the changes in the desorption rate with the temperature (Malet, 1990).

A-2.2 Temperature programmed reduction (TPR) and temperature programmed oxidation (TPO)

In the TPR technique an oxidised catalyst precursor is subjected to a programmed temperature rise, while a reducing gas mixture is passed over it (usually, hydrogen diluted in some inert gas such as nitrogen or argon). In the TPO technique, the sample is in the reduced form and is submitted to a programmed temperature excursion but, in this case, an oxidising

gas mixture (oxygen in helium) is passed over the sample. The reduction or oxidation rates are continuously measured by monitoring the change in composition of the effluent of after the reactor. The decrease in H_2 or O_2 concentration in the effluent gas with respect to the initial composition allows for quantification of transformations observed (Fadoni and Lucarelli, 1999).

A-2.3 Thermogravimetric analysis (TGA)

Thermogravimetric analysis (TGA) is a method of thermal analysis in which changes in physical and chemical properties of materials are measured as a function of increasing temperature (with constant heating rate), or as a function of time (with constant temperature and/or constant mass loss). TGA can provide information about physical phenomena, such as second-order phase transitions, including vaporization, sublimation, absorption, adsorption, and desorption. Likewise, TGA can provide information about chemical phenomena including chemisorption, desolvation (especially dehydration), conversion, and solid-gas reactions (e.g., oxidation or reduction) (Coats, 1963).

TGA is commonly used to determine selected characteristics of materials that exhibit either mass loss or gain due to conversion, oxidation, or loss of volatiles (such as moisture). Common applications of TGA are (1) materials characterization through analysis of characteristic conversion patterns, (2) studies of degradation mechanisms and reaction kinetics, (3) determination of organic content in a sample, and (4) determination of inorganic (e.g. ash) content in a sample, which may be useful for corroborating predicted material structures or simply used as a chemical analysis (Coats, 1963).

A-3. Mössbauer spectroscopy

Mössbauer spectroscopy has found widespread application in catalysts containing Mössbauer active elements like ^{57}Fe (Overweg *et al.*, 2004). Typically, three types of nuclear interactions may be observed: an isomeric shift, also known as a chemical shift; quadrupole splitting; and magnetic hyperfine splitting.

A-3.1 Isomer Shift (IS)

The isomer shift observed during Mössbauer spectroscopy is a result of the electron density of the Mössbauer atom where the isomer shift peaks vary in different materials due to the hyperfine interaction between the nucleus and the inner electrons (Futz, 2011). For the ^{57}Fe atom the effective radius of the exited state is smaller than the ground state. The 3d electrons partly screen the 4s electrons resulting in a more positive isomer shift as the number of 3d electrons increases. The isomer shift gives a good indication of the valance state of the Mössbauer atom (Futz, 2011). When hyperfine interactions are present the isomer shift sets the centre of gravity of the Mössbauer spectrum (Berry, 1990).

Table I.1 Isomer shift ranges (in mm/s) in iron compounds (Dickson and Berry, 2012).

	High Spin			Low Spin		
			-			
Fe(VI)	-0.8	to	0.9			
Fe(IV)	-0.2	to	0.2	0.1	to	0.2
Fe(III)	0.1	to	0.5	-0.1	to	0.5
Fe(II)	0.6	to	1.7	-0.2	to	0.5
Fe(0)				-0.2	to	-0.1

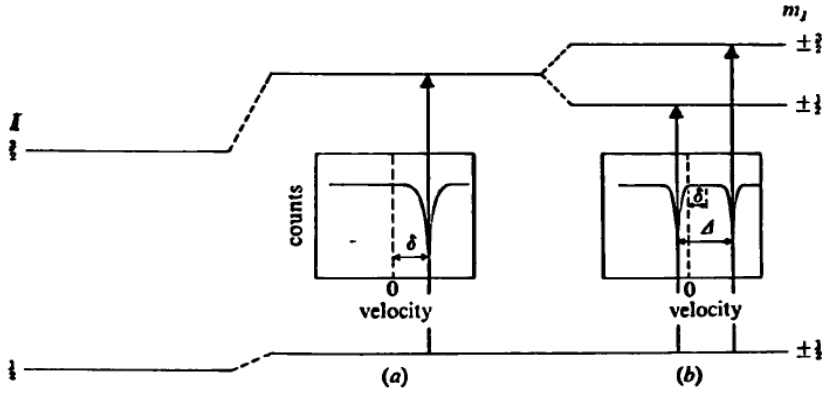

Figure I.4 The effects on the nuclear energy levels of ^{57}Fe of (a) the chemical isomer shift and (b) the quadrupole splitting (Berry, 1990)

A-3.2 Quadrupole Splitting (QS_{Doub})

The electric quadrupole splitting is an indication of the symmetry of the Mössbauer atom. Atoms with a nuclear angular quantum number I > ½ have asymmetrical charge densities which are characterised by electric quadrupole splitting during Mössbauer spectroscopy (Futz, 2011). The transitional metal elements have d-electrons with a number of different energy levels which affects the symmetry of the atom with an electric field gradient. On radiation during Mössbauer spectroscopy the quadrupole splitting gives information regarding the high and low spin Fe complexes, the ligand charge, ligand effect and the coordination (Futz, 2011). In crystalline solids, the position and the environment in the crystalline matrix distorts the electronic structure of the Mössbauer atom which is visible in the quadrupole splitting (Berry, 1990).

A-3.3 Magnetic hyperfine splitting (H)

When a Mössbauer active atom is placed in a magnetic field the interaction completely raises the degeneracy of a nuclear state and splits it into 2I +1 substates (Berry, 1990). In the case of ^{57}Fe the ground state with I = ½ splits into two substates, {−½, +½} and the excited state with I = 3/2 splits into four substates, {−3/2, −½, +½, +3/2} (Futz, 2011). The hyperfine magnetic field at the nucleus arises from any unpaired spin of the atoms' own electrons and therefore depends on the oxidation and spin state of the atom and are confined to ferro-, ferri-, or antiferromagnetic materials (Futz, 2011).

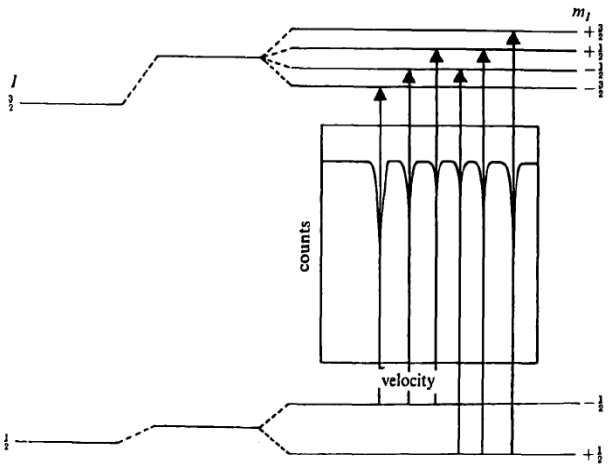

Figure I.5 The effect of magnetic splitting on the nuclear energy levels of ^{57}Fe (Berry, 1990).C